國立臺灣大學理學院物理學研究所

碩士論文

Department of Physics

College of Science

National Taiwan University

Master Thesis

# 在 Belle 實驗中尋找 $B^0 \to p\bar{\Sigma}^0\pi^-$ 衰變與測量 $B^0 \to p\bar{\Lambda}\pi^-$ 之衰變率

# Searching for $B^0 \to p\bar{\Sigma}^0\pi^-$ and Measurement of $B^0 \to p\bar{\Lambda}\pi^-$ at Belle Experiment

張傳彧

Chuan-Yu Chang

指導教授: 王名儒 教授

Advisor: Min-Zu Wang, Ph.D.

中華民國 111 年 8 月

August, 2022

doi:doi:10.6342/NTU202203205

doi:doi:10.6342/NTU202203205

# 國立臺灣大學碩士學位論文
# 口試委員會審定書

## 在Belle實驗中尋找$B^0 \to p\bar{\Sigma}\pi^-$之衰變與
## 測量$B^0 \to p\bar{\Lambda}\pi^-$之衰變率
## Searching for $B^0 \to p\bar{\Sigma}\pi^-$ and Measurement of $B^0 \to p\bar{\Lambda}\pi^-$ at Belle Experiment

本論文係張傳彧君（R08222067）在國立臺灣大學物理學所完成之碩士學位論文，於民國111年8月24日承下列考試委員審查通過及口試及格，特此證明

口試委員：王名儒（簽名）

（指導教授）

張寶棣　張敏娟

徐靜戈

doi:doi:10.6342/NTU202203205

# Acknowledgements

The following contents show my deepest gratitude for the each people who helped me in my master career.

I would like to thank my master thesis committee members Prof. Min-Zu Wang(王名儒), Prof. Min-Chuan Chang(張敏娟), Prof. Pao-Ti Chang(張寶棣) and Dr. Jing-Ge, Hsu(徐靜戈) first. Thank them for their very useful comments for my oral defense and master thesis .

I would also like to give my sincere gratitude to my advisor Prof. Min-Zu Wang. As a newbie of experimental particle physics, his suggestions always inspire me and make me more understand how to work at experimental particle physics field at all points.

Next I would like to express my appreciation to Prof. Pao-Ti Chang for letting me join the Belle analysis meeting, and sharing a lot of useful comments whether in the meeting or the personal discussion.

Then I am going to thank my colleagues in NTU HEP group. Pin-Chun, Chou (周品君) who taught me how to do Belle analysis when I was a freshman. Yu-Tan Chen (陳昱潭) who taught me some computer knowledge at the beginning, shared a lot of opinions whether in research or not, and sometimes held interesting activities. Kun-Xian, Huang (黃坤賢) and Ching-Hua, Li (李清化) who gave me many insightful advice to my project. Yuan-Ru, Lin (林沅儒) who always shared interested tools and opinions to me. Also Yen-Ting, Chin (金彥廷), Cheng-Wei, Lin (林承威), Yu-Chen, Chen (陳昱蓁), Wing Chen (陳文翊), You-Shuan, Liang (梁佑瑄), Shu-Pin, Lin (林紓平), Ching-Hao, Chen (陳勁豪), Chou-Han, Hsu (徐舟晗), Bo-Wei, Huang (黃柏瑋), Kai-Ning, Chu (朱凱寧), Yu-Chieh, Ku (辜禹傑), Tao-Chen, Yu (陶鎮宇), Jeng-Hao, Su (蘇鉦皓), Wei-Che, Lin (林偉哲) and those not mentioned above. Without you all, I wouldn't have such colorful graduate student life.

I also want to thank my college classmates. Ching-Hsuan, Chen (陳敬軒), Chun-Wen, Yang (楊淳文), Kai-Chun, Chen (陳愷駿), Po-Yuan, Wang (汪伯元), Hung-Lin, Lin (林宏霖), Ching-Hsien, Chen (陳景威), Po-Wei, Lai (賴柏瑋), Ming-Sen, Guo (郭明森), Yueh-Heng, Lu(呂岳衡), Chui-Cheng, Sun(孫垂正), Chia-Ching, Hsiao (蕭嘉慶),



doi:doi:10.6342/NTU202203205

Min-Yen, Tsai (蔡旻諺), Kun-Rong, Lin (林坤融), Yu-Ru, Li (李宥儒), Da-You, Yang (楊大友), Yu-Ren, Chen (陳郁仁), Chun-Ren, Deng (鄧淳仁), Yu-Rong, Huang (黃俞容), Ya-Tun, Hsu (許雅惇). Thank you all for remembering me and being willing to invite me to join your gathering.

Because of the previous accident I suffered, I would like to thank police Hong-Yi, Lin (林弘翊) for dealing with my case and talking with me make me feel comfortable. My the other gratitude will be given to teacher Wei-Yu, Chen (陳威宇) who chatted with me every week let me can express my trouble.

For the previous student career, I would like to thank my senior high school teacher Hung-Hsuan, Wang (王宏軒) for inspiring me to be interested in physics, and also thank my college teacher Prof. Rong-Sheng, Guo (郭榮升) for making me meet with experimental particle physics.

Finally, I want to show my deepest gratitude to my family. You all give me the strongest support to make me pursue my dream with all my heart. Also, I am going to thank my life partner Yi-Ching, Chen for her undying accompany during my graduate student career.



doi:doi:10.6342/NTU202203205

# Abstract

We use the data sample corresponding to an integrated luminosity of 711 $fb^{-1}$ and contain $772 \times 10^6$ $B\bar{B}$ pairs collected around $\Upsilon(4S)$ with Belle detector at the super KEKB asymmetric-energy $e^+$ $e^-$ collider to search for $B^0 \to p\bar{\Sigma}^0 \pi^-$ and measure $B^0 \to p\bar{\Lambda}\,\pi^-$ for the confirming of theoretic prediction of branching fraction and study of the threshold enhancement, polarized angle distribution. We measured the signal branching fraction $0.86^{+0.28}_{-0.26} \pm 0.07 \times 10^{-6}$ with 3.5 $\sigma$ in threshold enhancement region ($M_{p\bar{\Lambda}} < 2.8$ GeV/c$^2$) which indicates the hint of threshold enhancement, and set upper limit $1.2 \times 10^{-6}$ with 90 C-L. Also, we update the branching fraction $3.15^{+0.25}_{-0.24} \pm 0.16 \times 10^{-6}$, and the differential branching fraction of $M_{p\bar{\Lambda}}$ and $cos\theta_p$ dimensions respectively in $B^0 \to p\bar{\Lambda}\pi^-$ channel.

**Keywords:** Belle, $B$ meson, Baryonic decay



doi:doi:10.6342/NTU202203205

doi:doi:10.6342/NTU202203205

# 摘要

本次研究我們使用了日本 B 介子工廠的 7.72 億對 B 介子對來尋找及量測中性 $B^0$ 介子衰變至 $p\bar{\Sigma}^0\pi^-$ 與 $p\bar{\Lambda}\pi^-$ 之衰變分支比用以確認其衰變分支比的理論預測及 $p\bar{\Lambda}$ 不變質量與重子對靜止座標系中質子與強子的角度分佈。在本次分析研究中, 我們在特定 $p\bar{\Lambda}$ 不變質量的區間中量測到 $3.5\sigma$ 的中性 $B^0$ 介子衰變至 $p\bar{\Sigma}^0\pi^-$ 的衰變分支比 $0.86^{+0.28}_{-0.26}\pm0.07\times10^{-6}$ 及在 90% 的信心水準下衰變分支比上限 $1.2\times10^{-6}$, 並且更新了中性 $B^0$ 介子至 $p\bar{\Lambda}\pi^-$ 衰變頻道的衰變分支比及在 $p\bar{\Lambda}$ 不變質量與重子對靜止座標系中質子與強子的角度兩個維度的微分分支比。

關鍵字： Belle 實驗、$B$ 介子、含重子衰變



doi:doi:10.6342/NTU202203205

doi:doi:10.6342/NTU202203205

# Contents

Page





doi:doi:10.6342/NTU202203205

doi:doi:10.6342/NTU202203205

doi:doi:10.6342/NTU202203205

doi:doi:10.6342/NTU202203205

# List of Figures





doi:doi:10.6342/NTU202203205

doi:doi:10.6342/NTU202203205

doi:doi:10.6342/NTU202203205

doi:doi:10.6342/NTU202203205

doi:doi:10.6342/NTU202203205

doi:doi:10.6342/NTU202203205

# List of Tables





doi:doi:10.6342/NTU202203205

doi:doi:10.6342/NTU202203205

# Chapter 1

# Introduction

## 1.1 Belle Experiment

### 1.1.1 KEKB Accelerator

KEKB is a two-ring(3016 m), asymmetric-energy, electron(8-GeV) – positron(3.5-GeV) collider and is aiming at producing B meson pair as in a factory which serves as a beam producer in Belle experiment. This design produces center-of-mass energy at 10.58 GeV which is equal to the mass of the $\Upsilon(4S)$. The two rings cross at one point with a crossing angle $\pm 11$ rad in Tsukuba experiment hall, called the interaction point (IP), where electrons and positrons collide. The Belle detector surrounds the interaction point to collect the particle produced from collision. The following sections will introduce Belle detector. Fig 1.1 shows the configuration of KEKB accelerator.


doi:doi:10.6342/NTU202203205

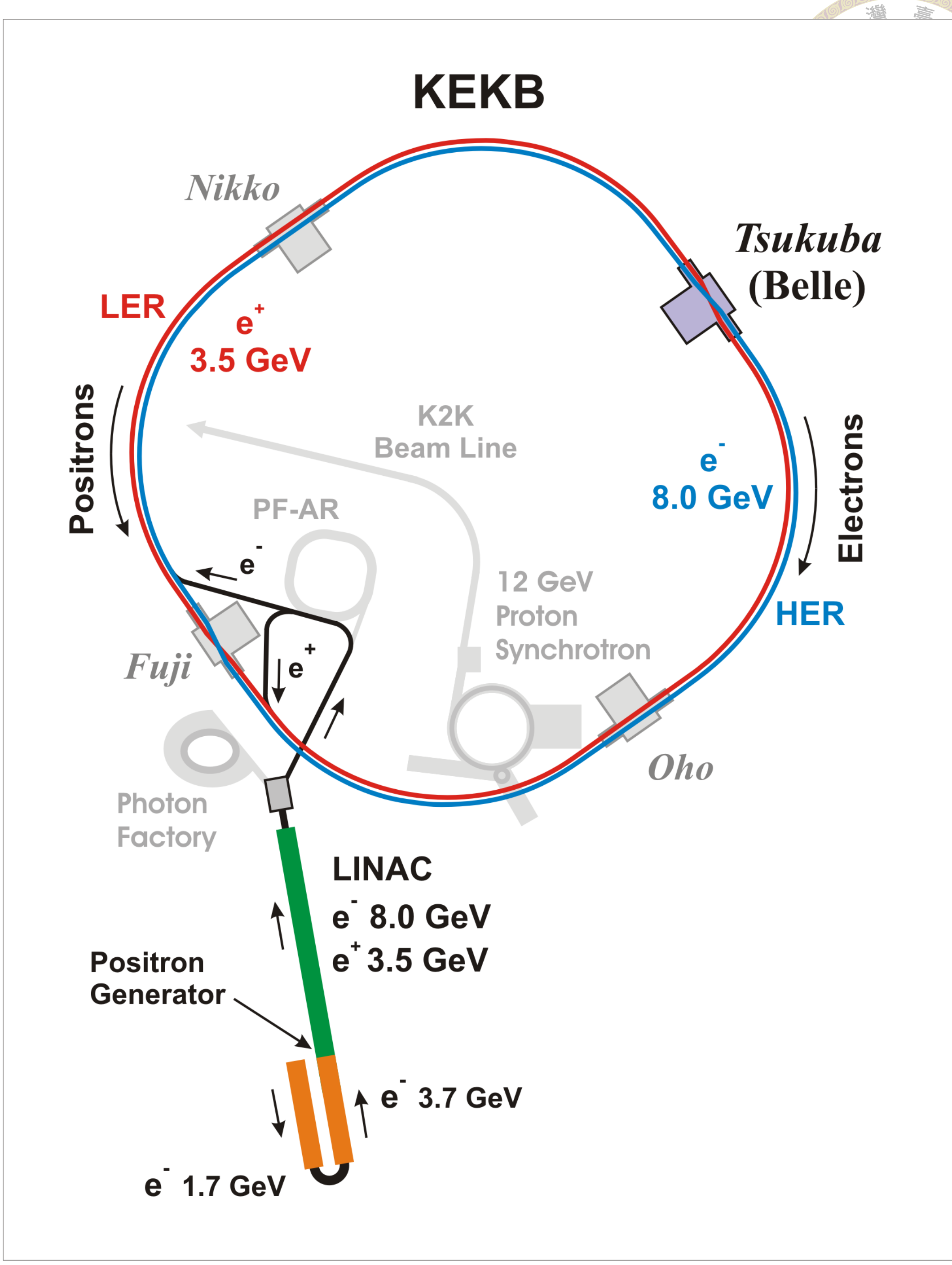


Figure 1.1: Configuration of KEKB accelerator

### 1.1.2 Belle Detector

The belle detector is configured around a 1.5T superconducting solenoid and iron structure surrounding the KEKB beams at the Tsukuba interaction region. The whole Belle detector consists of a group of sub-detectors which are SVD, EFC, CDC, ACC,



doi:doi:10.6342/NTU202203205

TOF, ECL and KLM. The configuration of Belle detector is shown in Fig 1.2.

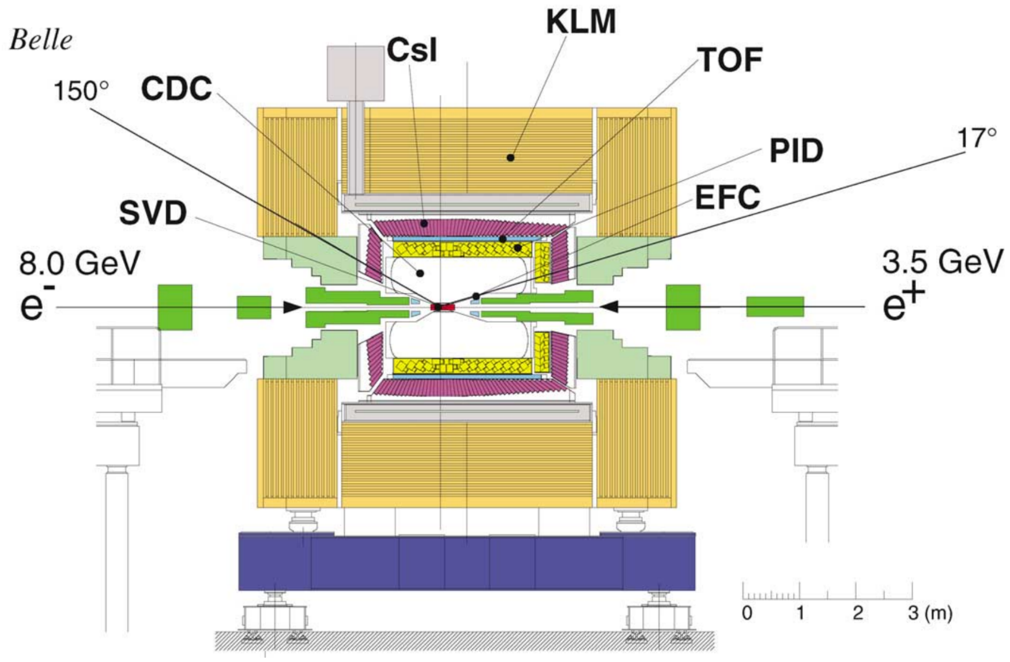


Figure 1.2: The configuration of Belle detector

#### 1.1.2.1 Beam Pipe

One of features of Belle experiment is the precise measurement of decay vertex. The whole design of beam pipe is focused on the main factors affecting the vertex detector which are multiple coulomb scattering in the beam-pipe wall and beam-induced heat. Thus, the minimization of the beam-pipe thickness and an active cooling system are necessary. The detailed numerical information of beam pipe is shown in Ref[1]. Fig 1.3 shows the cross-section and thickness parameters of beam pipe.



doi:doi:10.6342/NTU202203205

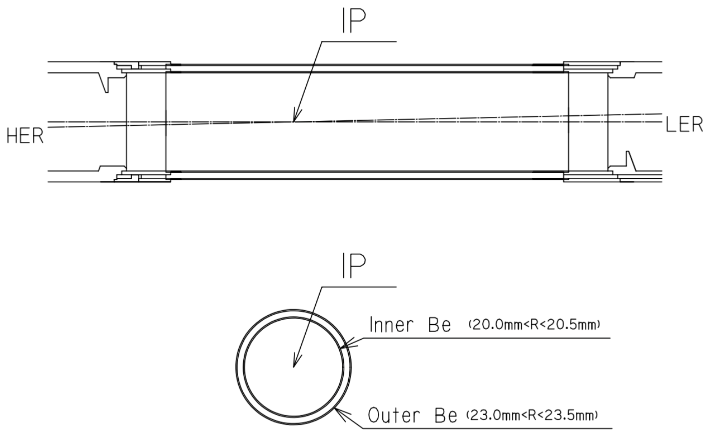


Figure 1.3: The cross-section of the beryllium beam pipe at the interaction point

#### 1.1.2.2 Extreme Forward Calorimeter (EFC)

In order to improve the experimental sensitivity to some specific physics decay like $B \to \tau\nu$, Extreme Forward Calorimeter (EFC) is designed to extend the polar angle coverage by ECL ($17^\circ < \theta < 150^\circ$). The EFC covered range is 6.4° to 11.5° in the forward direction and 163.3° to 171.2° in backward direction. In addition to expand EFC polar angle, EFC is required to serve as a beam mask to reduce backgrounds of CDC, and a beam monitor for KEKB control, also a luminosity monitor for the Belle experiment. EFC is made of BGO($Bi_4Ge_3O_{12}$) because of its radiation-hard property. The dimensional view of EFC is shown in Fig 1.4.


doi:doi:10.6342/NTU202203205

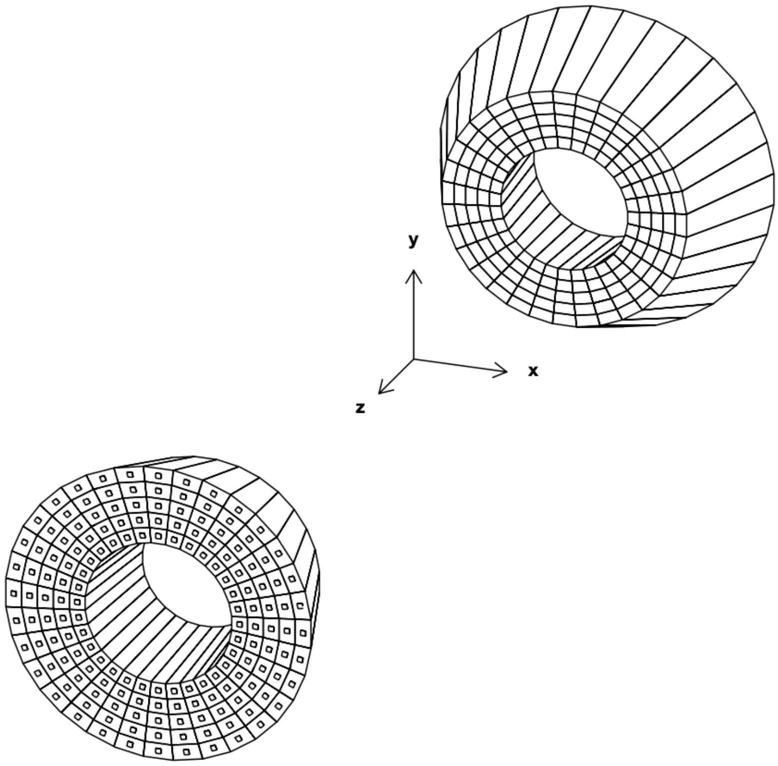


Figure 1.4: Dimensional view of EFC

#### 1.1.2.3 Silicon Vertex Detector (SVD)

Silicon Vertex Detector (SVD) is designed to measure the difference of z-vertex positions for B meson pairs which is a essential factor of CP violation measurement. Also, SVD is useful for measuring the vertex of particle decay like D and contributing to the tracking. The design of SVD is constraint by the multiple-Coulomb scattering, in particular, the innermost layer of the vertex detector must be placed as close to the interaction point as possible, the support structure must be low in mass but rigid, and high radiation-hard.


doi:doi:10.6342/NTU202203205

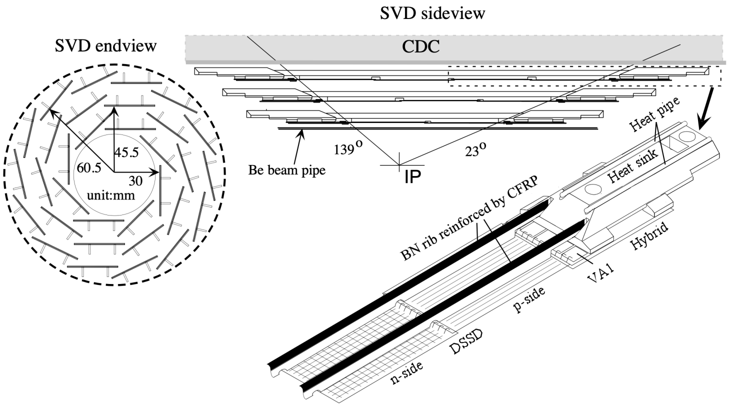


Figure 1.5: Detector configuration of SVD

The detailed numerical information of SVD is shown in Ref[1]. The configuration of SVD is shown in Fig 1.5. In 2003 summer, SVD2 is developed to replace SVD1 as a new vertex detector which included 4 layers with radii 20, 43.5, 70, 80mm and 6, 12, 18, 18 ladders in each layer respectively.

#### 1.1.2.4 Central Drift Chamber (CDC)

Central Drift Chamber (CDC) is designed to reconstruct charged particle track which used to precisely measure particle momentum. Also, CDC is expected to provide the important charged particle identification information which is $\frac{dE}{dx}$ measurements. The detailed numerical information of CDC is shown in Ref[1]. Fig 1.6 shows the configuration of CDC.


doi:doi:10.6342/NTU202203205

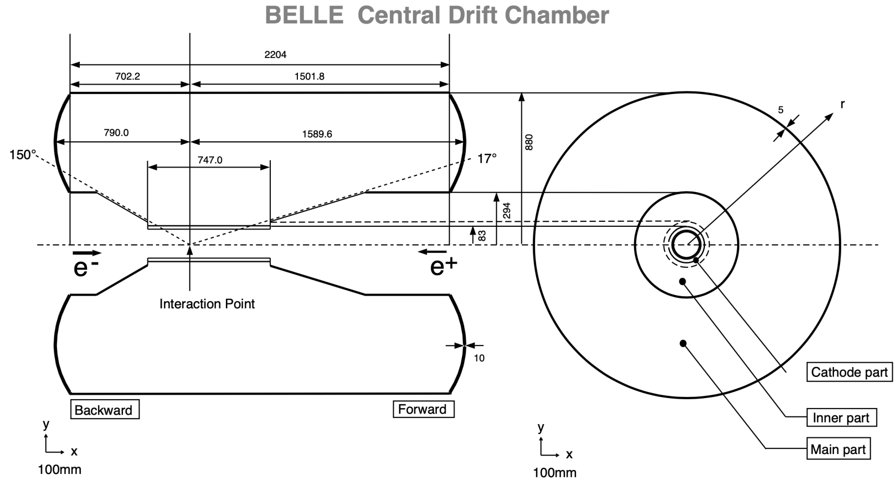


Figure 1.6: Overview of CDC structure

All planned physics measurement require a momentum resolution about $\sigma_{p_t}/p_t \sim 0.5\%\sqrt{1+p_t^2}$ for all measurable charged particle with $p_t > 100MeV/c$, and because the momentum of the majority of decay particles from B meson momentum is lower than 1 GeV/c, resolution is easily affected by multiple coulomb scattering. Therefore, low-Z gas is chosen to be the material of drift chamber to minimize multiple scattering. The chamber gas is a mixture of 50% helium and 50% ethane which has a long radiation length.


doi:doi:10.6342/NTU202203205

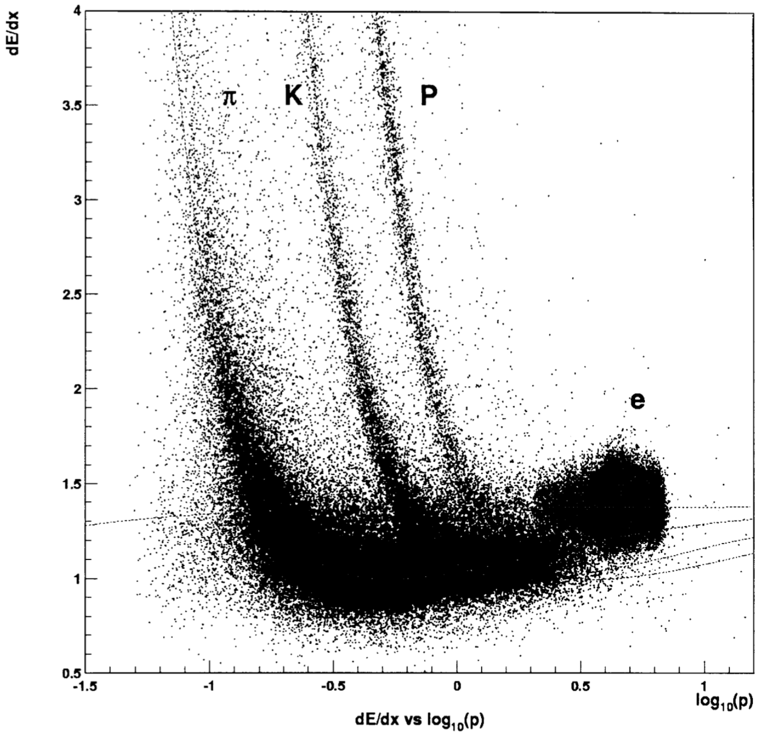


Figure 1.7: $\frac{dE}{dx}$ vs. momentum observed in collision data

#### 1.1.2.5 Aerogel Cherenkov Counter System (ACC)

Aerogel Cherenkov Counter System (ACC) is designed to provide the information for particle identification which has the ability to distinguish $\pi^{\pm}$ from $K^{\pm}$ also extend the momentum coverage beyond the reach of $dE/dx$ and time-of-flight measurement. Fig 1.8 shows the configuration of ACC at the central part of Belle experiment. The detailed numerical information of ACC is shown in Ref[1].


doi:doi:10.6342/NTU202203205

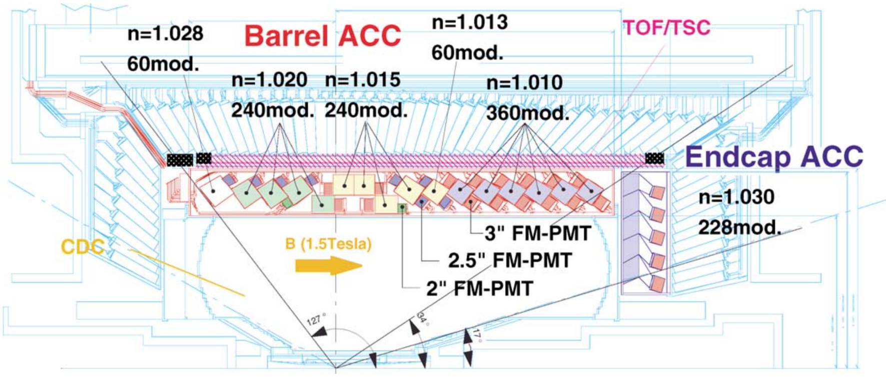


Figure 1.8: The arrangement of ACC at the central part of Belle detector

The refractive indices of aerogels are chosen to be between 1.01 to 1.03 based on their polar angle for the better performance of $\pi^{\pm}$ $K^{\pm}$ separation for whole kinematic range. Fig 1.9 shows a typical ACC module, one or two fine mesh-type photomultiplier tubes (FM-PMTs) are attached directly to the aerogels at the sides of the box to collect Cherenkov light effectively, .


doi:doi:10.6342/NTU202203205

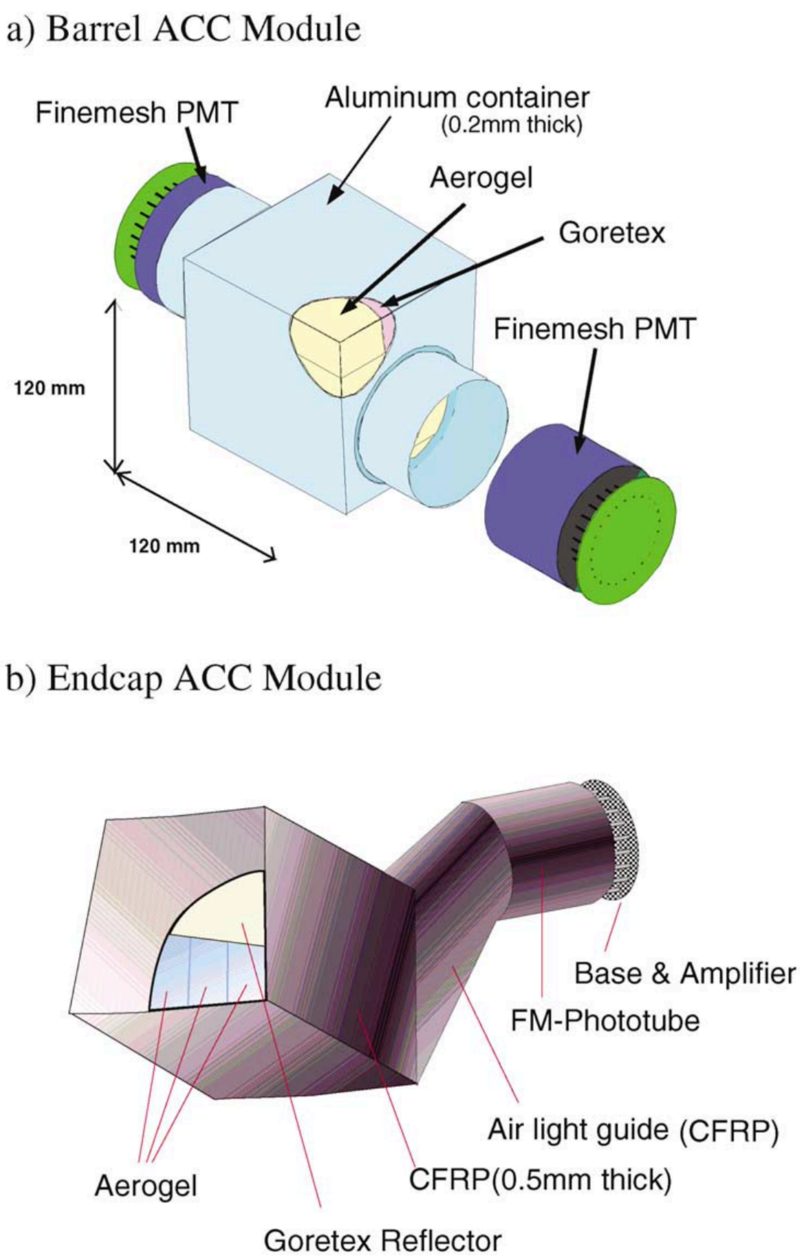


Figure 1.9: Schematic drawing of a typical ACC counter module: (a) barrel and (b) endcap ACC.

#### 1.1.2.6 Time of Flight (TOF)

Time-of-flight counters (TOF) is designed to measure the flight time of particles which is very powerful information for particle identification. With a 1.2 m flight path, the time resolution of the TOF system is about 100 ps for particle momentum lower than 1.2 $GeV/c$ which covers 90% of the particles in $\Upsilon(4S)$ decay. The TOF counters also pro-



doi:doi:10.6342/NTU202203205

vide fast timing signals for the trigger system, and TOF signals trigger frequency must be under 70 kHz to prevent pile-up in the trigger queue. In order to achieve this requirement, the TOF counters should be augmented by thin trigger scintillation counters (TSC) based on simulation studies.

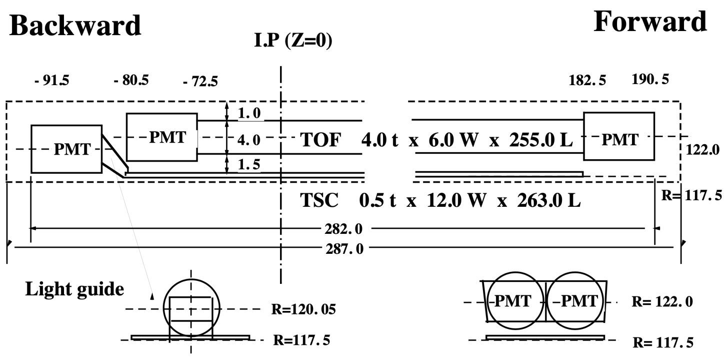


Figure 1.10: Dimensions of a TOF/TSC module

Fig 1.10 shows the modules configuration of TOF, and those modules are individually connected on the inner wall of the barrel ECL container.

#### 1.1.2.7 Electromagnetic Calorimeter (ECL)

Electromagnetic Calorimeter (ECL) is designed to detect the photon from B meson decay with high efficiency and good resolution in energy and position. The energy resolution plays important role in the design propose of ECL. The decay modes like $B \to K^*\gamma$ and $B \to \pi^0\pi^0$ produce photons energies higher than 4 GeV level and require good energy resolution to eliminate background from other channels. Also, good electromagnetic energy resolution performs better hadron rejection, and the separation of two nearby photons produced by high momentum $\pi^0$.

In order to to achieve above requirements, ECL consists of CsI crystal which has a large photon yield with silicon photodiode readout. The whole calorimeter covers polar angle between 17° and 150° which shown in Fig 1.11.


doi:doi:10.6342/NTU202203205

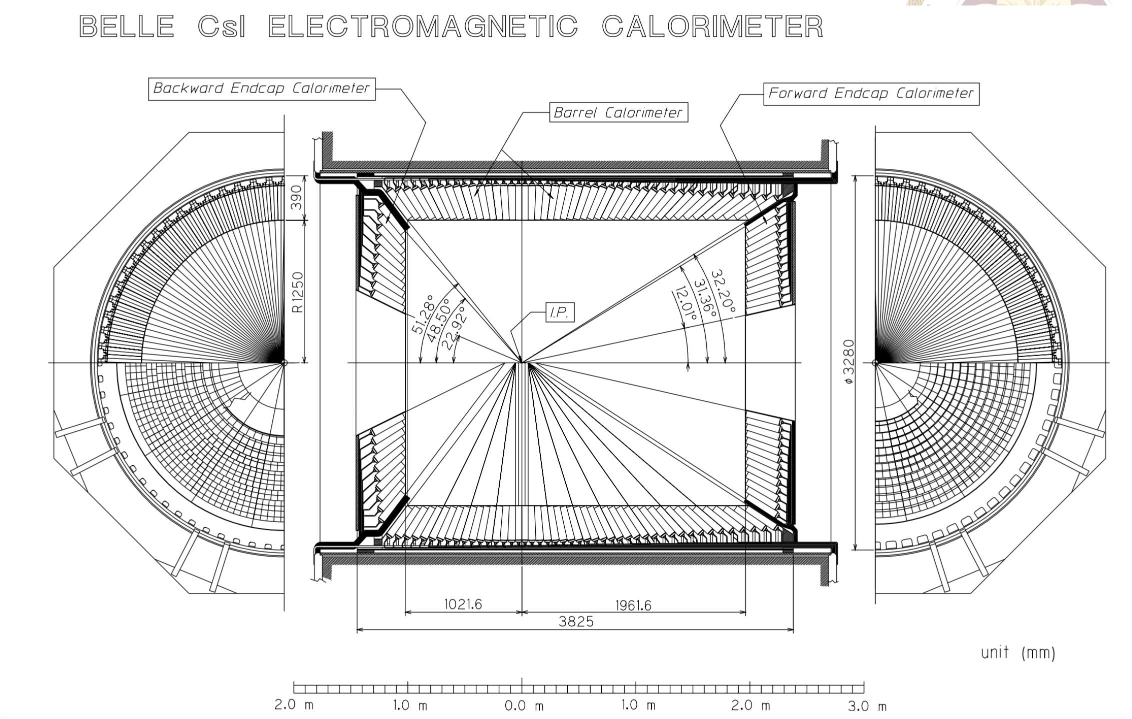


Figure 1.11: Overall configuration of ECL

#### 1.1.2.8 $K_L$ and $\mu$ Detection System (KLM)

$K_L$ and muon detection system (KLM) is designed to identify $K_L$ and muon with high efficiency over a broad momentum range greater than 600 MeV/c. When $K_L$ interacts with in the iron of KLM will produces a interaction shower which can provide the direction of $K_L$. Because of the fluctuation of the size of shower shape , we can't measure $K_L$ energy precisely. In addition to $K_L$ detection, The multiple layers of charged particle detectors and iron provide the information of discrimination between muon and charged hadron.



doi:doi:10.6342/NTU202203205

## 1.2 Motivation

### 1.2.1 $b \to s$ Transition Decay

There are several theoretical predictions[2][3] based on QCD model for the branching fraction of $B^0 \to p\bar{\Sigma}^0\pi^-$ and $B^0 \to p\bar{\Lambda}\pi^-$ and showing $B^0 \to p\bar{\Sigma}^0\pi^-$ has larger branching fraction than $B^0 \to p\bar{\Lambda}\pi^-$. The previous Belle measurement of $B^0 \to p\bar{\Lambda}\pi^-$ showed the branching fraction deviation which make us have better theoretical approach to predict the similar channel $B^0 \to p\bar{\Sigma}^0\pi^-$ about $1.6 \times 10^{-6}$. In our analysis, we are interested in the accuracy of QCD prediction for $B^0 \to p\bar{\Sigma}^0\pi^-$. Fig 1.12 shows the Feynman diagram of $B^0 \to p\bar{\Sigma}^0\pi^-$.

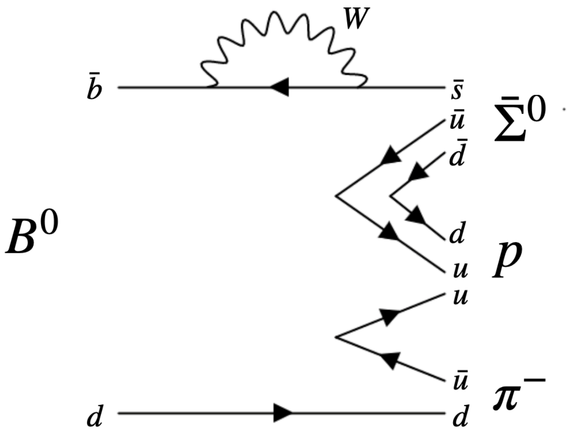


Figure 1.12: A possible $b \to s$ penguin diagram of $B^0 \to p\bar{\Sigma}^0\pi^-$

### 1.2.2 Threshold Enhancement Study

In previous Belle result[4] for $B^0 \to p\bar{\Lambda}\pi^-$ channel, we observed the distribution of invariant mass of baryonic pair has a peak near the position of summation of two baryons mass instead of flat distribution. Such phenomenon called ”threshold enhancement”, and the theoretical prediction in Ref[5] based on $B^0 \to p\bar{\Lambda}\pi^-$ observation indicates the same phenomenon in $B^0 \to p\bar{\Sigma}^0\pi^-$ channel. Fig 2.2 shows $M_{p\bar{\Lambda}}$ distribution for $B^0 \to p\bar{\Lambda}\pi^-$ in previous Belle study in Ref[4] and theoretical prediction of $M_{p\bar{\Lambda}}$ distribution for baryonic decay channel in Ref[5]


doi:doi:10.6342/NTU202203205

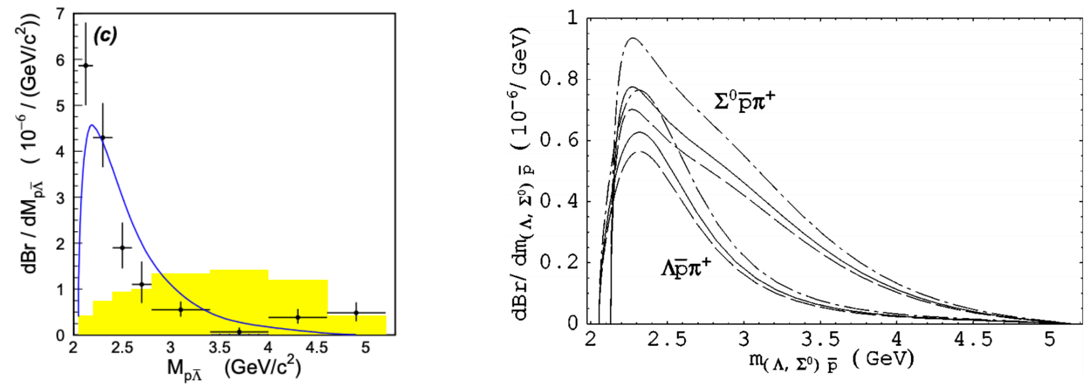


Figure 1.13: $M_{p\bar{\Lambda}}$ distribution for $B^0 \to p\bar{\Lambda}\pi^-$ with $414 fb^{-1}$ Belle data in previous Belle study (Left).The shaded distribution shows the expectation from a phase-space MC simulation, and the blue line is the function of baryon-antibaryon pair mass. Theoretical prediction of $M_{p\bar{\Lambda}}$ distribution for baryonic decay channel (Right)

### 1.2.3 cos$\theta_p$ Asymmetry

The other stunning result of previous $B^0 \to p\bar{\Lambda}\pi^-$ is the cos$\theta_p$ distribution anomaly, $\theta_p$ is the angle between the proton direction and the oppositely charged meson direction in baryon pair rest frame which shown in Fig 1.14. Fig 1.15 in Ref[4] shows the signal events close to -1 which indicates the proton moves faster than the accompany $\Lambda$. That is against the intuitive $b \to sg$ picture of the $B^0 \to p\bar{\Lambda}\pi^-$ decay that the s quark should be energetic. So we want to see this anomaly in $B^0 \to p\bar{\Sigma}^0\pi^-$ and use more data to confirm the cos$\theta_p$ distribution of $B^0 \to p\bar{\Lambda}\pi^-$.

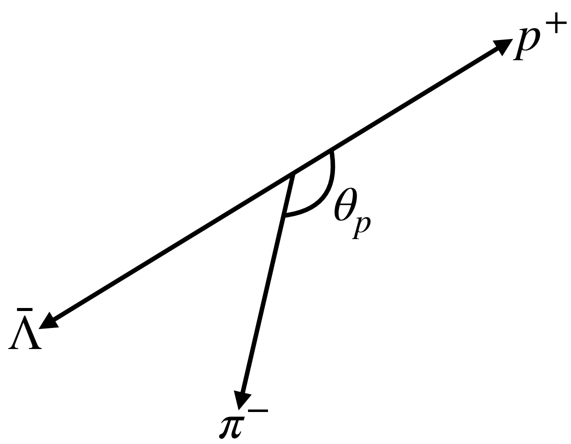


Figure 1.14: Baryon pair rest frame $\theta_p$ schematic diagram in $B^0 \to p\bar{\Lambda}\pi^-$ channel


doi:doi:10.6342/NTU202203205

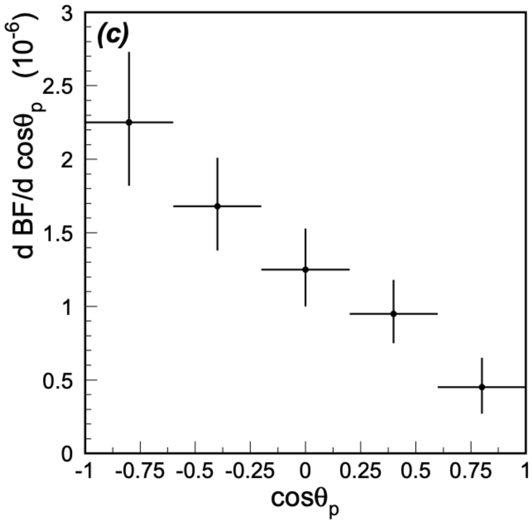


Figure 1.15: The distribution of $cos\theta_p$ for $B^0 \to p\bar{\Lambda}\pi^-$ in previous Belle study



doi:doi:10.6342/NTU202203205

doi:doi:10.6342/NTU202203205

# Chapter 2

# Event Reconstruction and Selection

## 2.1 Data Sample

### 2.1.1 Belle Data Sample

In our analysis, we used full Belle data set collected by Belle detector at the KEKB asymmetric-energy $e^+e^-$ collider around $\Upsilon(4S)$ resonance, with the integrated luminosity of 711 $fb^{-1}$. The total number of $B\bar{B}$ event is 771.581$\pm$10.566 million.

### 2.1.2 Signal Monte Carlo

All the signal Monte Carlo samples are generated by the `EvtGen` package[6] , and the response of Belle detector is simulated by the `GEANT3` package[7]. The on-resonance experiment including Exp7 to Exp65 are generated with corresponding proportions. Our each signal event of $B\bar{B}$ pair only one of them will decay to our signal channel, and the other one will decay generically. Due to our ignorance of true physics of signal and comparison the efficiency and fitting variables distribution, we generate two types signal Monte Carlo which are threshold enhancement and phase space decay. For the signal Monte Carlo following threshold enhancement decay, we define the virtual particle $X_{bb}$ listed in Tab 2.3 to mimic baryon pair $p\bar{\Lambda}$ and $p\bar{\Sigma}$ in threshold enhancement. For the signal Monte Carlo following phase space decay, we just make our signal directly decay to three body. The details of generation of Monte Carlo are listed in Tab 2.1 and Tab 2.2. In our analysis,


doi:doi:10.6342/NTU202203205

we assume our signal events all follow threshold enhancement decay, and consider the difference of two type decay as systematic uncertainty finally. In order to estimate expect yield, we assume our signal branching fraction is $1.9 \times 10^{-6}$. Fig 2.1. shows the difference between threshold enhancement and phase space in the distribution of invariant mass of baryon pair.

| Decay | Model used | Events generated |
|---|---|---|
| $\Upsilon(4S) \to B^0 \bar{B}^0$ | VSS BMIX dm | $771 \times 10^3$ |
| $B^0 \to X_{bb} \pi^-$ | PHOTOS PHSP | |
| $X_{bb} \to p \bar{\Sigma}^0$ | PHOTOS PHSP | |
| $\Upsilon(4S) \to B^0 \bar{B}^0$ | VSS BMIX dm | $771 \times 10^3$ |
| $B^0 \to X_{bb} \pi^-$ | PHOTOS PHSP | |
| $X_{bb} \to p \bar{\Lambda}$ | PHOTOS PHSP | |

Table 2.1: EvtGen decay models for signal MC sample with threshold enhancement

| Decay | Model used | Events generated |
|---|---|---|
| $\Upsilon(4S) \to B^0 \bar{B}^0$ | VSS BMIX dm | $771 \times 10^3$ |
| $B^0 \to p \bar{\Sigma}^0 \pi^-$ | PHOTOS PHSP | |

Table 2.2: EvtGen decay models for signal MC sample with phase space

| Pseudo-particle | $(p\bar{\Lambda})$ | $(p\bar{\Sigma}^0)$ |
|---|---|---|
| Mass (GeV/c$^2$) | 2.05 | 2.18 |
| Mass width (GeV/c$^2$) | 0.3 | 0.3 |

Table 2.3: The mass and mass width of pseudo-particle for simulate threshold enhancement


doi:doi:10.6342/NTU202203205

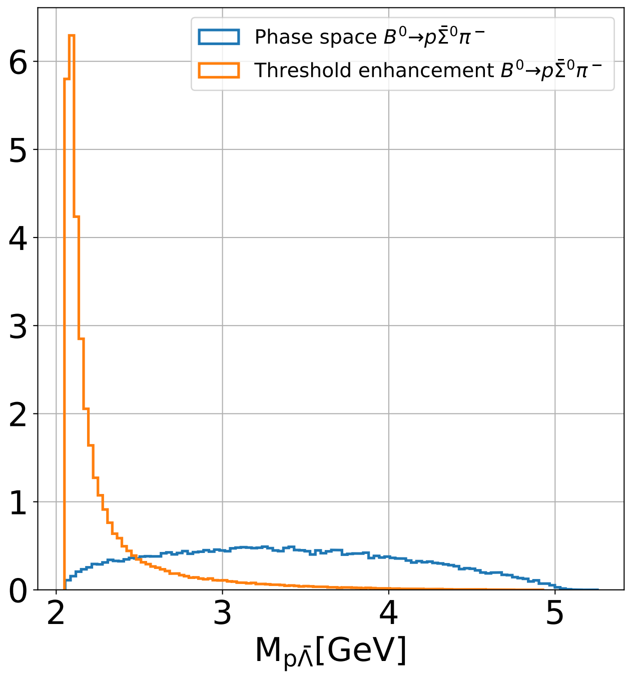


Figure 2.1: Comparison of $M_{p\bar{\Lambda}}$ normalized distribution for signal MC in phase space and threshold enhancement

### 2.1.3 Background Monte Carlo

Background Monte Carlo includes generic $B\bar{B}$, the continuum $q\bar{q}$ and rare B decay. The dominated background is expected to be continuum $q\bar{q}$. Generic $B\bar{B}$ and rare decay include mixed and charged but excluded our signal channels. Those background samples are officially generated by Belle collaboration with `EvtGen` and `GEANT`-based simulation. The details of background type and events generated are listed in Tab 2.4.

| Background type | Physics type | Events generated |
|---|---|---|
| Generic $B\bar{B}$ | $b \to c$ transition mixed and charged | 10 × data |
| Continuum $q\bar{q}$ | $e^+e^- \to q\bar{q}(u\bar{u}, d\bar{d}, c\bar{c}, s\bar{s})$ | 6 × data |
| Rare B decay | $b \to s$ transition mixed and charged | 50 × data |

Table 2.4: Type of background MC used


doi:doi:10.6342/NTU202203205

## 2.2 Reconstruction of Candidate

Because the energy of photon radiated from $\Sigma$ particle is as low as background photon which is hard to efficiently classify background and signal photons. To avoid this problem, we only reconstruct signal with charged tracks like $p^{\pm}$ and $\pi^{\pm}$. In our analysis, we partially reconstructed $B^0 \to p\bar{\Sigma}^0\pi^-$ candidates with $p$, $\bar{\Lambda}$, $\pi^{\pm}$, and measure $B^0 \to p\bar{\Lambda}\pi^-$ simultaneously as a control sample to make sure the precision of measurement of $B^0 \to p\bar{\Sigma}^0\pi^-$. Fig 2.2 shows the distribution of photon energy for signal and background.

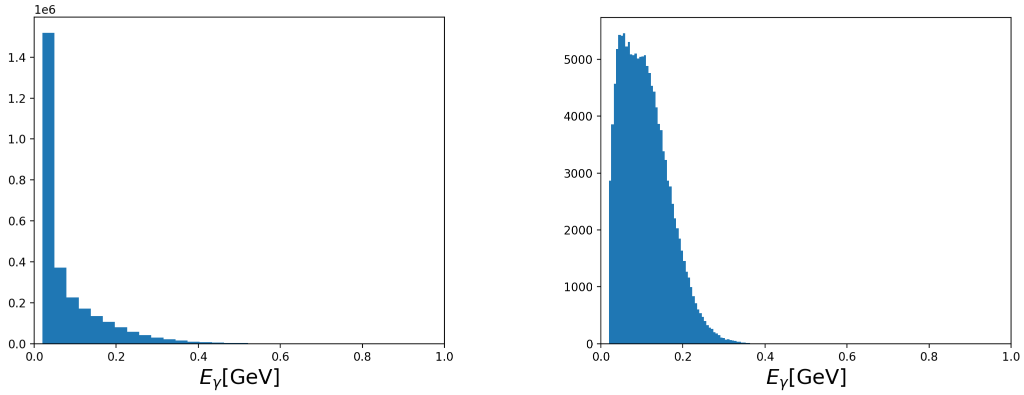


Figure 2.2: Photon energy for self-crossfeed background(Left) and signal photon(Right)

## 2.3 Event Selection

### 2.3.1 $p^{\pm}$ and $\pi^{\pm}$ Selection

The charged track selection criteria are based on the information obtained from the tracking system (SVD + CDC) and the hadron identification system (CDC + ACC + TOF). We reject the highly electron-like ($\mathscr{L}_e > 0.95$) and muon-like ($\mathscr{L}_\mu > 0.95$) track first, also require the impact parameters of charged track in radial direction $|\Delta r| < 0.3$ cm and in beam direction $|\Delta z| < 4$ cm for $\pi^{\pm}$, and $|\Delta r| < 0.3$ cm $|\Delta z| < 2$ cm for proton. For the proton likelihood ratio selection, we set selection criteria $\mathscr{L}_p/(\mathscr{L}_p + \mathscr{L}_K) > 0.6$ and $\mathscr{L}_p/(\mathscr{L}_p + \mathscr{L}_\pi) > 0.6$ to choose the proton-like track. For $\pi^{\pm}$ likelihood ratio selection, we set selection criteria $\mathscr{L}_\pi/(\mathscr{L}_\pi + \mathscr{L}_K) > 0.6$ to choose $\pi$-like track.


doi:doi:10.6342/NTU202203205

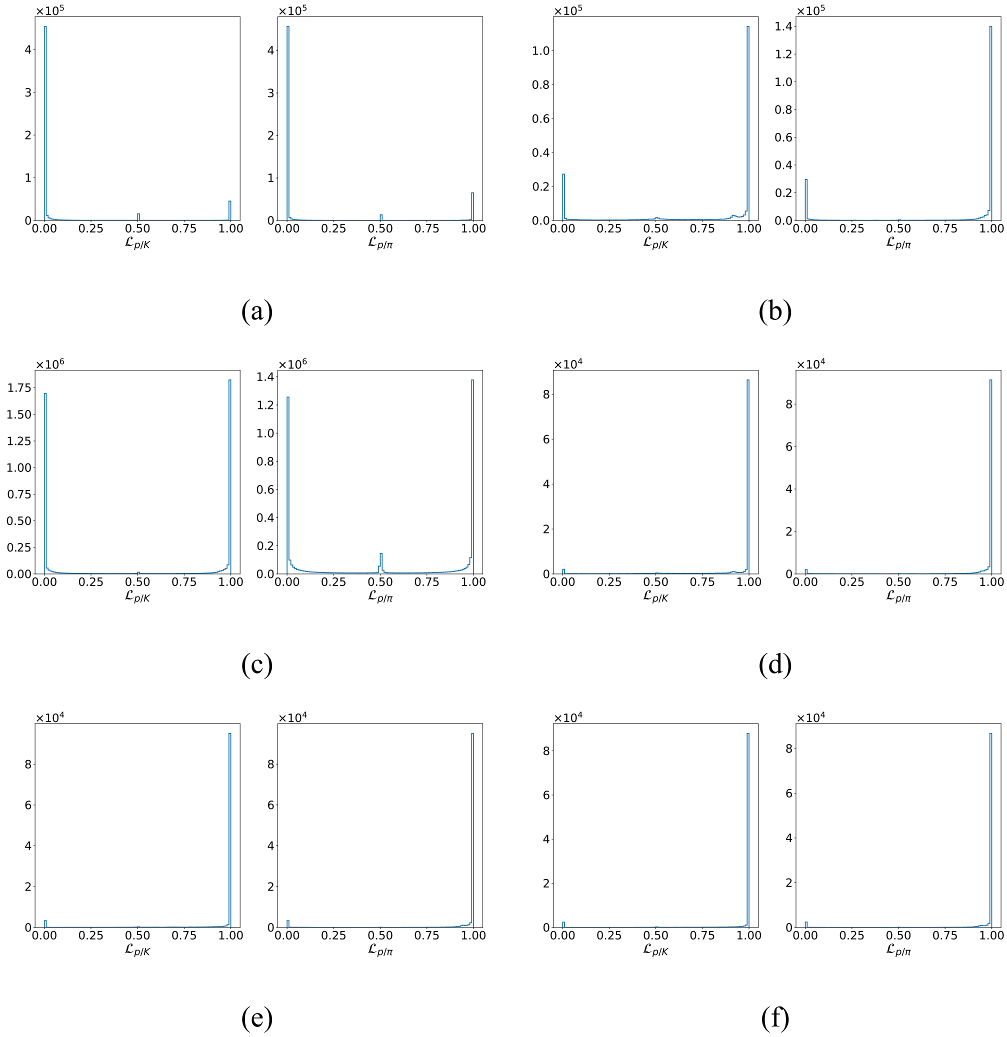


Figure 2.3: Proton likelihood ratio of Lambda daughter before pre-selection cut (a) Generic $B\bar{B}$ (b) Rare decay (c) Continuum $q\bar{q}$ (d)$B^0 \to p\bar{\Sigma}^0\pi^-$ in PHSP (e) $B^0 \to p\bar{\Lambda}\pi^-$ (f) $B^0 \to p\bar{\Sigma}^0\pi^-$ in TE

### 2.3.2 $\Lambda$ Selection

The $\Lambda$ selection is using `MdstVee2` bank. We apply `goodlambda` selection to choose truth $\Lambda$ ((`goodLambda()`>0) ) and the details of good$\Lambda$ index is described in Belle Note 684[8]. The invariant mass of $\Lambda$ candidate is required to be within 1.111 GeV/c$^2$ to 1.121 GeV/c$^2$, and the criteria of proton likelihood ratio of $\Lambda$'s daughter proton is set to be greater than 0.6 ($\mathscr{L}_p/(\mathscr{L}_p+\mathscr{L}_K) > 0.6$ and $\mathscr{L}_p/(\mathscr{L}_p+\mathscr{L}_\pi) > 0.6$) in order to reduce any possible combinatorial background. The selection performance is shown in Tab 2.5.


doi:doi:10.6342/NTU202203205

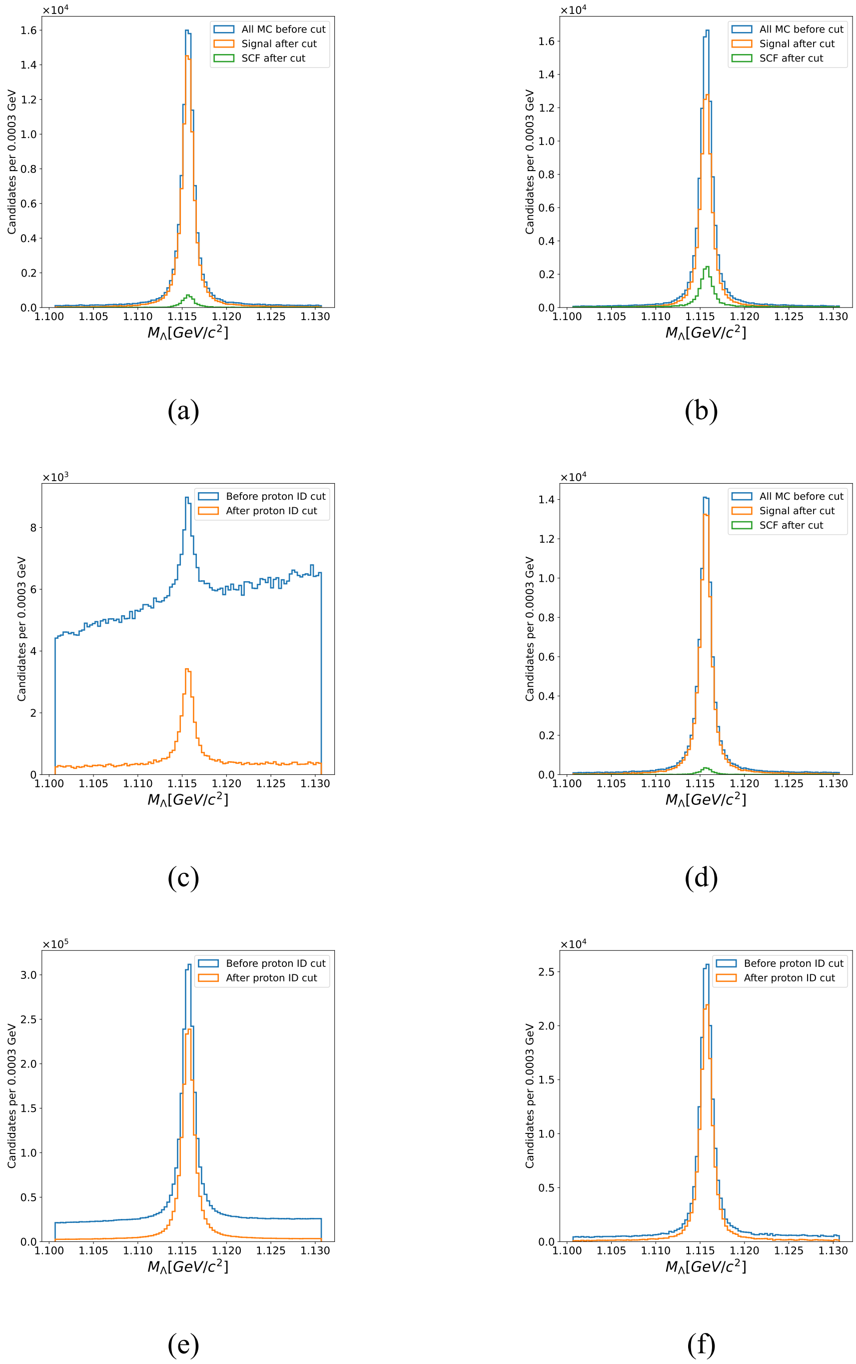


Figure 2.4: $M_{p\pi}$ distribution before and after proton and $\pi$ ID selection (a)$B^0 \to p\bar{\Lambda}\pi^-$ (b) PHSP $B^0 \to p\bar{\Sigma}^0\pi^-$ (c) Generic $B\bar{B}$ (d)TE $B^0 \to p\bar{\Sigma}^0\pi^-$ (e) Continuum $q\bar{q}$ (f) Rare decay

| Type | Before | After |
|---|---|---|
| PHSP signal efficiency | 13.96% | 12.99% |
| TE signal efficiency | 18.39% | 16.13% |

Table 2.5: Performance of $\Lambda$ selection


doi:doi:10.6342/NTU202203205

## 2.4 Kinematic Variables

The $B^0$ candidates are reconstructed from four momentum combination of $p\bar{\Lambda}\pi^-$, we use distribution of two kinematic variables in the CM frame to classify our signal candidates from background : the beam-energy-constrained mass $M_{bc}$, and energy difference $\Delta E$ which are given as :

$$M_{bc} = \sqrt{E_{beam}^2 - p_{recon}^2} \tag{2.1}$$

and

$$\Delta E = E_{beam} - E_{recon} \tag{2.2}$$

where $E_{beam}$ is beam energy, $p_{recon}$, $E_{recon}$ are the momentum and energy of our $B^0$ candidates. The distribution of two variables of signal MC is shown in Fig 2.5.

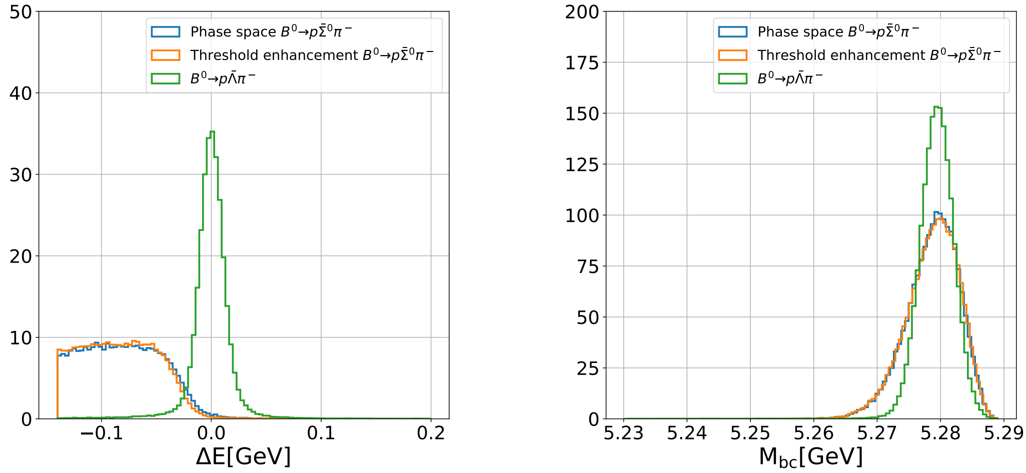


Figure 2.5: Comparison of ΔE vs $M_{bc}$ normalized histogram between PHSP and TH for $B^0 \to p\bar{\Sigma}^0\pi^-$

The fitting region and the signal region are shown in Fig 2.6. The whole region is fitting region and the red region is signal region.


doi:doi:10.6342/NTU202203205

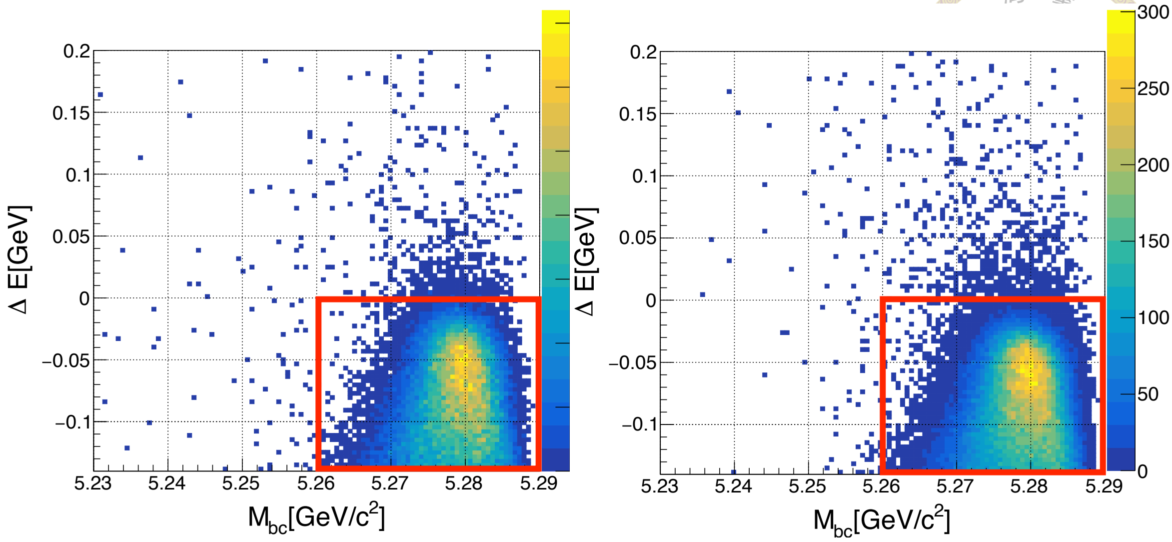


Figure 2.6: $\Delta E$ and $M_{bc}$ scattering plot for $B^0 \to p\bar{\Sigma}^0\pi^-$ following phase space decay(Left) and $B^0 \to p\bar{\Sigma}^0\pi^-$ following threshold enhancement(Right). The red line is signal region which is $-0.14$ GeV $< \Delta\text{E} < 0.00$ GeV and 5.26 GeV$/\text{c}^2 < \text{M}_{\text{bc}} < 5.29$ GeV$/\text{c}^2$.

## 2.5 Selection Summary

| | Selection |
|---|---|
| Charged Particle | $\mathscr{L}_{p/\pi} > 0.6$ $\mathscr{L}_{p/K} > 0.6$ for $p^{\pm}$<br>$\mathscr{L}_{\pi/K} > 0.6$, $\mathscr{L}_{e} < 0.95$, $\mathscr{L}_{\mu} < 0.95$ for $\pi^{\pm}$<br>$\lvert\Delta r\rvert < 0.3$ cm , $\lvert\Delta z\rvert <4$ cm for $\pi^{\pm}$ come from B candidate<br>$\lvert\Delta r\rvert < 0.3$ cm , $\lvert\Delta z\rvert <2$ cm for $\pi^{\pm}$ come from B candidate |
| $\Lambda$ Selection | `goodlambda`$> 0$<br>1.111 GeV$/\text{c}^2 < \text{M}_{\text{p}\pi} < 1.121$ GeV$/\text{c}^2$<br>$\mathscr{L}_{p/\pi} > 0.6$ $\mathscr{L}_{p/K} > 0.6$ for $p^{\pm}$ from $\Lambda$ |
| Selection Region | $-0.14$ GeV $< \Delta\text{E} < 0.2$ GeV ,<br>5.23 GeV$/\text{c}^2 < \text{M}_{\text{bc}} < 5.29$ GeV$/\text{c}^2$ |
| Signal box for $B^0 \to p\bar{\Lambda}\pi^-$ | $-0.05$ GeV $< \Delta\text{E} < 0.05$ GeV ,<br>5.27 GeV$/\text{c}^2 < \text{M}_{\text{bc}} < 5.29$ GeV$/\text{c}^2$ |
| Signal box for $B^0 \to p\bar{\Sigma}^0\pi^-$ | $-0.14$ GeV $< \Delta\text{E} < 0.00$ GeV ,<br>5.26 GeV$/\text{c}^2 < \text{M}_{\text{bc}} < 5.29$ GeV$/\text{c}^2$ |

Table 2.6: Summary of Selection


doi:doi:10.6342/NTU202203205

# Chapter 3

# Background Study

## 3.1 Overview of Background Study

In our analysis, there are three main type background which shown in Fig 3.1: the generic $B\bar{B}$ spherical events and the jet-like continuum $q\bar{q}$ events and rare B decay. The dominated background is expected to be continuum $q\bar{q}$. In generic $B\bar{B}$ background, we apply $\Lambda_c$ veto to eliminate the peaking background formed by $B^0 \to p\Lambda_c^-$ channel in sec 4.4. Also, we study the rare decay MC to evaluate the possibility of peaking background formed by rare decay.

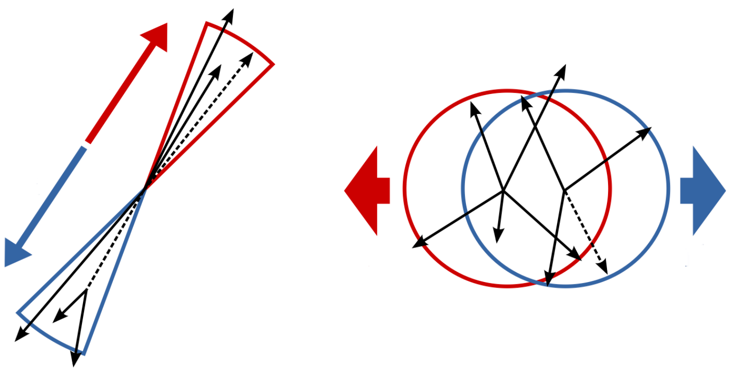

Figure 3.1: Background schematic diagram, LHS is continuum $q\bar{q}$ and RHS is generic $B\bar{B}$



doi:doi:10.6342/NTU202203205

## 3.2 Continuum Suppression

The dominated background is expected to be continuum $q\bar{q}$. In contrast of generic $B\bar{B}$ and rare B decay, continuum $q\bar{q}$ can be well-distinguished by their shape variables, and we hire a multivariate package which is based on neural network named NeuroBayes[9] to classify our signal and background. The following subsections are the details of training input variables, the output of NeuroBayes vary from -1 to +1, where the value being close to +1 is signal-like, -1 is background-like. Fig 3.2 shows the normalized output of NeuroBayes. We determine the cut of NeuroBayes output to optimize the proportion of signal and background by figure of merit (FOM).

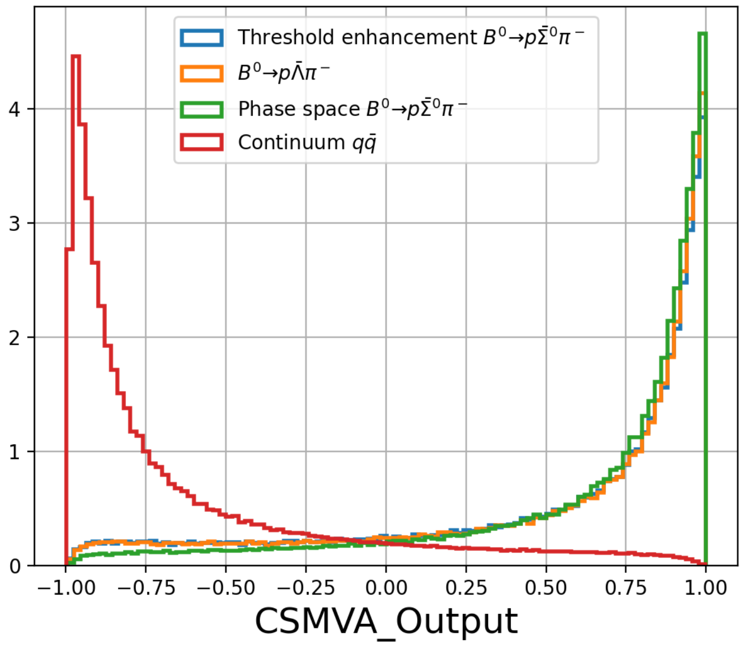


Figure 3.2: Normalized MVA output

### 3.2.1 Sideband Data and Monte Carlo Comparison

To make sure there is no significant discrepancy of performance of CSMVA output between data and Monte Carlo, we compare the CSMVA output of sideband data ($\Delta E$ >0.1(GeV)) with sideband continuum $q\bar{q}$, and the result is shown in Fig 3.3.


doi:doi:10.6342/NTU202203205

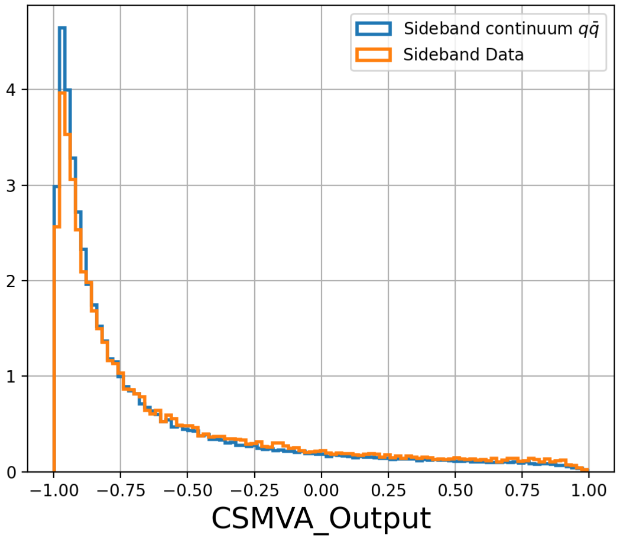


Figure 3.3: Comparison of `CSMVA` output between sideband data and sideband continuum $q\bar{q}$ with normalized histogram

### 3.2.2 $\Delta Z$

$\Delta Z$ is the vertex difference between B candidate and accompanying B. Because of color confinement, there is no free quark which means $\Delta Z$ of $q\bar{q}$ event is narrower than $B\bar{B}$. Fig 3.4 shows the $\Delta Z$ distribution of $B^0 \to p\bar{\Sigma}^0\pi^-$ signal and continuum background.

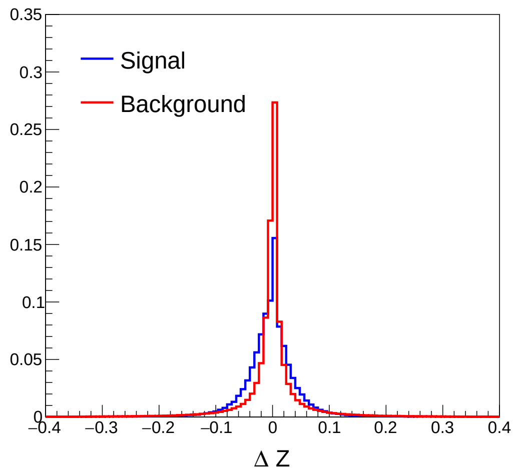


Figure 3.4: The normalized distribution of $\Delta Z$ for signal and background



doi:doi:10.6342/NTU202203205

### 3.2.3 $cos\theta_B$

$\theta_B$ is the angle between reconstructed B flight direction in the beam axis in the $\Upsilon(4S)$ rest frame. Since $\Upsilon(4S)$ is vector particle (spin=1) and $B\bar{B}$ are two pseudoscalar particles (spin=0), so the angle distribution of $\theta_B$ can be represented by $1-cos^2\theta_B$, and the distribution of $q\bar{q}$ is approximately uniform. The distribution difference of signal and continuum background is shown in Fig 3.5 .

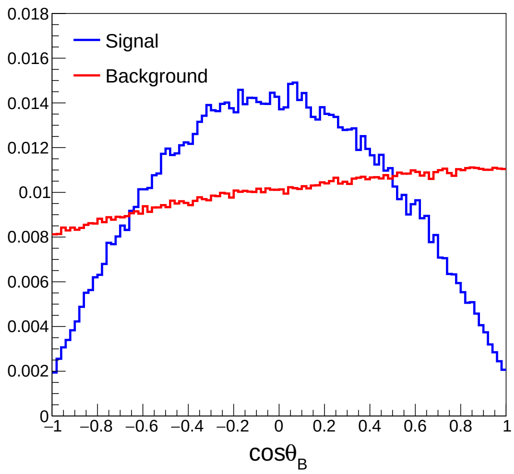


Figure 3.5: The normalized distribution of $cos\theta_B$ for signal and background

### 3.2.4 Thrust angle

Thrust angle is the angle between two thrust axis. One of thrust axis is obtained from the momentum of B candidate, and the other is constructed by remaining particles in event. The definition of thrust axis is given as

$$T = max(\vec{T}) = max\frac{\sum_i |\vec{p}_i \cdot \vec{T}|}{\sum_i |\vec{p}_i|} \tag{3.1}$$

where $\vec{p}_i$ is momentum of i-th particle in B candidate or rest of event. The distribution of $cos\theta_{thrust}$ will be peaking near $\pm1$ for continuum events because of their jet-like event shape, and for generic events $cos\theta_{thrust}$ will be uniform due to the spherical event shape. The distribution of $cos\theta_{thrust}$ is shown in Fig 3.6.



doi:doi:10.6342/NTU202203205

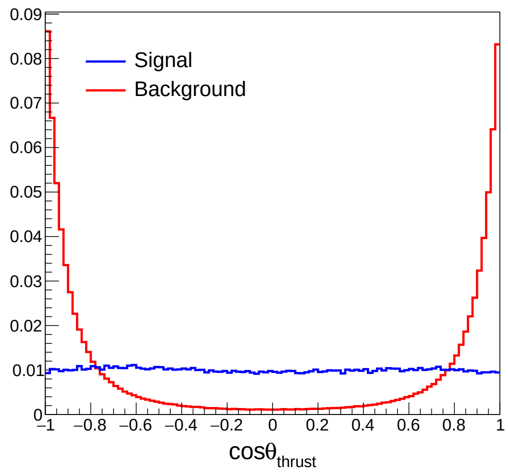


Figure 3.6: The normalized distribution of $cos\theta_{thrust}$ for signal and background

### 3.2.5 Sphericity

Sphericity is the measurement of how closely the shape of an object approaches that of a mathematically perfect sphere. Therefore, the distribution of generic B decay is closer to +1 than continuum $q\bar{q}$ event. Fig 3.7 shows the sphericity distribution of signal and continuum background normalized histogram. The formula of sphericity tensor is given as

$$S^{\alpha,\beta} = \frac{\sum_i p_i^{\alpha} p_i^{\beta}}{\sum_i |\vec{p}_i|^2} \tag{3.2}$$

where $\alpha$, $\beta$ mean x,y,z direction. The eigenvalues of the sphericity tensor are $\lambda_1$, $\lambda_2$, and $\lambda_3(\lambda_1 > \lambda_2 > \lambda_3)$. The sphericity (S) and aplanarity (A) are given as

$$\begin{aligned} S &= \frac{3}{2}(\lambda_2 + \lambda_3) = \frac{3}{2}(1 - \lambda_1) \\ A &= \frac{3}{2}\lambda_3 \end{aligned} \tag{3.3}$$

For spherical distribution of $B\bar{B}$ event, the eigenvalues should be closed to $\frac{1}{3}$ due to the isotropic distribution which makes S and A are close to 1 and $\frac{1}{2}$. For the continuum background, $\lambda_3$ is about 1 due to the angular distribution, so the S and A are closed to 0. In our training, we only take S as our training variable.


doi:doi:10.6342/NTU202203205

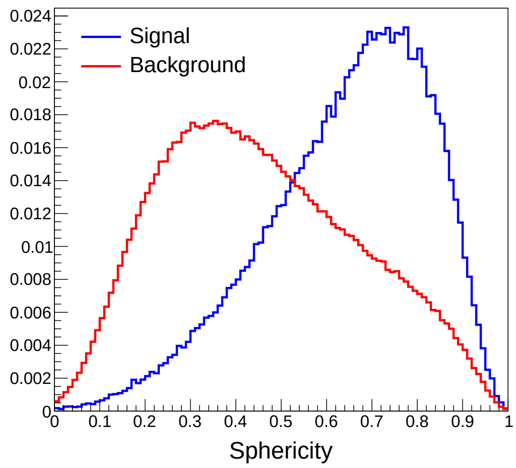


Figure 3.7: The normalized distribution of sphericity for signal and background

### 3.2.6 $q \cdot r$

We also use flavor tagging quality $q \cdot r$ which is shown in Fig 3.8 to judge how likely a B candidate is B meson. The value of the preferred flavor q, equals +1 for particle $B^0$ or $B^+$, and -1 for anti-particle $\bar{B}^0$ or $B^-$. The value of tagging quality r varies between 0 to +1 .$q \cdot r$ is given as

$$q \cdot r = \frac{N(B^0) - N(\bar{B}^0)}{N(B^0) + N(\bar{B}^0)} \tag{3.4}$$

where $N(B^0)$ and $N(\bar{B}^0)$ are the numbers of $B^0$ and $\bar{B}^0$. The value of $q \cdot r$ of background events is closed to 0 since they are not correctly reconstructed, and correctly reconstructed B candidates is distributed between 0 to $\pm 1$.


doi:doi:10.6342/NTU202203205

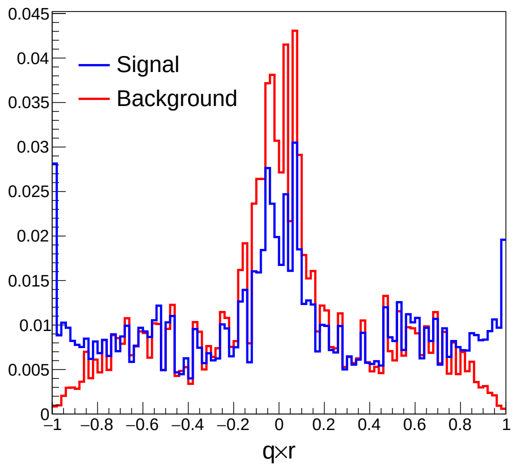


Figure 3.8: The normalized distribution of $q \cdot r$ for signal and background

### 3.2.7 Fox-Wolfram moments

Fox-Wolfram moment[10] $H_l$ is defined as

$$H_l = \sum_{i,j}^{N} |p_i||p_j| P_l(cos\theta_{i,j}) \tag{3.5}$$

where $P_l$ is l-th Legendre polynomial, $\theta_{i,j}$ is the opening angle between the i-th and j-th particle, $p_i$ and $p_j$ is the i-th and j-th final state particle. In our analysis, we use normalized Fox-Wolfram moment instead of $H_l$, normalized Fox-Wolfram moment is defined as

$$R_l = \frac{H_l}{H_0} \tag{3.6}$$

In Fox-Wolfram moment, we only use $R_2$ as training variable.

### 3.2.8 Kakuno Super Fox-Wolfram (KSFW)

KSFW variables are useful to separate signal from continuum $q\bar{q}$ events, which includes 6 normalized Fox-Wolfram moments. The distributions are not same in different missing mass region. Missing mass is given as

$$MM^2 = (E_{\Upsilon(4s)} - \sum_{i=1}^{N_t} E_i)^2 - \sum_{i=1}^{N_t} |p_i|^2 \tag{3.7}$$



doi:doi:10.6342/NTU202203205

where separated into 7 region as Table 3.1.

| Region | 1 | 2 | 3 | 4 | 5 | 6 | 7 |
|---|---|---|---|---|---|---|---|
| $MM^2(GeV^2/c^4)$ | $< -0.5$ | $-0.5 \sim 0.3$ | $0.3 \sim 1.0$ | $1.0 \sim 2.0$ | $2.0 \sim 3.5$ | $3.5 \sim 6.0$ | $> 6.0$ |

Table 3.1: The $MM^2$ regions

KSFW is defined as :

$$KSFW = \sum_{l=0}^{4} R_l^{so} + \sum_{l=0}^{4} R_l^{oo} + \gamma \sum_{n=1}^{N_t} |P_{t,n}| \tag{3.8}$$

where the superscript s denotes the hadronic particle from reconstructed B candidate, and o denotes which from rest of event. $P_t$ is the transverse momenta of all particles, $N_t$ is the number of tracks in an event, $\gamma$ is fisher coefficient. $R_l^{oo}$ is defined as :

$$R_l^{oo} \equiv \frac{\alpha_l^c H_l^{so,c} + \alpha_l^n H_l^{so,n} + \alpha_l^m H_l^{so,m}}{E_{beam} - \Delta E} \tag{3.9}$$

where c, n and m stand for charged, neutral and missing.

For $l = 1,3$

$$H_l^{oo} \equiv \beta_l^{oo} \sum_i \sum_j Q_i Q_j |p_i| P_l(cos\theta_{ij}) \tag{3.10}$$

and $H_l^{so,(n,m)} = 0$.

For $l = 0,2,4$

$$H_l^{oo,(c,n,m)} \equiv \beta_l^{oo} \sum_i \sum_j |p_i| P_l(cos\theta_{ij}) \tag{3.11}$$

and

$$H_l^{so,(c,n,m)} \equiv \beta_l^{so} \sum_i \sum_j |p_i| P_l(cos\theta_{ij}) \tag{3.12}$$

where $i$ denotes the particle from B candidate, j iterates over the same category (charged, neutral, missing)tracks of others;$Q_i, Q_j$ are the electric charges of particle $i$ and particle $i$ respectively; $P_l$ is legendre polynomial; $\theta_{ij}$ is angle between particle $i$ and particle $j$; $\alpha$ and $\beta$ are fisher coefficient.

$R_l^{oo}$ is defined as

For $l = 1,3$

$$R_l^{oo} = \frac{\beta_l^{oo} \sum_j \sum_{j \neq k} Q_j Q_k |p_j||p_k| P_l(cos\theta_{jk})}{(E_{beam} - \Delta E)^2} \tag{3.13}$$



doi:doi:10.6342/NTU202203205

For $l = 0,2,4$

$$R_l^{oo} = \frac{\beta_l^{oo} \sum_j \sum_{j \neq k} |p_j||p_k| P_l(cos\theta_{jk})}{(E_{beam} - \Delta E)^2} \tag{3.14}$$

$R_l^{so}$ is defined as

$$R_l^{so} = \frac{\alpha_l^c H_l^{so,c} + \alpha_l^n H_l^{so,n} + \alpha_l^m H_l^{so,m}}{E_{beam} - \Delta E} \tag{3.15}$$

where $\alpha$,$\beta$ are fisher coefficient, and $E_{beam}$ is beam energy.

### 3.2.9 Other training variables

Except for the variables we mentioned before, we also put the missing energy $E_{miss}$ and missing mass squared into training. In summary, we put 28 variables into NeuroBayes training which are shown in Table 3.2.

| | |
|---|---|
| $E_{miss}$ | $H_l^{so,c}, l = 0,1,2,3,4$ |
| $R_2$ $E_T$ | $H_l^{so,n}, l = 0,2,4$ |
| Thrust angle of $cos\theta_{th}$ | $H_l^{so,m}, l = 2,4$ |
| $B^0$ polar angle of $cos\theta_B$ | $H_l^{oo}, l = 3,4$ |
| Sphericity $S$ | $R_l^{oo}, l = 1,2,3$ |
| $\Delta Z$ | $R_l^{so}, l = 2,3,4$ |
| Missing mass squared $MM^2$ | $R_l^{gso}.l = 1,2$ |
| $q \cdot r$ | |

Table 3.2: Summary of training variables



doi:doi:10.6342/NTU202203205

## 3.3 Best FOM

After NeuroBayes training and testing, we have to decide the best background suppression cuts for our NeuroBayes output. Therefore, we apply Figure of Merit (FOM) to estimate performance of corresponding `CSMVA` output. FOM is defined as

$$FOM = \frac{N_{sig}}{\sqrt{N_{sig} + N_{bkg}}} \tag{3.16}$$

where $N_{sig}$ is numbers of signal and $N_{bkg}$ is numbers background which have been normalized to sideband data, and this optimization was performed in the signal region. To estimate $N_{sig}$, we use half upper limit of branching fraction $1.9 \times 10^{-6}$ in previous measurement. In order to show the performance of background rejection of both types signals, we also draw the ROC(Receiver operator characteristic) curve which is shown in Figure 3.9.

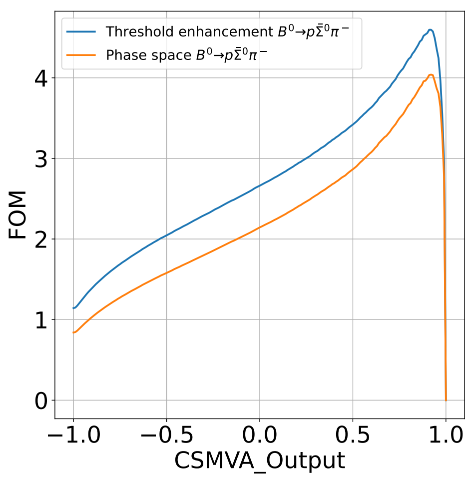


(a)

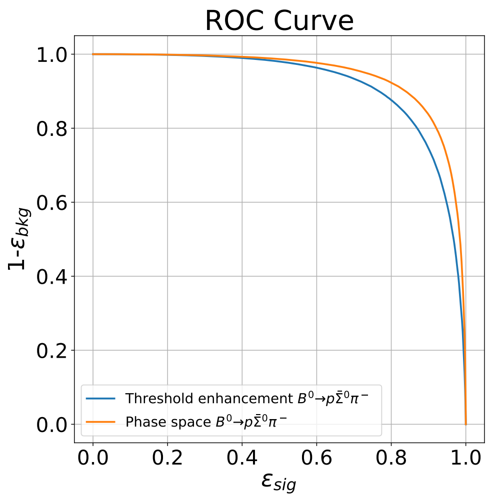


(b)

Figure 3.9: (a) Figure of Merit plot (b) ROC

To eliminate most continuum background and keep enough signal efficiency, we choose `CSMVA` output at 0.8 as best FOM cut which can cut off about 99% continuum background events and leave 45% signal efficiency.


doi:doi:10.6342/NTU202203205

## 3.4 Peaking Background Veto

### 3.4.1 Generic $B\bar{B}$

In generic $B\bar{B}$ background event, we discover that there is peaking background in our signal region, and pined down those event mostly come from $B^0 \to p\Lambda_c^-$ decay after our investigation, so we introduce $\Lambda_c^+$ veto method to kill those events. Because $\Lambda_c^+ \to \Lambda\pi^+$ and $\Lambda_c^+ \to \Sigma\pi^+$, we reconstruct the invariant mass $M_{\Lambda\pi}$ which is shown in Fig 3.10 as veto variable.

Fig 3.11 shows the result of $M_{\Lambda\pi}$ fitting, the red line is $B \to p\Lambda_c^-(\Lambda_c^- \to \bar{\Lambda}\pi^-)$, so the peaking position is exact $\Lambda_c$ mass value. The brown line part is contributed by $B \to p\Lambda_c^-(\Lambda_c^- \to \bar{\Sigma}^0\pi^-)$, because we only capture $\Lambda$ and $\pi$ which make the peaking position shifted. In order to remove the peak and keep enough efficiency, we decide to cut off the region of $M_{\Lambda\pi}$ at 2.15 $\mathrm{GeV/c^2} < \mathrm{M}_{\Lambda\pi} < 2.3\mathrm{GeV/c^2}$ about $\pm 2\sigma$ of brown line gaussian in $\Lambda_c$ mass region. The performance of veto is shown in Fig 3.12.

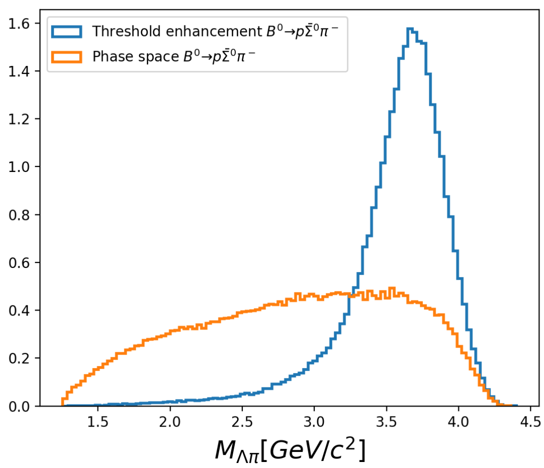


Figure 3.10: $M_{\bar{\Lambda}\pi^-}$ normalized distribution for $B^0 \to p\bar{\Sigma}\pi^-$


doi:doi:10.6342/NTU202203205

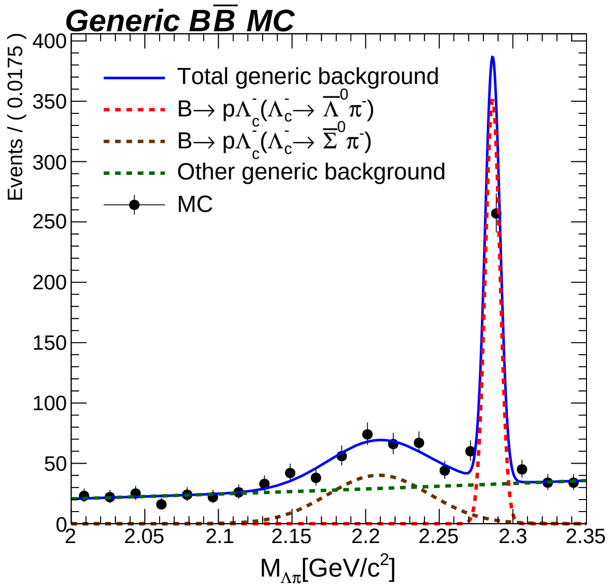


Figure 3.11: Fitting result of $M_{\Lambda\pi}$ in generic background sample to decide veto region.

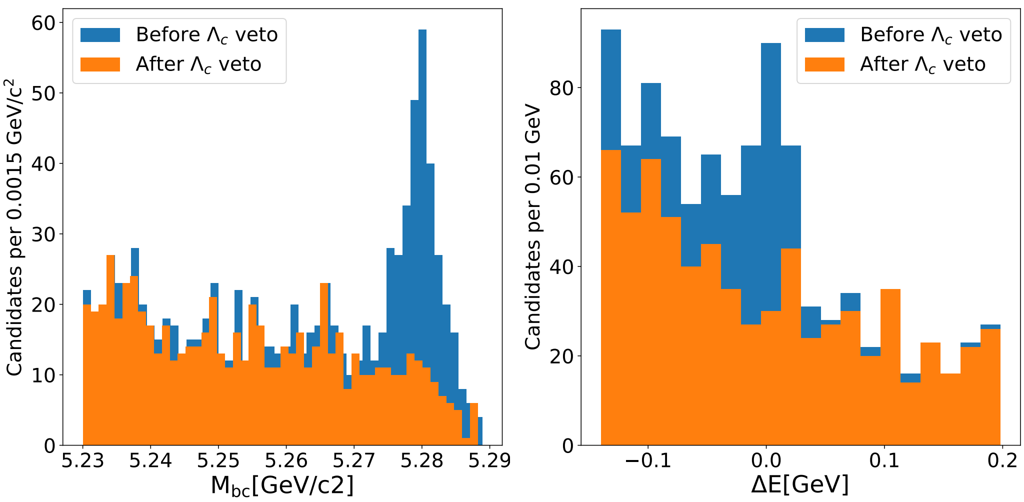


(a) (b)

Figure 3.12: The performance of $\Lambda_c^+$ veto in generic $B\bar{B}$ background (a)$M_{bc}$ (b)$\Delta E$


doi:doi:10.6342/NTU202203205

### 3.4.2 Rare B Decay

In $b \to s$ rare decay events, we also discovered peaking background which listed in Table 3.3 in our signal region. In order to check the effect of those decay channels, we cut off the region in $M_{p\bar{\Lambda}}$ greater than 4.95 GeV/c$^2$ and the region in $M_{p\pi}$ smaller than 1.121 GeV/c$^2$, the result is shown in Fig 3.14. After our study of rare decay, we found those channels are in the specific region but their yields are overrated by decay table. So we won't apply the veto in the real data.

| Decay channel | $\mathscr{B}(10^{-6})$ in decay table | $\mathscr{B}(10^{-6})$ in PDG |
|---|---|---|
| $B^+ \to p\bar{\Lambda}$ | 0.37 | $0.24^{+0.1}_{-0.08} \pm 0.03$ |
| $B^+ \to p\bar{\Sigma}^0$ | 1.5 | - |
| $B^+ \to p\bar{\Lambda}\rho^0$ | 5.7 | $4.78^{+0.67}_{-0.64} \pm 0.6$ |
| $B^+ \to \Lambda\bar{\Lambda}\pi^+$ | 2.8 | $< 0.9$ |
| $B^0 \to \Lambda\bar{\Lambda}$ | 0.3 | $< 0.3$ |
| $B^0 \to \Lambda\bar{\Sigma}^0$ | 1.0 | - |
| $B^0 \to \Sigma^0\bar{\Sigma}^0$ | 1.0 | - |

Table 3.3: Main rare decay background list

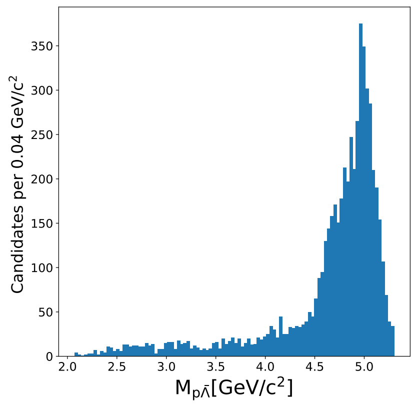


(a)

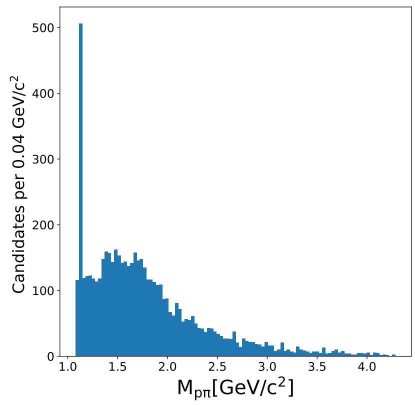


(b)

Figure 3.13: (a) $M_{p\Lambda}$ and (b) $M_{p\pi}$ distribution of rare decay background


doi:doi:10.6342/NTU202203205

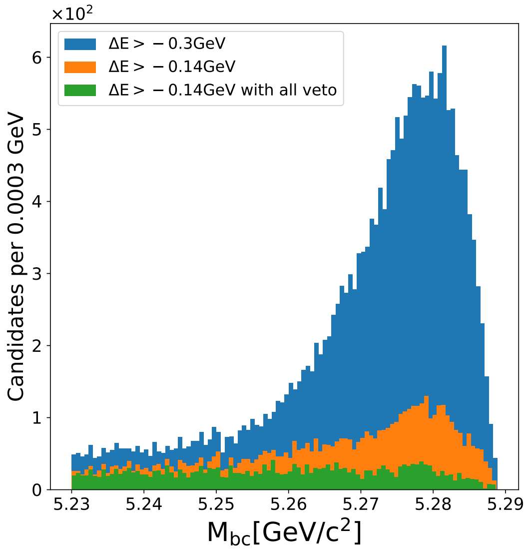


Figure 3.14: Performance of rare decay veto

## 3.5 Best Candidate Selection

To remove multiple candidate event, we reconstruct $\Lambda$ vertex first then use $p$,$\pi$ tracks and $\Lambda$ vertex to get $B$ vertex and choose the minimum $B$ vertex $\chi^2$ obtained by ExKfitter for each event as best candidate selection criteria. Fig 3.15 shows the performance of best candidate selection, there are about 1.18% multiple candidate events before best candidate selection. The distribution of $M_{bc}$ and $\Delta E$ after the all selection are shown in Fig 3.16.

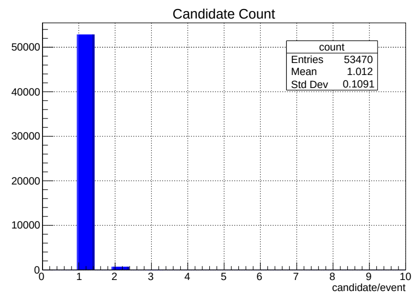


(a)

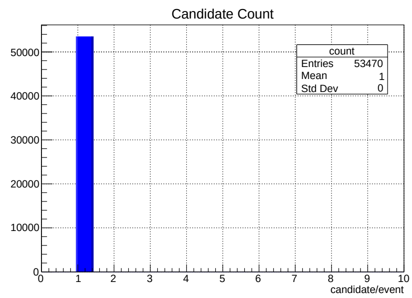


(b)

Figure 3.15: Best candidate performance for TE $B^0 \to p\bar{\Sigma}^0\pi^-$(a) Before best candidate selection (b)After best candidate selection



doi:doi:10.6342/NTU202203205

## 3.6 Conclusion of Background Study

After all selection cut to kill any possible background, we make the predicted plot of data distribution with all kind of Monte Carlo sample according to same luminosity which are shown in Fig 3.16 and compare the $M_{bc}$ and $\Delta E$ distribution between sideband data and Monte Carlo sample whose results are shown is Fig 3.17. In summary, there is no significant difference in distribution, but the background yield is larger than our expectation, and we show the details of each cut in section 3.7.

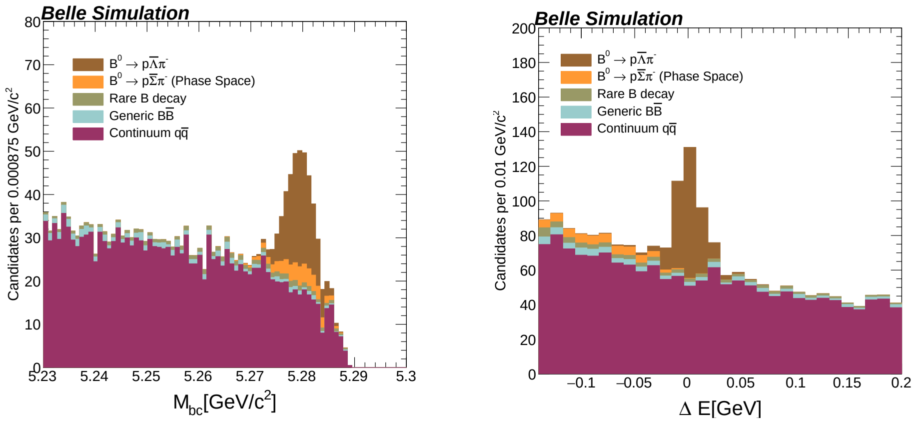


(a) (b)

Figure 3.16: $M_{bc}$ and $\Delta E$ distribution after all selection (a)$M_{bc}$, (b)$\Delta E$

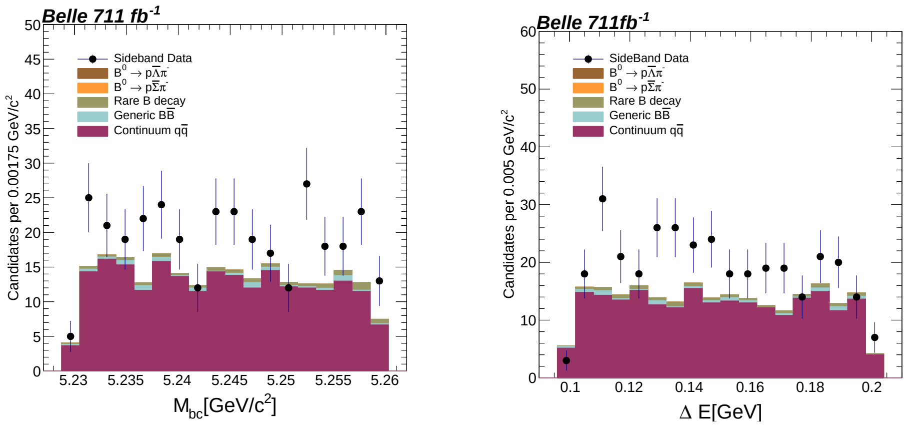


(a) (b)

Figure 3.17: Comparison between sideband data and MC for $M_{bc}$ and $\Delta E$ distribution after all selection cut


doi:doi:10.6342/NTU202203205

## 3.7 Table of selection counting

**Before Continuum Suppression**

| Type | Whole Region | $B^0 \to p\bar{\Sigma}^0\pi^-$ Signal Region | $B^0 \to p\bar{\Lambda}\pi^-$ Signal Region |
|---|---|---|---|
| efficiency of $B^0 \to p\bar{\Sigma}^0\pi^-$ (PHSP) | 11.66% | 11.51% | - |
| Expected yields for $B^0 \to p\bar{\Sigma}^0\pi^-$ (PHSP) | 171 | 169 | - |
| Self-crossfeed for $B^0 \to p\bar{\Sigma}^0\pi^-$(PHSP) | 8.69% | 3.77% | - |
| efficiency of $B^0 \to p\bar{\Sigma}^0\pi^-$ (TE) | 15.79% | 15.67% | - |
| Expected yields for $B^0 \to p\bar{\Sigma}^0\pi^-$ (TE) | 232 | 230 | - |
| Self-crossfeed for $B^0 \to p\bar{\Sigma}^0\pi^-$(TE) | 2.41% | 1.9% | - |
| efficiency of $B^0 \to p\bar{\Lambda}\pi^-$ | 22.67% | - | 21.99% |
| Expected yields for $B^0 \to p\bar{\Lambda}\pi^-$ | 549 | - | 532 |
| Self-crossfeed for $B^0 \to p\bar{\Lambda}\pi^-$ | 2.70% | - | 1.37% |
| Generic $B\bar{B}$ | 354 | 93 | 25 |
| Continuum $q\bar{q}$ | 137559 | 27600 | 5357 |
| Rare decay | 381 | 130 | 35 |

**After Continuum Suppression**

| Type | Whole Region | $B^0 \to p\bar{\Sigma}^0\pi^-$ Signal Region | $B^0 \to p\bar{\Lambda}\pi^-$ Signal Region |
|---|---|---|---|
| Efficiency of $B^0 \to p\bar{\Sigma}^0\pi^-$ (PHSP) | 6.08% | 6.01% | - |
| Expected yields for $B^0 \to p\bar{\Sigma}^0\pi^-$ (PHSP) | 89 | 88 | - |
| Self-crossfeed for $B^0 \to p\bar{\Sigma}^0\pi^-$ (PHSP) | 5.31% | 2.57% | - |
| Efficiency of $B^0 \to p\bar{\Sigma}^0\pi^-$ (TE) | 7.08% | 7.03% | - |
| Expected Yield for $B^0 \to p\bar{\Sigma}^0\pi^-$ (TE) | 104 | 103 | - |
| Self-crossfeed for $B^0 \to p\bar{\Sigma}^0\pi^-$ (TE) | 1.92% | 1.65% | - |
| Efficiency of $B^0 \to p\bar{\Lambda}\pi^-$ | 10.25% | - | 9.98% |
| Expected yields for $B^0 \to p\bar{\Lambda}\pi^-$ | 248 | - | 241 |
| Self-crossfeed for $B^0 \to p\bar{\Lambda}\pi^-$ | 2.11% | - | 1.25% |
| Generic $B\bar{B}$ | 100 | 33 | 19 |
| Continuum $q\bar{q}$ | 2167 | 430 | 180 |
| Rare decay | 90 | 35 | 8 |


doi:doi:10.6342/NTU202203205

**After Peaking Background Veto**

| Type | Whole Region | $B^0 \to p\bar{\Sigma}^0\pi^-$ Signal Region | $B^0 \to p\bar{\Lambda}\pi^-$ Signal Region |
|---|---|---|---|
| Efficiency of $B^0 \to p\bar{\Sigma}^0\pi^-$ (PHSP) | 5.76% | 5.70% | - |
| Expected Yield for $B^0 \to p\bar{\Sigma}^0\pi^-$ (PHSP) | 84 | 83 | - |
| Self-crossfeed for $B^0 \to p\bar{\Sigma}^0\pi^-$ (PHSP) | 5.12% | 2.53% | |
| Efficiency of $B^0 \to p\bar{\Sigma}^0\pi^-$ (TE) | 7.05% | 7.00% | - |
| Expected Yield for $B^0 \to p\bar{\Sigma}^0\pi^-$ (TE) | 103 | 102 | - |
| Self-crossfeed for $B^0 \to p\bar{\Sigma}^0\pi^-$ (TE) | 1.91% | 1.65% | |
| Efficiency of $B^0 \to p\bar{\Lambda}\pi^-$ | 10.20% | - | 9.93% |
| Expected Yield for $B^0 \to p\bar{\Lambda}\pi^-$ | 247 | - | 241 |
| Self-crossfeed for $B^0 \to p\bar{\Lambda}\pi^-$ | 2.08% | - | 1.24% |
| Generic $B\bar{B}$ | 69 | 14 | 3 |
| Continuum $q\bar{q}$ | 2092 | 416 | 175 |
| Rare decay | 82 | 33 | 8 |

**After Best Candidate Selection**

| Type | Whole Region | $B^0 \to p\bar{\Sigma}^0\pi^-$ Signal Region | $B^0 \to p\bar{\Lambda}\pi^-$ Signal Region |
|---|---|---|---|
| Efficiency of $B^0 \to p\bar{\Sigma}^0\pi^-$ (PHSP) | 5.65% | 5.56% | - |
| Expected yields for $B^0 \to p\bar{\Sigma}^0\pi^-$ (PHSP) | 83 | 82 | - |
| Self-crossfeed for $B^0 \to p\bar{\Sigma}^0\pi^-$ (PHSP) | 3.63% | 1.97% | - |
| Efficiency of $B^0 \to p\bar{\Sigma}^0\pi^-$ (TE) | 7.00% | 6.92% | - |
| Expected yields for $B^0 \to p\bar{\Sigma}^0\pi^-$ (TE) | 102 | 101 | - |
| Self-crossfeed for $B^0 \to p\bar{\Sigma}^0\pi^-$ (TE) | 1.40% | 1.29% | - |
| Efficiency of $B^0 \to p\bar{\Lambda}\pi^-$ | 10.06% | - | 9.80% |
| Expected yields for $B^0 \to p\bar{\Lambda}\pi^-$ | 256 | - | 237 |
| Self-crossfeed for $B^0 \to p\bar{\Lambda}\pi^-$ | 1.81% | - | 1.14% |
| Generic $B\bar{B}$ | 63 | 14 | 3 |
| Continuum $q\bar{q}$ | 1828 | 416 | 151 |
| Rare decay | 76 | 32 | 7 |



doi:doi:10.6342/NTU202203205

# Chapter 4

# Yield Extraction

## 4.1 Introduction

In the analysis, we use unbinned maximum extend likelihood (UML) fit method to extract the signal yields. The likelihood function which is made of 2 dimension($\Delta E$,$M_{bc}$) is given as

$$\mathscr{L} = \frac{e^{-(N_s+N_b)}}{N!}\prod_{i=1}^{N}(N_sP_s(M_{bc},\Delta E)+N_bP_b(M_{bc},\Delta E)) \tag{4.1}$$

where N is number of events in our fit, $i$ denotes the $i^{th}$ event, and $P_j$ is probability density functions (PDF) of signal and, background. At first, we will introduce the PDF for each component, then the result of fitter test.

## 4.2 Correlation Check

In order to decide the PDF, we check the correlation factor of each component.The 2D distributions of each component are shown in Fig 4.1 and Fig 4.2. In $B^0 \to p\bar{\Sigma}^0\pi^-$ channel, because of the low correlation between $M_{bc}$ and $\Delta E$, we use 1D×1D histogram PDF to model our signal whether it's following threshold enhancement or phase space. In summary, all component correlation numbers are listed in Table 4.1.


doi:doi:10.6342/NTU202203205

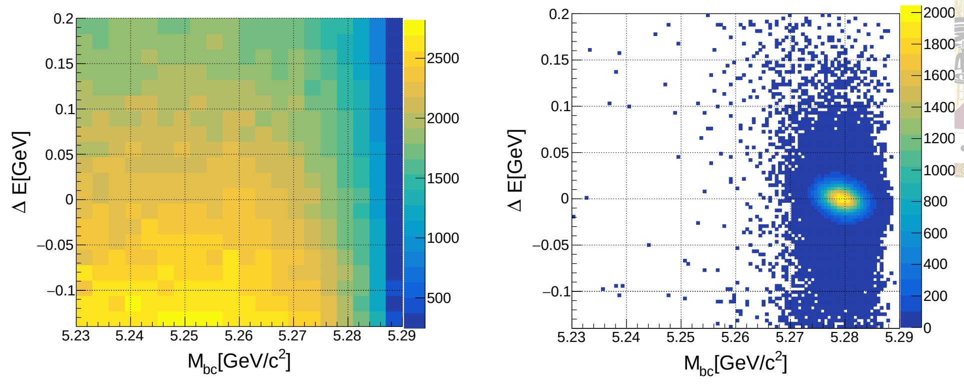


(a) (b)

Figure 4.1: ΔE vs $M_{bc}$ for (a) background and (b) $B^0 \to p\bar{\Lambda}\pi^-$

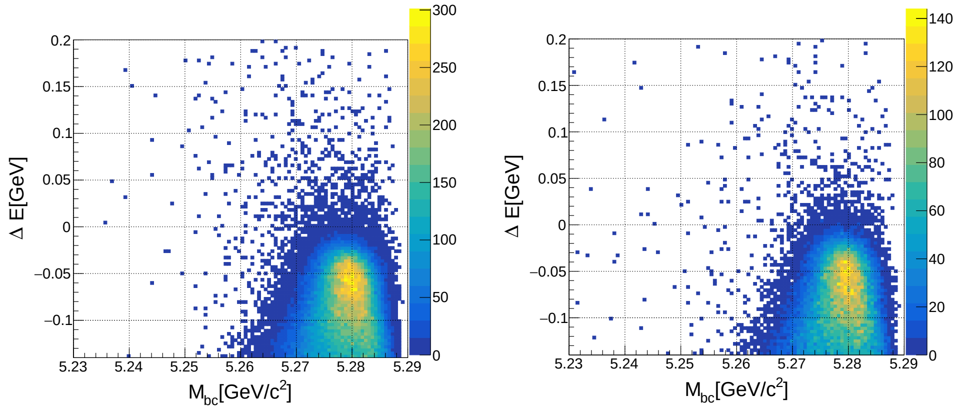


(a) (b)

Figure 4.2: ΔE vs $M_{bc}$ for $B^0 \to p\bar{\Sigma}^0\pi^-$ for (a)Threshold enhancement and (b) phase space

| Type | Correlation |
|---|---|
| PHSP $B^0 \to p\bar{\Sigma}^0\pi^-$ Signal | 0.035 |
| TE $B^0 \to p\bar{\Sigma}^0\pi^-$ Signal | 0.024 |
| $B^0 \to p\bar{\Lambda}\pi^-$ | -0.006 |
| continuum $q\bar{q}$ | 0.005 |
| Generic $B\bar{B}$ | 0.043 |

Table 4.1: Summary of correlation


doi:doi:10.6342/NTU202203205

## 4.3 PDF Modeling

Our 2D fitter can be divided into those components:$B^0 \to p\bar{\Sigma}^0\pi^-$, $B^0 \to p\bar{\Lambda}\pi^-$, rare decay excluded our signal, and background which is combined with continuum $q\bar{q}$ and generic $B\bar{B}$ whose distribution is similar to continuum event. The proportion of self-cross feed is about 2% which is extremely lower than our statistic error, so we just ignore it in our fitter. All PDF which we choose for each component are listed in Table 4.2. Table 4.3 shows all the floated fitting parameters for PDFs. The fitting result of signal and other background are shown as Fig 4.3 to Fig 4.7 , then Fig 4.8 shows the fitting result of one psudoexperiment.

| | $M_{bc}$ | $\Delta E$ |
|---|---|---|
| $B^0 \to p\bar{\Sigma}^0\pi^-$ | 1D HistPDF | 1D HistPDF |
| $B^0 \to p\bar{\Lambda}\pi^-$ | Double Gaussian with same mean and different width | Triple Gaussian with same mean and different width |
| Self-crossfeed of $B^0 \to p\bar{\Lambda}\pi^-$ | 2D Kernel PDF | |
| Continuum $q\bar{q}$ + Generic $B\bar{B}$ + Rare B decay | ARGUS Function | 2nd order Polynomial |

Table 4.2: Summary of PDF

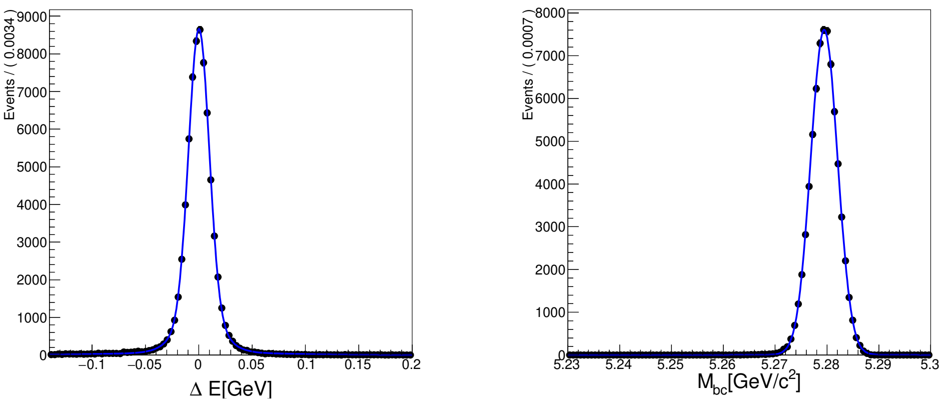


Figure 4.3: $\Delta E$ , $M_{bc}$ for $B^0 \to p\bar{\Lambda}\pi^-$


doi:doi:10.6342/NTU202203205

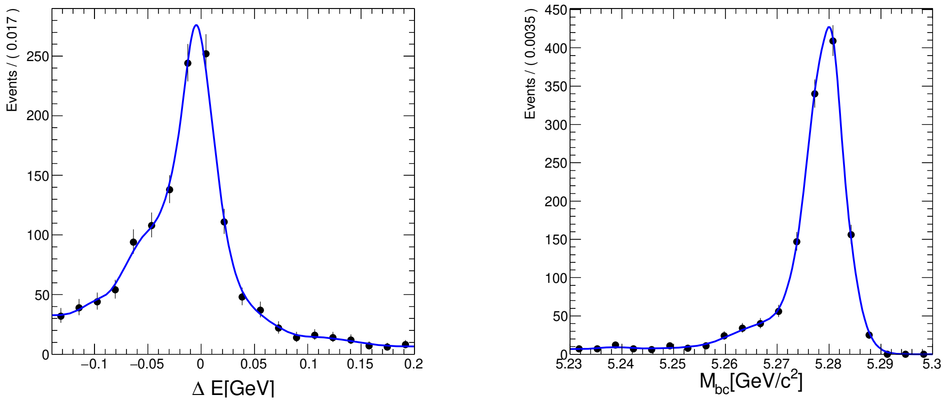


Figure 4.4: $\Delta E$ , $M_{bc}$ for self-crossfeed of $B^0 \to p\bar{\Lambda}\pi^-$

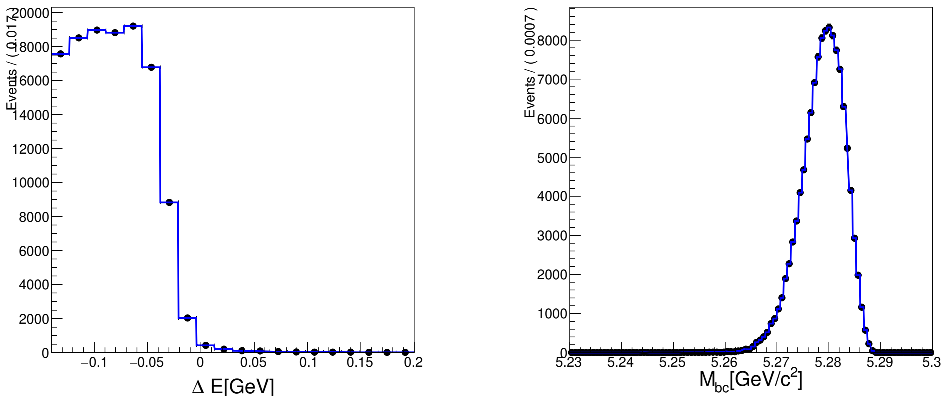


Figure 4.5: $\Delta E$ , $M_{bc}$ for threshold enhancement $B^0 \to p\bar{\Sigma}^0\pi^-$

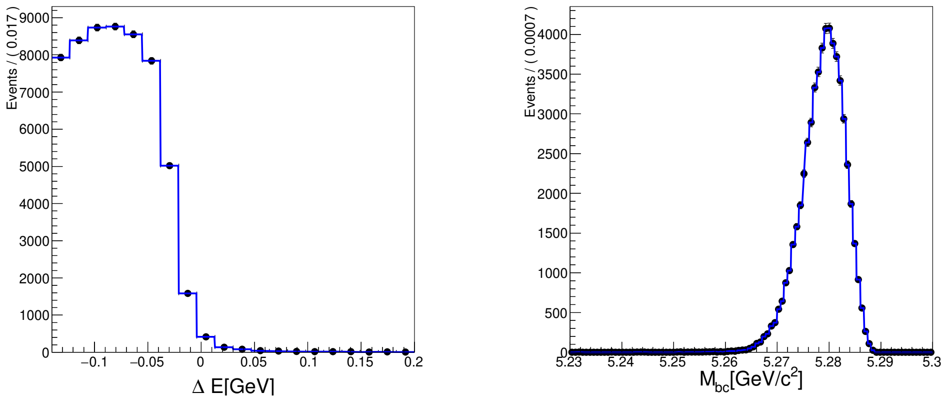


Figure 4.6: $\Delta E$ , $M_{bc}$ for phase space $B^0 \to p\bar{\Sigma}^0\pi^-$


doi:doi:10.6342/NTU202203205

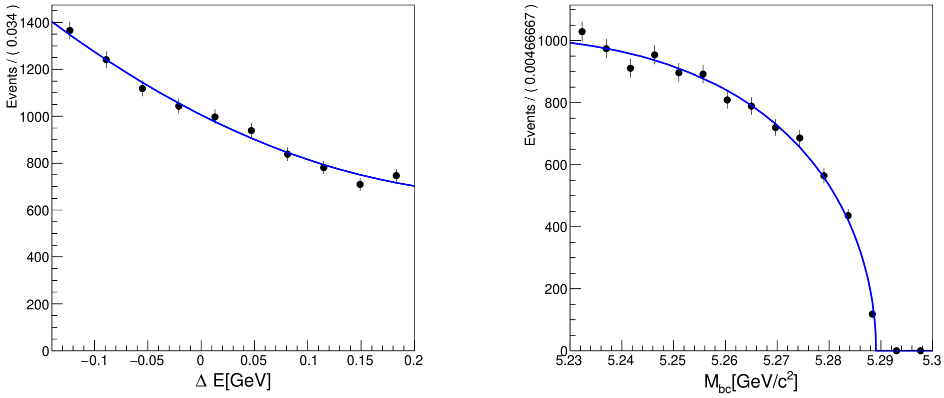


Figure 4.7: $\Delta E$ , $M_{bc}$ for background

| Component | Fitting Parameter |
|---|---|
| $B^0 \to p\bar{\Sigma}^0\pi^-$ | $N_{B^0\to p\bar{\Sigma}^0\pi^-}$ is floated |
| $B^0 \to p\bar{\Lambda}\pi^-$ | $N_{B^0\to p\bar{\Lambda}\pi^-}$ is floated |
| Self-crossfeed of $B^0 \to p\bar{\Lambda}^0\pi^-$ | $N_{scf}$ = ratio$\times N_{B^0\to p\bar{\Lambda}\pi^-}$, ratio is fixed |
| Continuum $q\bar{q}$+Generic $B\bar{B}$+Rare B decay | $N_{bkg}$ and ARGUS shape parameter are floated |

Table 4.3: Fitting parameter

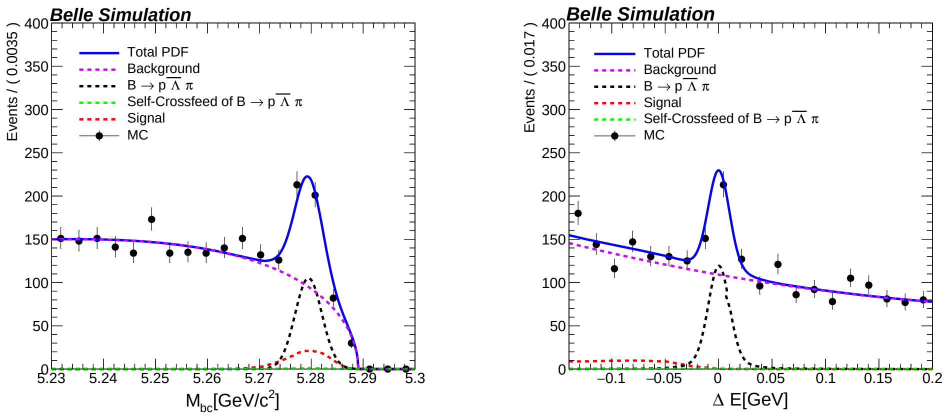


(a) (b)

Figure 4.8: Fitting plots of one pseudo-experiment (a) $M_{bc}$ and (b) $\Delta E$


doi:doi:10.6342/NTU202203205

| Fitting parameter | Fitting result | Expected result |
|---|---|---|
| $N_{B^0\to p\bar{\Sigma}^0\pi}$ | $58.18^{+18.28}_{-17.52}$ | 65 |
| $N_{bkg}$ | $2203.84^{+50.56}_{-49.74}$ | 2203 |
| $N_{B^0\to p\bar{\Lambda}\pi}$ | $192.33^{+16.40}_{-15.67}$ | 190 |
| ARGUS shape variable | $-22.37^{+4.16}_{-4.14}$ | -26.07 |

Table 4.4: Fitting result of PDF parameters

## 4.4 Fitter Test

In order to see the performance of our fitter, we perform the fitter test to check whether there is any bias in our fitting model. The fitter test includes Gsim ensemble test and toyMC ensemble test with two generated ways, the gsim sample is extracted from randomly selecting MC as input, and the toyMC sample is generated with PDFs. We determine the input number with Poisson distribution with mean value equal to the expected number of signal and background in full Belle luminosity. The mean value of input number of $B^0 \to p\bar{\Sigma}^0\pi^-$ is varied from 35 to 95, the mean value of input number of $B^0 \to p\bar{\Lambda}\pi^-$ is fixed at 190, and $N_{bkg}$ is obtained from the background MC. Then the fitting result information is collected repeatedly 5000 times to check the pull distribution whether it is a standard Gaussian ($\bar{x} = 0$, $\sigma = 1$ ), the definition of pull is given as

$$Pull = \frac{Yield - Expect\ yield}{\sigma_{fit}} \tag{4.2}$$

where $\sigma_{fit}$ is statistical uncertainty. Except gsim and toyMC fitter test, we also perform linearity test for the yield of $B^0 \to p\bar{\Sigma}^0\pi^-$ to confirm our fitting yield is linear with different $N_{sig}$.

### 4.4.1 ToyMC ensemble test

Our results of toyMC ensemble test are shown in Fig 4.9 and Table 4.5, Table 4.6. Overall, $Pull_{mean}$, $Pull_{width}$ and $N_{sig}$ all cover the expect value within $1 \sim 3\sigma$ for both channel. Table 4.5 and Table 4.6 show the detailed information of ToyMC ensemble test for $B^0 \to p\bar{\Lambda}\pi^-$ and $B^0 \to p\bar{\Sigma}^0\pi^-$. The performance of linearity test for toyMC sample



doi:doi:10.6342/NTU202203205

is shown in Fig 4.10 which shows the slope and intercept cover the value within $1 \sim 3\sigma$. Each pull, yield, and error fitting result is shown in Appendix B.

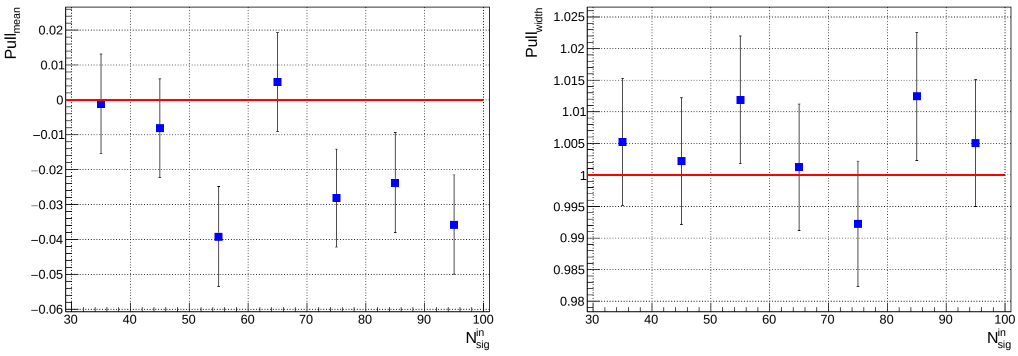


(a) (b)

Figure 4.9: Pull mean and pull width plot of toyMC ensemble test for each input signal number

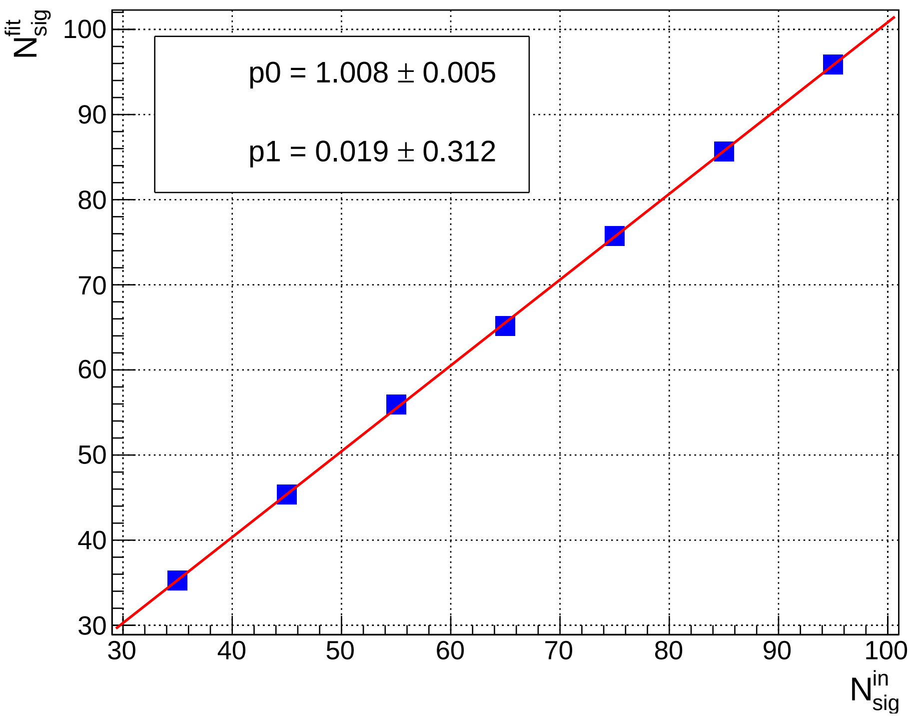


Figure 4.10: ToyMC linearity test. The p0 is slope and the p1 is intercept of 1st order polynomial.



doi:doi:10.6342/NTU202203205

| $N_{input}^{B^0\to p\bar{\Sigma}^0\pi^-}$ | $N_{fit}^{B^0\to p\bar{\Sigma}^0\pi^-}$ | $Pull_{mean}^{B^0\to p\bar{\Sigma}^0\pi^-}$ | $Pull_{width}^{B^0\to p\bar{\Sigma}^0\pi^-}$ | $error_{mean}^{B^0\to p\bar{\Sigma}^0\pi^-}$ |
|---|---|---|---|---|
| 95 | $95.89\pm0.27$ | $-0.036\pm0,014$ | $1.005\pm0.010$ | $18.68\pm0.01$ |
| 85 | $85.65\pm0.26$ | $-0.024\pm0.014$ | $1.012\pm0.010$ | $18.33\pm0.01$ |
| 75 | $75.72\pm0.25$ | $-0.028\pm0.014$ | $0.992\pm0.010$ | $17.99\pm0.01$ |
| 65 | $65.15\pm0.25$ | $0.005\pm0.014$ | $1.001\pm0.010$ | $17.61\pm0.01$ |
| 55 | $55.91\pm0.25$ | $-0.039\pm0.014$ | $1.012\pm0.010$ | $17.26\pm0.01$ |
| 45 | $45.36\pm0.24$ | $-0.008\pm0.014$ | $1.002\pm0.010$ | $16.87\pm0.01$ |
| 35 | $35.25\pm0.23$ | $-0.001\pm0.014$ | $1.005\pm0.010$ | $16.47\pm0.01$ |

Table 4.5: Detailed result of toyMC ensemble test for $B^0 \to p\bar{\Sigma}^0\pi^-$

| $N_{input}^{B^0\to p\bar{\Sigma}^0\pi^-}$ | $N_{fit}^{B^0\to p\bar{\Lambda}\pi^-}$ | $Pull_{mean}^{B^0\to p\bar{\Lambda}\pi^-}$ | $Pull_{width}^{B^0\to p\bar{\Lambda}\pi^-}$ | $error_{mean}^{B^0\to p\bar{\Lambda}\pi^-}$ |
|---|---|---|---|---|
| 95 | $189.92\pm0.23$ | $0.022\pm0.014$ | $0.987\pm0.010$ | $16.29\pm0.01$ |
| 85 | $189.86\pm0.23$ | $0.026\pm0.014$ | $0.995\pm0.010$ | $16.28\pm0.01$ |
| 75 | $189.76\pm0.22$ | $0.031\pm0.014$ | $0.980\pm0.010$ | $16.27\pm0.01$ |
| 65 | $190.29\pm0.23$ | $-0.001\pm0.014$ | $0.981\pm0.010$ | $16.27\pm0.01$ |
| 55 | $190.26\pm0.22$ | $0.001\pm0.014$ | $0.979\pm0.010$ | $16.26\pm0.01$ |
| 45 | $190.24\pm0.22$ | $0.001\pm0.014$ | $0.960\pm0.010$ | $16.25\pm0.01$ |
| 35 | $190.82\pm0.23$ | $-0.034\pm0.014$ | $0.980\pm0.010$ | $16.25\pm0.01$ |

Table 4.6: Detailed result of toyMC ensemble test for $B^0 \to p\bar{\Lambda}\pi^-$

### 4.4.2 Gsim ensemble test

Our results of Gsim ensemble test are shown in Fig 4.11 and Table 4.7, Table 4.8. Overall, $Pull_{mean}$, $Pull_{width}$ and $N_{sig}$ all cover the expect value within $1 \sim 3\sigma$ for both channel. Table 4.7 and Table 4.8 show the detailed information of Gsim ensemble test for $B^0 \to p\bar{\Lambda}\pi^-$ and $B^0 \to p\bar{\Sigma}^0\pi^-$. The performance of linearity test for gsim sample sample is shown in Fig 4.12. which shows the slope and intercept cover the value within $1 \sim 3\sigma$. Each pull, yield, and error fitting result is shown in Appendix C.


doi:doi:10.6342/NTU202203205

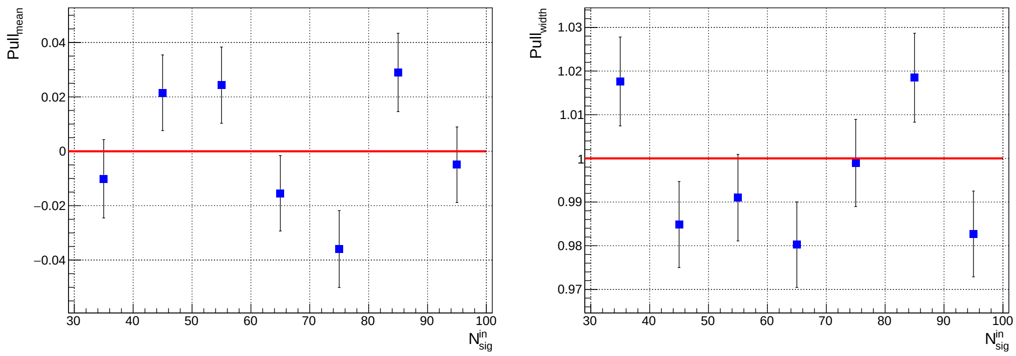


(a) (b)

Figure 4.11: Pull mean and pull width plot of toyMC ensemble test for each input signal number

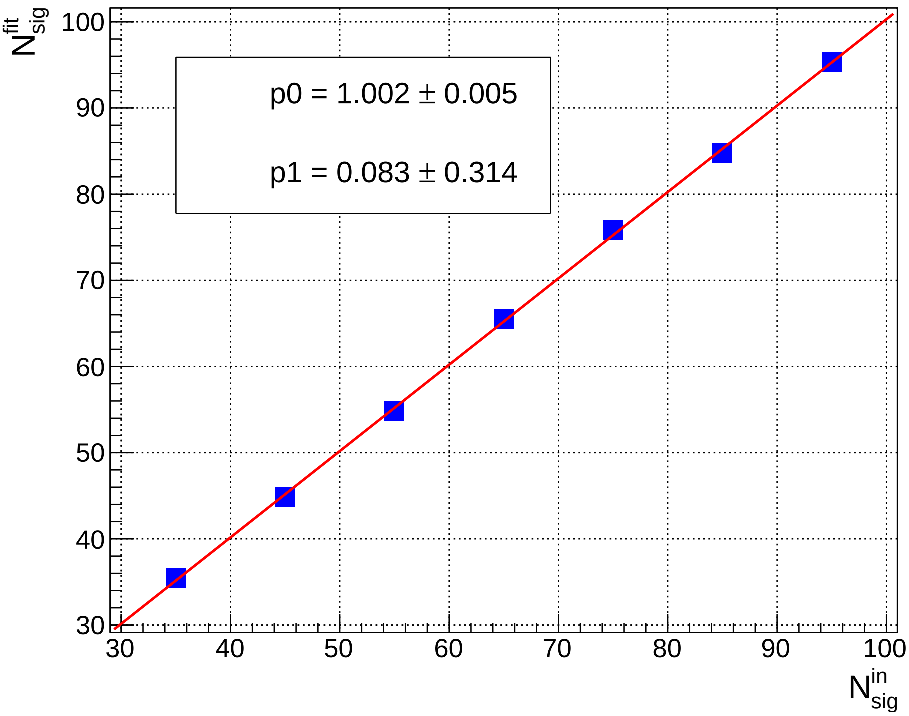


Figure 4.12: Gsim linearity test. The p0 is slope and the p1 is intercept of 1st order polynomial.



doi:doi:10.6342/NTU202203205

| $N_{input}^{B^0\to p\bar{\Sigma}^0\pi^-}$ | $N_{fit}^{B^0\to p\bar{\Sigma}^0\pi^-}$ | $Pull_{mean}^{B^0\to p\bar{\Sigma}^0\pi^-}$ | $Pull_{width}^{B^0\to p\bar{\Sigma}^0\pi^-}$ | $error_{mean}^{B^0\to p\bar{\Sigma}^0\pi^-}$ |
|---|---|---|---|---|
| 95 | $95.30 \pm 0.26$ | $-0.005 \pm 0,014$ | $0.983 \pm 0.010$ | $18.98 \pm 0.01$ |
| 85 | $84.73 \pm 0.27$ | $0.029 \pm 0.014$ | $1.018 \pm 0.010$ | $18.64 \pm 0.01$ |
| 75 | $75.89 \pm 0.26$ | $-0.036 \pm 0.014$ | $0.999 \pm 0.010$ | $18.35 \pm 0.01$ |
| 65 | $65.50 \pm 0.25$ | $-0.015 \pm 0.014$ | $0.980 \pm 0.010$ | $18.14 \pm 0.01$ |
| 55 | $54.79 \pm 0.25$ | $0.024 \pm 0.014$ | $0.991 \pm 0.010$ | $17.60 \pm 0.01$ |
| 45 | $44.87 \pm 0.24$ | $0.022 \pm 0.014$ | $0.985 \pm 0.010$ | $17.22 \pm 0.01$ |
| 35 | $35.41 \pm 0.24$ | $-0.010 \pm 0.014$ | $1.018 \pm 0.010$ | $17.03 \pm 0.01$ |

Table 4.7: Detailed result of gsim ensemble test for $B^0 \to p\bar{\Sigma}^0\pi^-$

| $N_{input}^{B^0\to p\bar{\Sigma}^0\pi^-}$ | $N_{fit}^{B^0\to p\bar{\Lambda}\pi^-}$ | $Pull_{mean}^{B^0\to p\bar{\Lambda}\pi^-}$ | $Pull_{width}^{B^0\to p\bar{\Lambda}\pi^-}$ | $error_{mean}^{B^0\to p\bar{\Lambda}\pi^-}$ |
|---|---|---|---|---|
| 95 | $190.33 \pm 0.23$ | $-0.004 \pm 0.014$ | $0.993 \pm 0.010$ | $16.36 \pm 0.01$ |
| 85 | $189.97 \pm 0.23$ | $0.018 \pm 0.014$ | $0.989 \pm 0.010$ | $16.35 \pm 0.01$ |
| 75 | $190.16 \pm 0.23$ | $0.007 \pm 0.014$ | $1.004 \pm 0.010$ | $16.34 \pm 0.01$ |
| 65 | $190.00 \pm 0.23$ | $0.017 \pm 0.014$ | $0.997 \pm 0.010$ | $16.33 \pm 0.01$ |
| 55 | $190.60 \pm 0.23$ | $-0.021 \pm 0.014$ | $0.973 \pm 0.010$ | $16.32 \pm 0.01$ |
| 45 | $190.26 \pm 0.23$ | $0.001 \pm 0.014$ | $0.985 \pm 0.010$ | $16.30 \pm 0.01$ |
| 35 | $190.40 \pm 0.23$ | $-0.007 \pm 0.014$ | $1.014 \pm 0.010$ | $16.30 \pm 0.01$ |

Table 4.8: Detailed result of gsim ensemble test for $B^0 \to p\bar{\Lambda}\pi^-$

## 4.5 $M_{p\bar{\Lambda}}$ Distribution Study with MC Sample

In order to show how we claim which decay type our signal follows, we apply 2D fitting we mention above in different $M_{p\bar{\Lambda}}$ bin region. In this part, we only use MC sample to see whether our fitting yields are consistent with expected distribution. Table 4.9 and 4.10 show the detail of fitting result in each $M_{p\bar{\Lambda}}$ bin.



doi:doi:10.6342/NTU202203205

| $M_{p\bar{\Lambda}}$(GeV/c$^2$) | Fitting Yield(signal) | Expected Yield(signal) |
|---|---|---|
| 2.0-2.2 | 51.64± 8.62 | 49 |
| 2.2-2.4 | 21.60± 7.25 | 18 |
| 2.4-2.8 | 14.38± 7.58 | 14 |
| 2.8-3.4 | 19.19± 7.43 | 8 |
| 3.4-5.0 | 7.37±8.77 | 3 |

Table 4.9: $B^0 \to p\bar{\Sigma}^0\pi^-$ fitting yield in each $M_{p\bar{\Lambda}}$ bin

| $M_{p\bar{\Lambda}}$(GeV/c$^2$) | Fitting Yield($B^0 \to p\bar{\Lambda}\pi^-$) | Expected Yield($B^0 \to p\bar{\Lambda}\pi^-$) |
|---|---|---|
| 2.0-2.2 | 121.26± 11.52 | 118 |
| 2.2-2.4 | 59.02± 8.32 | 60 |
| 2.4-2.8 | 32.01± 6.32 | 32 |
| 2.8-3.4 | 14.33± 4.74 | 14 |
| 3.4-5.0 | 11.82± 5.10 | 8 |

Table 4.10: $B^0 \to p\bar{\Lambda}\pi^-$ fitting yield in each $M_{p\bar{\Lambda}}$ bin

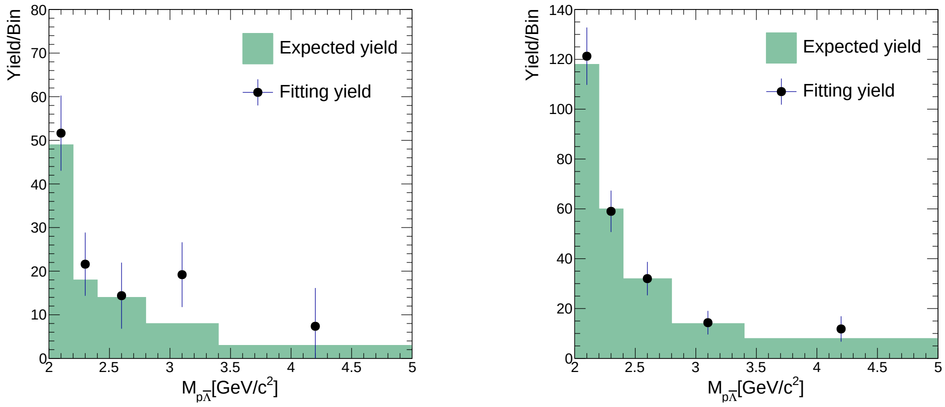


(a) (b)

Figure 4.13: Comparison plot of expected yield and fitting yield for $B^0 \to p\bar{\Sigma}^0\pi^-$ and $B^0 \to p\bar{\Lambda}\pi^-$ channels in different $M_{p\bar{\Lambda}}$ bin. The green shaded one is obtained from signal MC and expected branching fraction, and the data points are fitting result of pseudo-experiment of each $M_{p\bar{\Lambda}}$ bin.

Fig 4.14 to 4.18 are pseudo-experiment fitting plots for each bin where blue line is total PDF, red dashed line is signal PDF, purple dashed line is background PDF, green


doi:doi:10.6342/NTU202203205

dashed line is self-crossfeed of $B^0 \to p\bar{\Lambda}\pi^-$ and black dashed line is $B^0 \to p\bar{\Lambda}\pi^-$

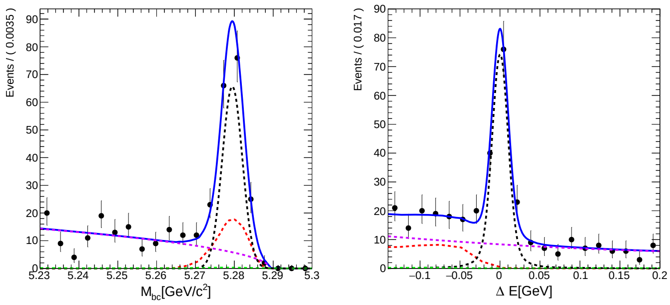


Figure 4.14: Pseudo-experiment plot in $M_{p\bar{\Lambda}}$ bin1

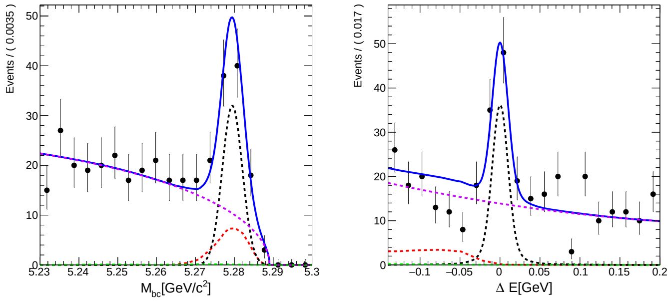


Figure 4.15: Pseudo-experiment plot in $M_{p\bar{\Lambda}}$ bin2

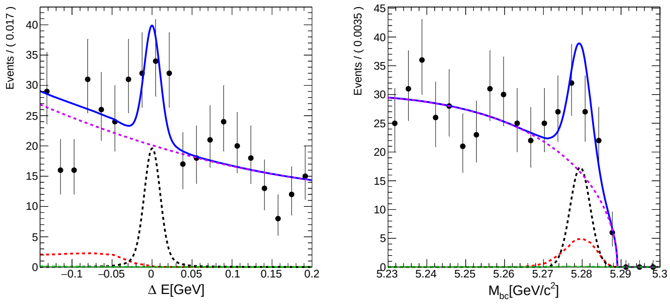


Figure 4.16: Pseudo-experiment plot in $M_{p\bar{\Lambda}}$ bin3



doi:doi:10.6342/NTU202203205

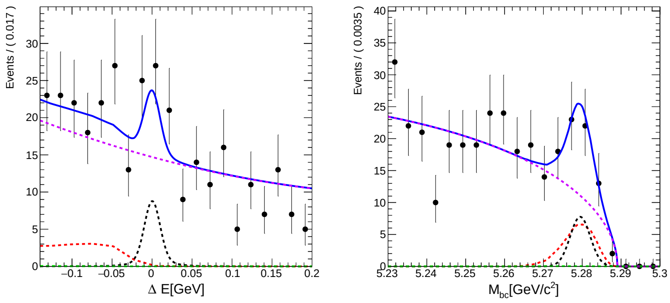


Figure 4.17: Pseudo-experiment plot in $M_{p\bar{\Lambda}}$ bin4

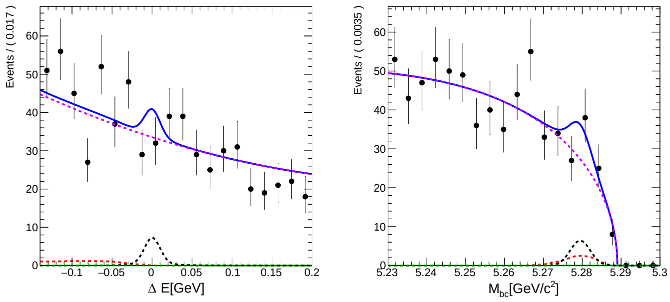


Figure 4.18: Pseudo-experiment plot in $M_{p\bar{\Lambda}}$ bin5



doi:doi:10.6342/NTU202203205

doi:doi:10.6342/NTU202203205

# Chapter 5

# Control Sample

In order to determine the implicit systematic uncertainty of our analysis, we tend to apply it on some well-measured decay mode which have similar property of our signal as control sample and follow the similar steps to see its accuracy and error. For the calibration of efficiency drop of background suppression, we decide to use $B^0 \to D^-\pi^+$ and $D^- \to K_S^0\pi^-$ which has topologically similar final states with $B^0 \to p\bar{\Lambda}\pi^-$ and larger statistics.

## 5.1 Data Sample

Signal MC and background MC are generated following the list in Table 5.1 and Table 5.2.

| Decay | Model used | Events generated |
|---|---|---|
| $\Upsilon(4S) \to B^0\bar{B}^0$ | VSS BMIX dm | |
| $B^0 \to D^-\pi^+$ | PHSP | $771 \times 10^3$ |
| $D^- \to K_S^0\pi^-$ | PHSP | |

Table 5.1: EvtGen decay mode for control sample signal MC

| Background type | Physics type | Events generated |
|---|---|---|
| Generic BB | $b \to c$ transition mixed and charged exclude $B^0 \to D^-\pi^+$ | $10 \times$ data |
| Continuum $q\bar{q}$ | $e^+e^- \to q\bar{q}(u\bar{u}, d\bar{d}, c\bar{c}, s\bar{s})$ | $6\times$ data |

Table 5.2: Background type used for control sample



doi:doi:10.6342/NTU202203205

## 5.2 Event Selection

The selection criteria of $B^0 \to D^-\pi^+$is listed in Table 5.3.

| Particle type | Selection |
|---|---|
| $\pi^\pm$ | $\mathscr{L}_{K/\pi} < 0.4$ for $\pi^\pm$ come from $D^-$ and $B^0$<br>$\lvert dr \rvert < 0.3$ cm, $\lvert \mathrm{dz} \rvert < 3$ cm for $\pi^\pm$ come from $D^-$ and $B^0$ |
| $K_S^0$ | $\texttt{goodKshort} = 1, 0.488\ \mathrm{GeV/c^2} < \mathrm{M}_{\pi\pi} < 0.508\ \mathrm{GeV/c^2}$<br>$\chi^2_{\pi\pi} < 20.$ |
| $D^-$ | $1.84\ \mathrm{GeV/c^2} < \mathrm{M}_{\pi\pi\pi} < 1.9\ \mathrm{GeV/c^2}$ |

Table 5.3: Particle basic selection for $B^0 \to D^-\pi^+$

## 5.3 Background Suppression

In order to calibrate the efficiency drop of our mode, we hire NeuroBayes package again and use the same training algorithm generated in continuum suppression section, then we cut the same value of NeuroBayes output as we mention before, all variables are listed in Table 3.2 .

## 5.4 PDF Modeling

We still use 2D fitting here. The components of our fitting PDF are listed in Table 5.4, the proportion of self-crossfeed is very low and is hard to be model so we use 2D histogram PDF to model it. The fitting result of signal and background are shown in Fig 5.1 to Fig 5.3.

| | $M_{bc}$ | $\Delta E$ |
|---|---|---|
| Signal | One Gaussian | Double Gaussian |
| continuum $q\bar{q}$ | ARGUS Distribution | 2nd Order Chebyshev Polynomial |
| Generic BB | 2D smooth HistPDF | |
| Self-cross feed | 2D smooth HistPDF | |

Table 5.4: PDFs modeling for $B^0 \to D^-\pi^+$



doi:doi:10.6342/NTU202203205

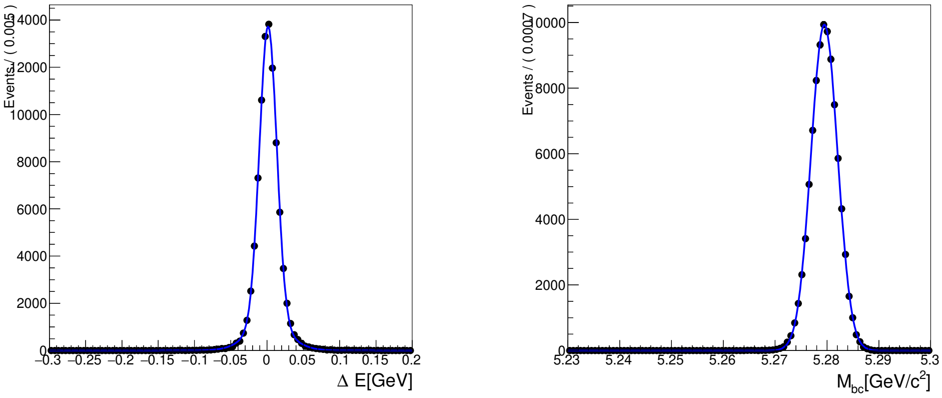


Figure 5.1: PDFs for $B^0 \to D^- \pi^+$

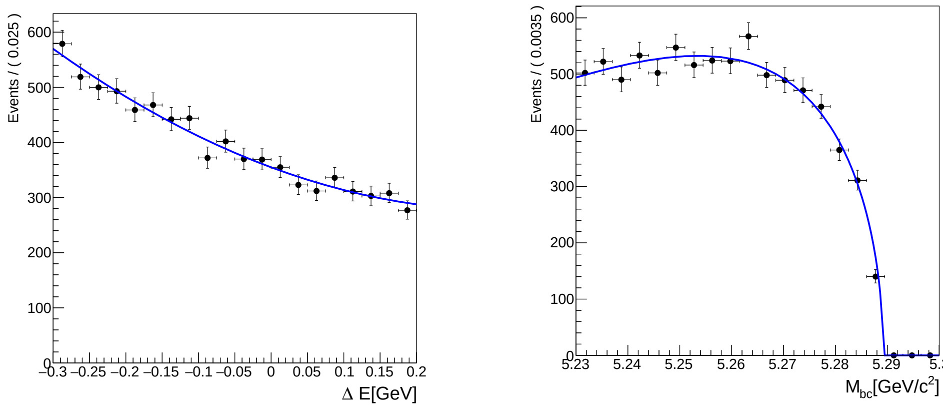


Figure 5.2: PDFs for continuum $q\bar{q}$

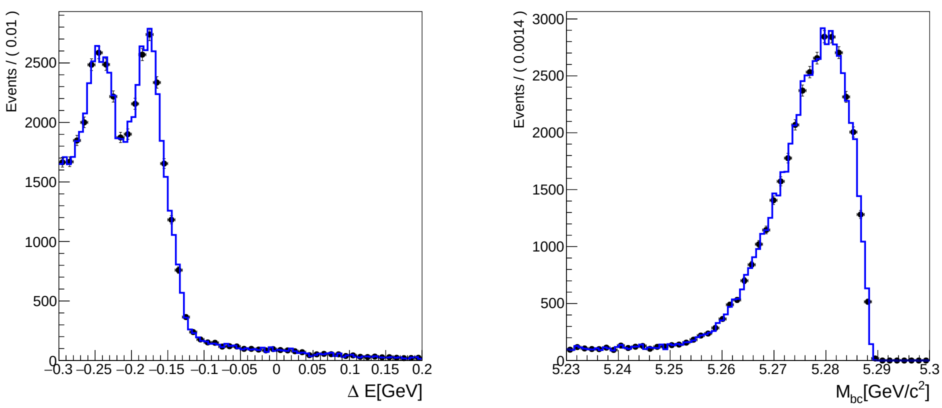


Figure 5.3: PDFs for generic $B\bar{B}$



doi:doi:10.6342/NTU202203205

## 5.5 Fitting Result

To obtain the branching fraction and efficiency drop, we divide our data sample into two samples, the first one is the data greater than `CSMVA` cut 0.8, and the second one is the sample lower than 0.8, then we apply simultaneous fit with those two sample to fit branching fraction and efficiency drop directly. Here is how we define signal yield for each sample, and the fitting results are shown in Fig 5.4 and Fig 5.5.

$$\begin{aligned} Yield_{sig}^{CSMVA>0.8} &= N_{B\bar{B}} \times \mathscr{B}_{B\to D^-\pi^+} \times \mathscr{B}_{D\to K_s\pi^-} \times \varepsilon_{D^-\pi^+} \times \varepsilon_{drop} \times (\mathscr{C}_{PID}) \\ Yield_{sig}^{CSMVA<0.8} &= N_{B\bar{B}} \times \mathscr{B}_{B\to D^-\pi^+} \times \mathscr{B}_{D\to K_s\pi^-} \times \varepsilon_{D^-\pi^+} \times (1-\varepsilon_{drop}) \times (\mathscr{C}_{PID}) \end{aligned} \tag{5.1}$$

Finally, we obtain the branching fraction $2.55 \times 10^{-6}$ and efficiency drop 50.52% which are listed in Tab 5.5.

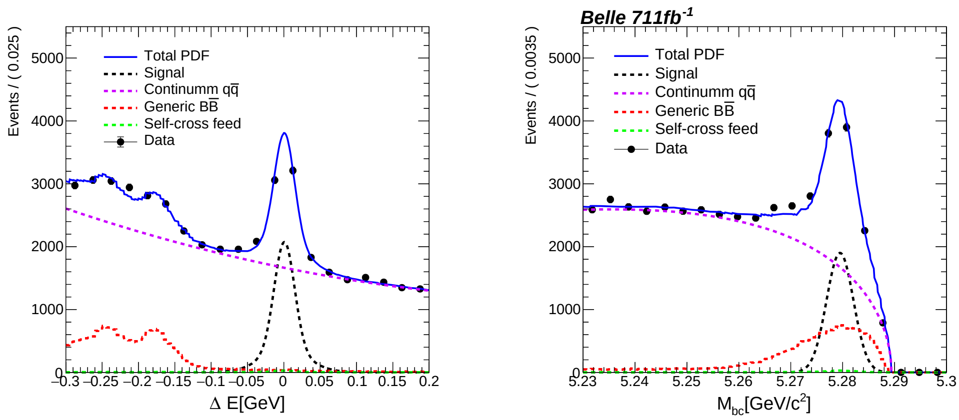


Figure 5.4: Fitting result of control sample data `CSMVA` $< 0.8$

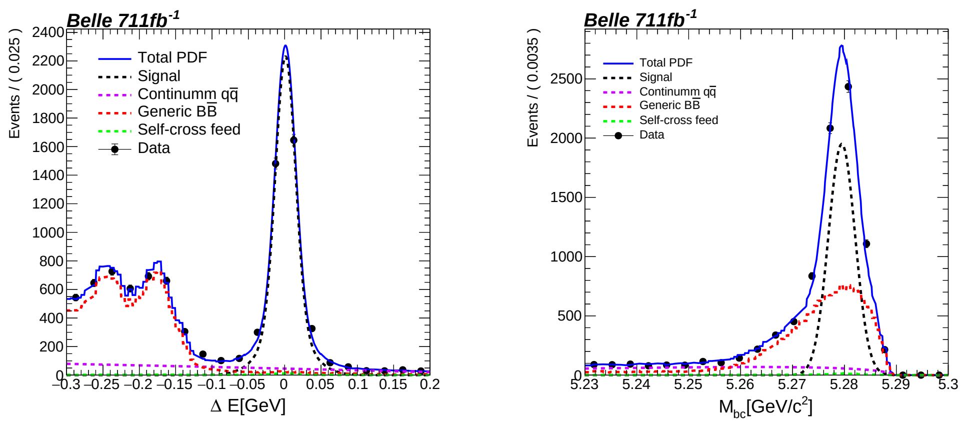


Figure 5.5: Fitting result of control sample data `CSMVA` $> 0.8$



doi:doi:10.6342/NTU202203205

## 5.6 Calibration on Continuum Suppression Efficiency

In order to calibrate the efficiency drop between signal MC and data, we compare both efficiency drop to calculate the ratio as the calibration factor, the detail of calibration is shown in Table 5.5.

| Fitting Parameter | Fitting Result |
|---|---|
| efficiency drop | $50.52 \pm 0.94\%$ |
| Branching fraction | $(2.55 \pm 0.05) \times 10^{-3}$ |

Table 5.5: Fitting parameter result

| | MC | Data |
|---|---|---|
| Ratio (After/Before) | $51.10 \pm 0.57$ % | $50.52 \pm 0.94$ % |
| Calibration Factor | $0.989 \pm 0.024$ | |
| Uncertainty | 2.43% | |

Table 5.6: Calibration on continuum suppression

## 5.7 Conclusion

We obtained the calibration factor of continuum suppression with control sample $B^0 \to D^-\pi^+$. In order to validate the correction of our fitting, we measure the branching fraction of $B^0 \to D^-\pi^+$, the formula of Branch fraction is given as

$$\mathscr{B}(B^0 \to D^-\pi^+) = \frac{Yield}{771581000 \times (Efficiency) \times 0.0156 \times (PIDfactor)} \tag{5.2}$$

where 0.0156 is branch fraction of subdecay $D^- \to K_S^0\pi^-$ according to the PDG value[11], and the PID factor is the calibration factor for PID selection which is 0.954 and 0.958 for $\pi$ID selection. The measurement of the branching fraction of our fitting is equal to $2.55 \pm 0.05 \times 10^{-3}$ which is consistent with the PDG value[12] which is $2.51 \pm 0.08 \times 10^{-3}$


doi:doi:10.6342/NTU202203205

doi:doi:10.6342/NTU202203205

# Chapter 6

# Unblind Results

## 6.1 Fitting Results

Fig 6.1 and 6.2 show the unblind results with whole $M_{p\bar{\Lambda}}$ region. We measure $50.29^{+18.06}_{-17.38}$ $B^0 \to p\bar{\Sigma}^0\pi^-$ signal yield and $215.45^{+17.36}_{-16.62}$ $B^0 \to p\bar{\Lambda}\pi$ yield, and the detailed fitting and open box results are summarized in Tab 6.4. In order to obtain higher significant signal yields, we also try to fit the yields in the threshold enhancement region $M_{p\bar{\Lambda}} <$ 2.8 GeV/c$^2$ which is shown in Fig 6.3 and 6.4. In the threshold enhancement region ($M_{p\bar{\Lambda}} < 2.8$ GeV/c$^2$), we measure the $B^0 \to p\bar{\Sigma}^0\pi^-$ signal yield $36.70^{+11.82}_{-11.09}$, $184.82^{+15.20}_{-14.52}$ $B^0 \to p\bar{\Lambda}\pi^-$ yield, and also obtain the increasing significance. The result also shows the evidence of exist of threshold enhancement in $B^0 \to p\bar{\Sigma}^0\pi^-$ channel.



doi:doi:10.6342/NTU202203205

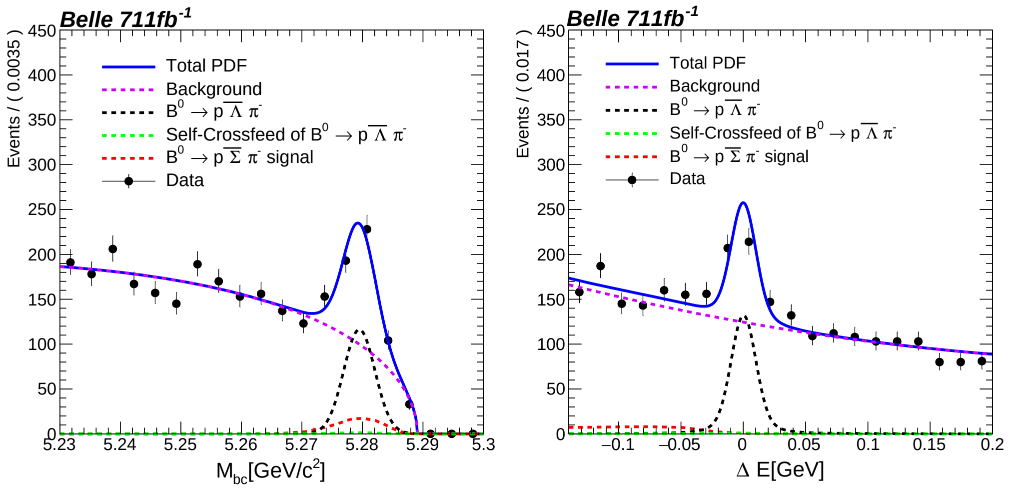


Figure 6.1: $M_{bc}$ (left) and ΔE (right) plots of unblind results in whole $M_{p\bar{\Lambda}}$ region

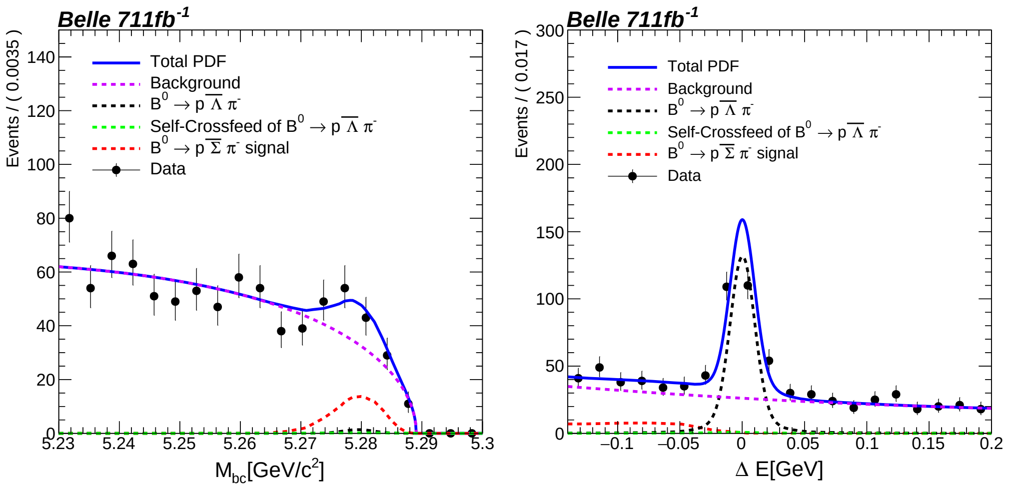


Figure 6.2: $M_{bc}$ (left) and ΔE (right) projected plots of unblind results in whole $M_{p\bar{\Lambda}}$ region. The projected regions are $-0.14 < \Delta E < -0.05$ GeV for $M_{bc}$ plot and $M_{bc} > 5.26\ \mathrm{GeV/c^2}$ for $\Delta E$ plot.


doi:doi:10.6342/NTU202203205

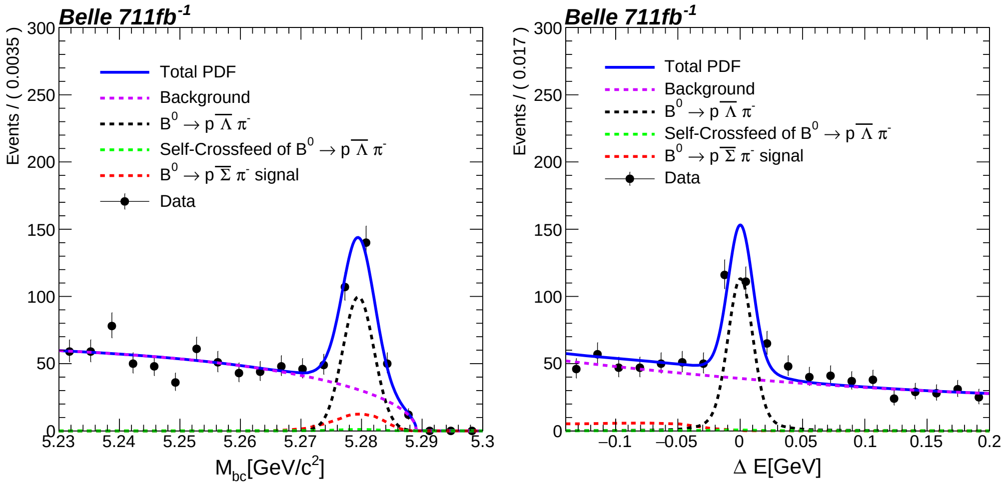


Figure 6.3: $M_{bc}$ (left) and $\Delta$E (right) projected plots of unblind results in $M_{p\bar{\Lambda}}$ region $<$ 2.8 GeV/c$^2$.

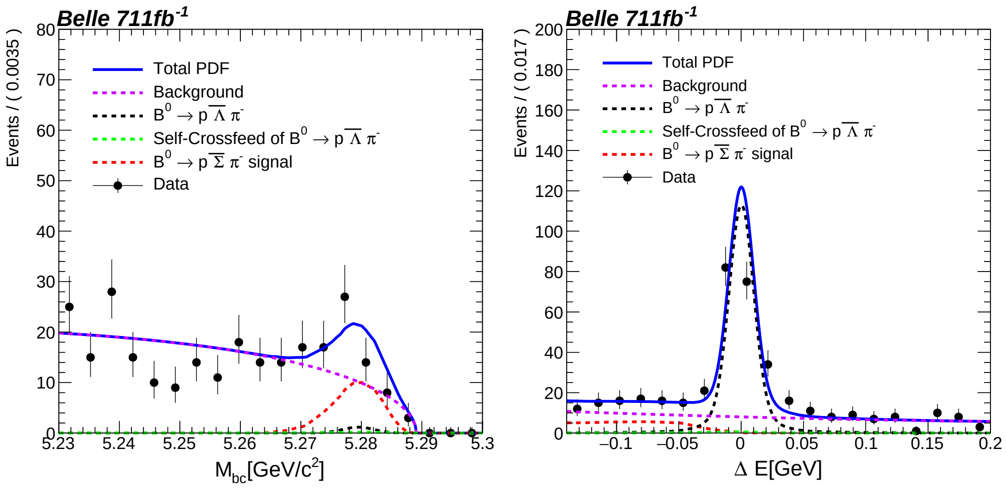


Figure 6.4: $M_{bc}$ (left) and $\Delta$E (right) projected plots of unblind results in $M_{p\bar{\Lambda}}$ region $<$ 2.8GeV/c$^2$. The projected regions are $-0.14 < \Delta E < -0.05$ GeV for $M_{bc}$ plot and $M_{bc} > 5.26$ GeV/c$^2$ for $\Delta E$ plot.



doi:doi:10.6342/NTU202203205

## 6.2 Threshold Enhancement Result

In order to study threshold enhancement in our signal modes, we obtain the yields in different $M_{p\bar{\Lambda}}$ bin and calculate the branching fraction with calibrated efficiency in each bin. Because we don't measure enough yields in $B^0 \to p\bar{\Sigma}^0\pi^-$ channel to calculate precise differential branching fraction, we only observe a convincible result in $B^0 \to p\bar{\Lambda}\pi^-$ channel. Fig 6.5 shows the $M_{p\bar{\Lambda}}$ distribution, and Fig 6.6 to 6.13 are the fitting result of each $M_{p\bar{\Lambda}}$ bin where blue line is total PDF, red dashed line is signal PDF, purple dashed line is background PDF, green dashed line is self-crossfeed of $B^0 \to p\bar{\Lambda}\pi^-$ and black dashed line is $B^0 \to p\bar{\Lambda}\pi^-$.

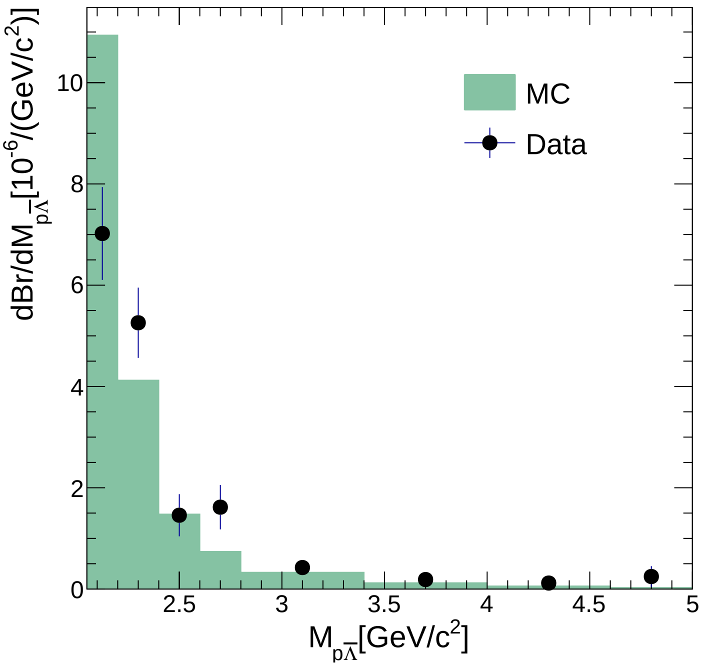


Figure 6.5: Differential branching fraction for $B^0 \to p\bar{\Lambda}\pi^-$ on $M_{p\bar{\Lambda}}$ dimension from threshold to limit, the green shadowed one is obtained from signal MC and the data points are obtain from fitting yields of data and corresponding signal efficiency of each $M_{p\bar{\Lambda}}$ bin.



doi:doi:10.6342/NTU202203205

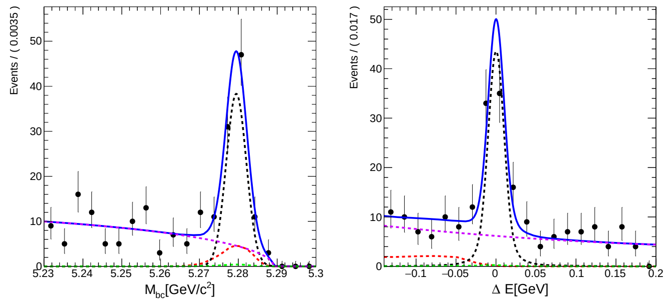


Figure 6.6: 0-th $M_{p\bar{\Lambda}}$ bin

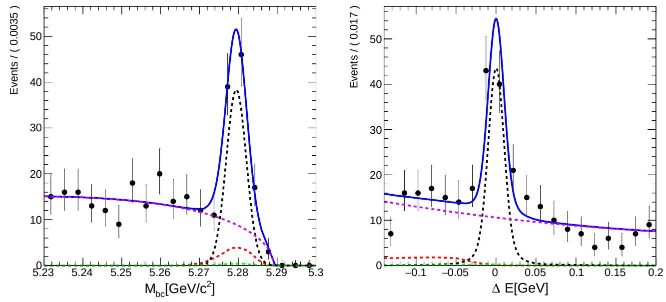


Figure 6.7: 1-st $M_{p\bar{\Lambda}}$ bin

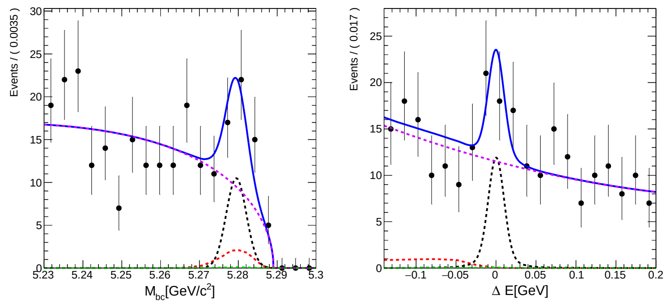


Figure 6.8: 2-nd $M_{p\bar{\Lambda}}$ bin

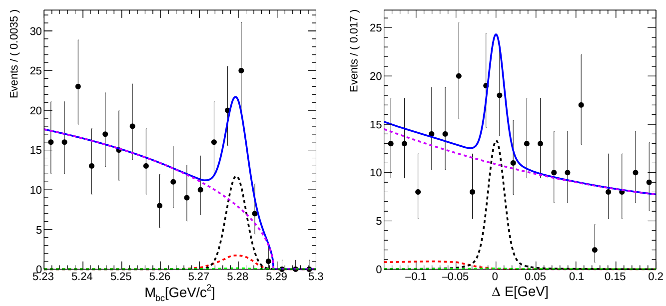


Figure 6.9: 3-rd $M_{p\bar{\Lambda}}$ bin



doi:doi:10.6342/NTU202203205

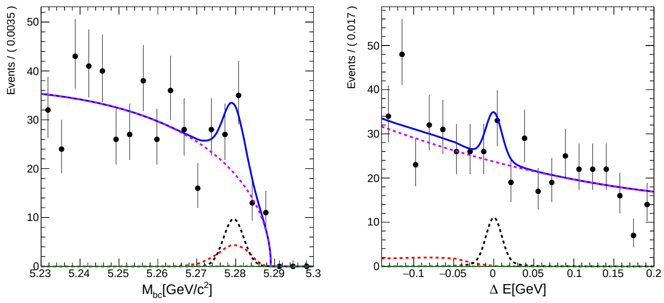


Figure 6.10: 4-th $M_{p\bar{\Lambda}}$ bin

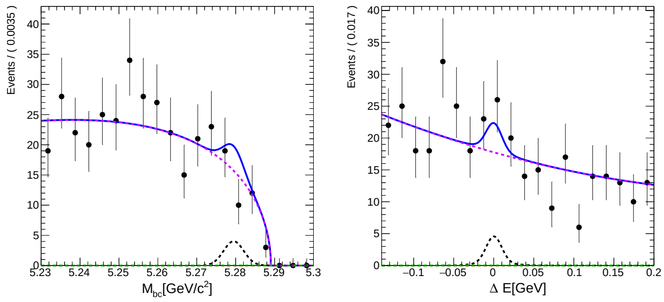


Figure 6.11: 5-th $M_{p\bar{\Lambda}}$ bin

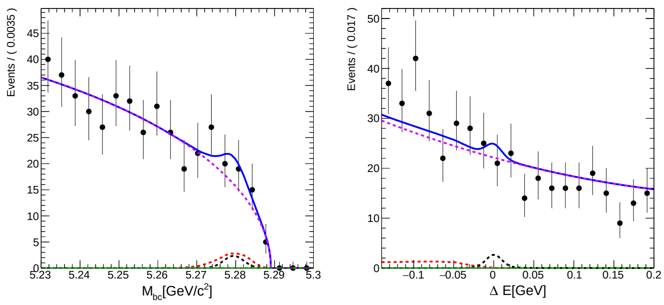


Figure 6.12: 6-th $M_{p\bar{\Lambda}}$ bin

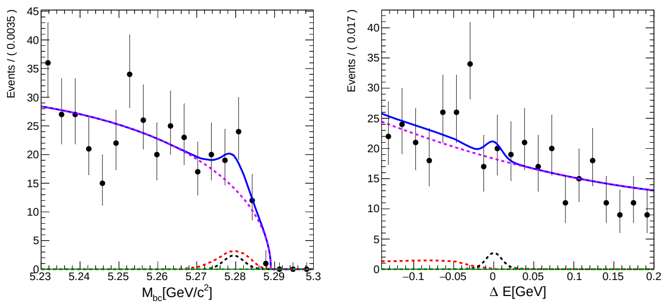


Figure 6.13: 7-th $M_{p\bar{\Lambda}}$ bin



doi:doi:10.6342/NTU202203205

| | $B^0 \to p\bar{\Lambda}\pi^-$ | | | $B^0 \to p\bar{\Sigma}^0\pi^-$ | | |
|---|---|---|---|---|---|---|
| $M_{p\bar{\Lambda}}(\mathrm{GeV/c^2})$ | Yield | $\mathscr{B}(10^{-6})$ | $\varepsilon_{eff}(\%)$ | Yield | $\mathscr{B}(10^{-6})$ | $\varepsilon_{eff}(\%)$ |
| Threshold-2.2 | $71.17^{+9.30}_{-8.51}$ | $1.04^{+0.14}_{-0.13}$ | 10.07 | $13.24^{+5.82}_{-5.12}$ | $0.27^{+0.12}_{-0.11}$ | 7.14 |
| 2.2-2.4 | $71.25^{+9.40}_{-8,70}$ | $1.04^{+0.14}_{-0.13}$ | 10.09 | $11.33^{+6.60}_{-5.93}$ | $0.24^{+0.14}_{-0.12}$ | 7.05 |
| 2.4-2.6 | $19.51^{+5.57}_{-4.84}$ | $0.29^{+0.09}_{-0.07}$ | 9.97 | $5.96^{+6.14}_{-5.51}$ | $0.13^{+0.13}_{-0.12}$ | 6.93 |
| 2.6-2.8 | $21.81^{+5.92}_{-5.18}$ | $0.32^{+0.09}_{-0.08}$ | 10.05 | $5.11^{+5.75}_{-5.03}$ | $0.12^{+0.13}_{-0.11}$ | 6.52 |
| 2.8-3.4 | $18.07^{+5.64}_{-4.87}$ | $0.25^{+0.08}_{-0.07}$ | 10.57 | $12.70^{+8.29}_{-7.72}$ | $0.29^{+0.19}_{-0.18}$ | 6.50 |
| 3.4-4.0 | $7.62^{+4.23}_{-3.50}$ | $0.11^{+0.06}_{-0.05}.$ | 10.10 | $-9.02^{+5.66}_{-4.87}$ | $-0.22^{+0.14}_{-0.12}$ | 5.98 |
| 4.0-4.6 | $4.39^{+3.88}_{-3.08}$ | $0.07^{+0.06}_{-0.05}$ | 9.23 | $8.56^{+7.16}_{-6.58}$ | $0.23^{+0.20}_{-0.17}$ | 5.55 |
| 4.6-limit. | $3.82^{+3.77}_{-2.92}$ | $0.09^{+0.09}_{-0.07}$ | 5.97 | $3.86^{+7.02}_{-6.37}$ | $0.11^{+0.20}_{-0.18}$ | 5.10 |

Table 6.1: Yields, efficiencies and measured branching fractions in different $M_{p\bar{\Lambda}}$ bin for $B^0 \to p\bar{\Lambda}\pi^-$ and $B^0 \to p\bar{\Sigma}^0\pi^-$



doi:doi:10.6342/NTU202203205

## 6.3 $cos\theta_p$ Asymmetry

We also do the $cos\theta_p$ asymmetry study for $B^0 \to p\bar{\Lambda}\pi^-$, in order to draw the $cos\theta_p$ distribution, we obtain the differential branching fraction with signal yields and calibrated efficiency in each $cos\theta_p$ bin. Fig 6.14 shows the $cos\theta_p$ distribution and we also observe the $cos\theta_p$ asymmetry with more data than previous study. Tab 6.2 shows the fitting detailed information in each $cos\theta_p$ bin.

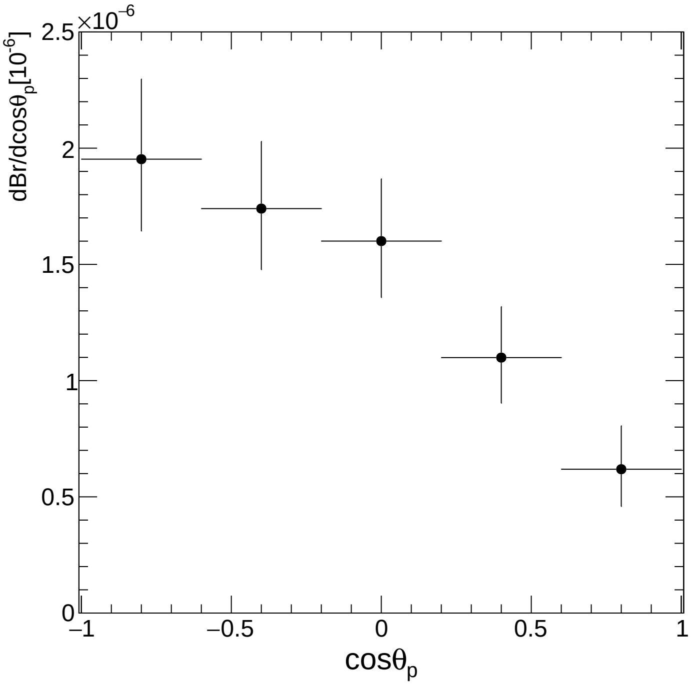


Figure 6.14: Differential branching fraction for $B^0 \to p\bar{\Lambda}\pi^-$ of $cos\theta_p$ in baryon pair rest frame in $M_{p\bar{\Lambda}} < 2.8$ GeV/c$^2$

| | $B^0 \to p\bar{\Lambda}\pi^-$ | | | $B^0 \to p\bar{\Sigma}^0\pi^-$ | | |
|---|---|---|---|---|---|---|
| $cos\theta_p$ | Yield | $\mathscr{B}(10^{-6})$ | $\varepsilon_{eff}(\%)$ | Yield | $\mathscr{B}(10^{-6})$ | $\varepsilon_{eff}(\%)$ |
| -1.0 -0.6 | $43.23^{+7.56}_{-6.87}$ | $0.79^{+0.14}_{-0.13}$ | 8.19 | $9.09^{+5.98}_{-5.35}$ | $0.20^{+0.13}_{-0.12}$ | 6.79 |
| -0.6 -0.2 | $46.07^{+7.63}_{-6.97}$ | $0.70^{+0.12}_{-0.11}$ | 9.84 | $11.72^{+5.69}_{-5.02}$ | $0.23^{+0.11}_{-0.10}$ | 7.39 |
| -0.2 0.2 | $46.31^{+7.70}_{-7.06}$ | $0.64^{+0.11}_{-0.10}$ | 10.76 | $4.66^{+5.36}_{-4.6}$ | $0.09^{+0.11}_{-0.10}$ | 7.47 |
| 0.2 0.6 | $33.05^{+6.57}_{-5.90}$ | $0.44^{+0.09}_{-0.08}$ | 11.18 | $8.22^{+5.51}_{-4.78}$ | $0.17^{+0.11}_{-0.10}$ | 7.18 |
| 0.6 1.0 | $17.25^{+5.19}_{-4.47}$ | $0.25^{+0.07}_{-0.06}$ | 10.36 | $2.24^{+4.94}_{-4.32}$ | $0.05^{+0.11}_{-0.10}$ | 6.48 |

Table 6.2: Yields, efficiencies and measured branching fractions in different $cos\theta_p$ bin for $B^0 \to p\bar{\Lambda}\pi^-$ and $B^0 \to p\bar{\Sigma}^0\pi^-$



doi:doi:10.6342/NTU202203205

## 6.4 PDF Uncertainty

In order to consider the uncertainty caused by PDF, first, we fit the yield 1000 times by changing the PDF fixed parameters with random uniform distribution and take the maximum deviation as the uncertainty. Second, we change our $\Delta E$ background PDF into third order polynomial, then combine those two uncertainty as one PDF uncertainty. Table 6.3 shows the systematic uncertainty estimation.

| | $B^0 \to p\bar{\Sigma}^0\pi^-$ | $B^0 \to p\bar{\Lambda}\pi^-$ |
|---|---|---|
| Signal PDF uncertainty | 3.16% | 0.81% |
| Background PDF uncertainty | 0.90% | 1.11% |
| PDF uncertainty | 3.29% | 1.37% |

Table 6.3: PDF uncertainty

## 6.5 Significance Estimation

The significance estimation is done by profile likelihood corresponding to the parameter $\theta_0$, where $\theta_0$ is the parameter we are interested in like signal yields. The estimation function of significance is given as

$$Significance = \sqrt{-2log(\frac{L(\theta_0)}{L(\hat{\theta}_0)})} \tag{6.1}$$

where $\hat{\theta}_0$ denotes fitting result of the parameter we interested in, and $\theta_0$ is the null hypothesis (Fitting yield = 0 ). Since there is non-negligible systematic error caused by PDF modeling, we need to consider it into the significance estimation by a smeared likelihood function which is given as

$$\mathscr{L}_{smear}(n) = \int_{-\infty}^{+\infty} \mathscr{L}(n') \frac{e^{\frac{-(n-n')^2}{2\sigma^2}}}{\sqrt{2\pi}\sigma} dn' \tag{6.2}$$

where $\sigma$ is PDF modeling systematic error. Fig 6.15 shows the log likelihood ratio plot.


doi:doi:10.6342/NTU202203205

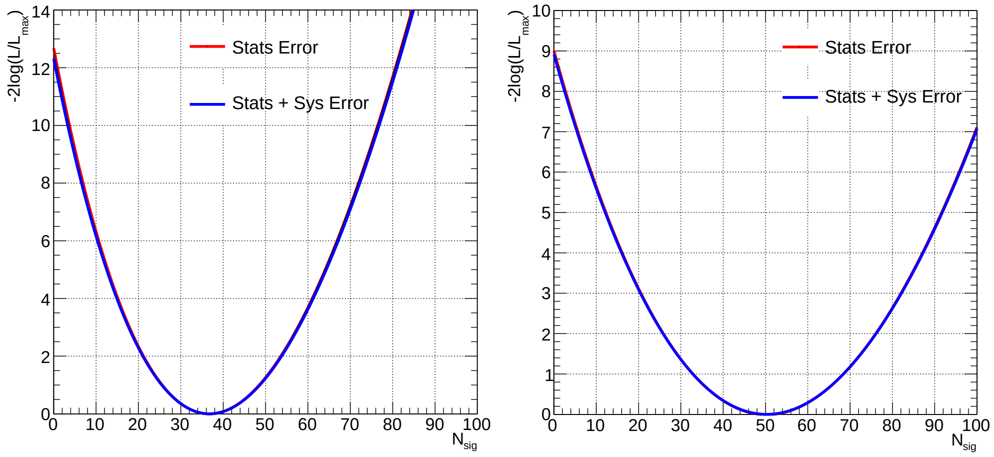


Figure 6.15: log likelihood ratio distribution for $B^0 \to p\bar{\Sigma}^0\pi^-$, the red line is only considered statistical error, and the blue line is likelihood smeared with systematic error. LHS is TE region and RHS is whole region

## 6.6 Summary

The summary of unblind result is shown in Table 6.4 and 6.5.

| Channels | Yield | Significance(Stats error) | Significance(Stats+Sys error) |
|---|---|---|---|
| $B^0 \to p\bar{\Sigma}^0\pi^-$ | $50.29^{+18.06}_{-17.38}$ | $3.00\sigma$ | $2.98\sigma$ |
| $B^0 \to p\bar{\Lambda}\pi^-$ | $215.45^{+17.36}_{-16.62}$ | $21.12\sigma$ | $18.52\ \sigma$ |

Table 6.4: Whole $M_{p\bar{\Lambda}}$ region fitting results for unblind result

| Channels | Yield | Significance(Stats error) | Significance(Stats+Sys error) |
|---|---|---|---|
| $B^0 \to p\bar{\Sigma}^0\pi^-$ | $36.70^{+11.82}_{-11.09}$ | $3.56\sigma$ | $3.51\sigma$ |
| $B^0 \to p\bar{\Lambda}\pi^-$ | $184.84^{+15.20}_{-14.52}$ | $23.80\sigma$ | $18.55\sigma$ |

Table 6.5: TE region fitting results for unblind result


doi:doi:10.6342/NTU202203205

# Chapter 7

# Systematic Uncertainty

## 7.1 Number of $B\bar{B}$ pairs uncertainty

According to official release, there are $(771.581 \pm 10.566) \times 10^6$ $B\bar{B}$ pairs in real data from exp7 to exp65, and the systematic error is 1.37% from reference[13].

## 7.2 Tracking Uncertainty

In Belle Note 1165[14], tracking reconstruction of charged particle is studied by using partially reconstructed $D^{*+} \to D^0(\pi^-\pi^+K_S^0)\pi^+$ decay sample. Comparing the tracking efficiency between data and signal MC, the systematic uncertainty has been evaluated to be $(-0.13 \pm 0.30(stat.) \pm 0.10(syst.))\%$ per track. The suggestion of systematic uncertainty is of 0.35% per track which is applied in our analysis. There are four tracks in $B^0 \to p\bar{\Sigma}^0\pi^-$ and $B^0 \to p\bar{\Lambda}\pi^-$, so the systematic uncertainty is 1.4%.

## 7.3 Charged Particle Identification Uncertainty

Proton and $\pi$ identification are studied by various control samples in Belle-Note 779 and Belle-Note 1279[15][16] respectively, the former one is $D^{*+} \to D^0(K^-\pi^+)\pi^+$ and the later one is $\Lambda \to p\pi^-$. The systematic uncertainty are estimated by using the official table which is provided by the PID joint group to calculate the calibration factor between



doi:doi:10.6342/NTU202203205

data and signal MC. The uncertainty and calibration factor has been evaluated in Tab 7.1 7.2, and the systematic uncertainty is defined by $\frac{statistical\ error}{mean\ value}$.

| Channel | Calibration Factor | Uncertainty |
|---|---|---|
| $B^0 \to p\bar{\Lambda}\pi^-$ | $0.945 \pm 0.006$ | 0.63% |
| $B^0 \to p\bar{\Sigma}^0\pi^-$ | $0.940 \pm 0.006$ | 0.64% |

Table 7.1: Calibration factor and uncertainty on Proton Identification

| Channel | Calibration Factor | Uncertainty |
|---|---|---|
| $B^0 \to p\bar{\Lambda}\pi^-$ | $0.943 \pm 0.007$ | 0.74% |
| $B^0 \to p\bar{\Sigma}^0\pi^-$ | $0.943 \pm 0.007$ | 0.74% |

Table 7.2: Calibration factor and uncertainty on $\pi$ Identification

## 7.4 $\Lambda$ Selection Uncertainty

$\Lambda$ selection is according to good$\Lambda$ selection in Belle-Note 684[8]. We use the number of signal MC in three different $\Lambda$ mass regions which is based on belle note 684 to obtain the systematic uncertainty 3.4%.

## 7.5 Secondary Subdecay Uncertainty

The systematic error from subdecay is calculated by the ratio of uncertainty to the corresponding branching fraction in PDG :$BR(\Lambda \to p\pi^-) = (63.9 \pm 0.5)\%$[17] , so the subdecay systematic error is 0.8%.

## 7.6 Continuum Suppression Uncertainty

We have estimated the systematic uncertainty of continuum suppression in chapter 5, and the value is listed in Tab 5.6. The systematic uncertainty is 2.43% based on our study.



doi:doi:10.6342/NTU202203205

## 7.7 MC Modeling

Because of our ignorance of true physics about the signal, we need to quote the systematic uncertainty for the MC modeling. In order to obtain the uncertainty, we take the efficiency difference from the two signal MC which we generated with PHSP and TE as systematic uncertainty which is listed in Tab 7.3. According to our open box result, we discover about 70% signal yields in threshold enhancement region ($M_{p\bar{\Lambda}} < 2.8(GeV/c^2)$) with 3.5 $\sigma$ significance. That shows the evidence that our signal more follows threshold enhancement. Base on this premise, we modify this systematic uncertainty by

$$Modified\ uncertainty = \frac{\varepsilon_{TE} - (ratio * \varepsilon_{TE} + (1 - ratio) * \varepsilon_{PHSP})}{\varepsilon_{TE}} \tag{7.1}$$

where ratio is $\frac{Yield\ (TE\ region)}{Yield\ (Whole\ region)}$

| | $\varepsilon_{PHSP}$ | $\varepsilon_{TE}$ | Maximum uncertainty $\frac{\varepsilon_{PHSP}-\varepsilon_{TE}}{\varepsilon_{TE}}$ | Modified uncertainty |
|---|---|---|---|---|
| $B^0 \to p\bar{\Sigma}^0\pi^-$ | 5.65% | 7.00% | 19.28% | 5.21% |

Table 7.3: Comparison between phase space and threshold enhancement for signal channel

For $B^0 \to p\bar{\Lambda}\pi^-$ channel, in order to correct the MC model, we obtain the systematic uncertainty of MC modeling by reweight each $M_{p\bar{\Lambda}}$ bin contribution, and the reweighted efficiency and the systematic uncertainty are listed in Tab 7.4.

| | $\varepsilon_{eff}$ | Reweighted $\varepsilon_{eff}$ | Uncertainty |
|---|---|---|---|
| $B^0 \to p\bar{\Lambda}\pi^-$ | 10.06% | 9.98% | 0.8% |

Table 7.4: MC modeling uncertainty for $B^0 \to p\bar{\Lambda}\pi^-$

## 7.8 PDF Uncertainty

We have estimated the PDF uncertainty in Sec 6.4 which is listed in Tab 6.3.



doi:doi:10.6342/NTU202203205

## 7.9 Summary of Systematic Error

The all kinds of systematic uncertainty are listed in Table 7.5 for both channels.

| Source | $B^0 \to p\bar{\Lambda}\pi^-$ | $B^0 \to p\bar{\Sigma}^0\pi^-$ |
|---|---|---|
| Number of $B\bar{B}$ | 1.37% | 1.37% |
| Tracking | 1.40% | 1.40% |
| Proton ID | 0.63% | 0.64% |
| $\pi$ ID | 0.74% | 0.74% |
| Subdecay | 0.80% | 0.80% |
| $\Lambda$ Selection | 3.40% | 3.40% |
| Continuum Suppression | 2.45% | 2.45% |
| MC Modeling | 0.8% | 5.21% |
| PDF Modeling | 1.37% | 3.29% |
| Summary | 5.04% | 7.80 % |

Table 7.5: Summary of Systematic Uncertainty

## 7.10 Summary of Calibration Factor

| Source | $B^0 \to p\bar{\Lambda}\pi^-$ | $B^0 \to p\bar{\Sigma}^0\pi^-$ |
|---|---|---|
| Proton ID | 0.945 | 0.941 |
| $\pi$ID | 0.943 | 0.943 |
| Continuum Suppression | 0.989 | 0.989 |
| Summary | 0.881 | 0.878 |

Table 7.6: Summary of Calibration Factor



doi:doi:10.6342/NTU202203205

# Chapter 8

# Conclusion

In $B^0 \to p\bar{\Sigma}^0\pi^-$ channel, we measure 3.5$\sigma$ signal yield which disobeys the current QCD model prediction, and set an upper limit on the branching fraction in threshold enhancement region. In $B^0 \to p\bar{\Lambda}\pi^-$ channel, we update the branching fraction and differential branching fraction on $M_{p\bar{\Lambda}}$ and $cos\theta_p$ dimension, and observe the asymmetry of $cos\theta_p$. The measurement results of each decay channel are listed in Tab 8.1. The formula of branching fraction is given as

$$\mathscr{B} = \frac{Yields}{771581000 \times \varepsilon_{sig} \times \mathscr{C}_{PID} \times \mathscr{C}_{CSMVA}} \tag{8.1}$$

where $\varepsilon_{sig}$ is signal efficiency, $\mathscr{C}_{PID}$ is PID calibration factor, and $\mathscr{C}_{CSMVA}$ is continuum suppression calibration factor.

## 8.1 Upper Limit Estimation

Since we don't observe significant signal yield, we evaluate the 90% confidence level Bayesian upper limit of branching fraction which is obtained by integral likelihood function given as.

$$\int_0^{N_{Upper}} \mathscr{L}(n)dn = 0.9\int_0^{\infty} \mathscr{L}(n)dn \tag{8.2}$$

where $\mathscr{L}(n)$ is likelihood corresponding to the fitting yield shown in Fig 8.1. Also the


doi:doi:10.6342/NTU202203205

likelihood is smeared by the systematic error. We determine the upper limit of branching fraction of $B^0 \to p\bar{\Sigma}^0\pi^-$ to be $1.2 \times 10^{-6}$ with 90% confidence level.

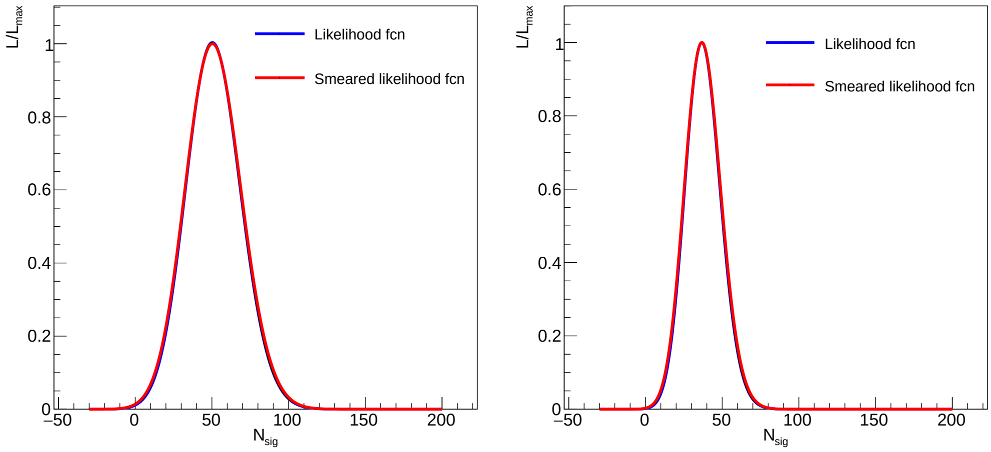


Figure 8.1: likelihood ratio distribution for $B^0 \to p\bar{\Sigma}^0\pi^-$, the red line is only considered statistical uncertainty, and the blue line is likelihood smeared with systematic error. LHS is TE region and RHS is whole $M_{p\bar{\Lambda}}$ region

## 8.2 Summary

| Channel | $\mathscr{B}(10^{-6})$ | Upper Limit (90%C-L) | Significance |
|---|---|---|---|
| $B^0 \to p\bar{\Sigma}^0\pi^-$ | $0.86^{+0.28}_{-0.26} \pm 0.07$ | $< 1.2 \times 10^{-6}$ | $3.5\ \sigma$ |
| $B^0 \to p\bar{\Lambda}\pi^-$ | $3.15^{+0.25}_{-0.24} \pm 0.16$ | - | $18.55\ \sigma$ |

Table 8.1: Summary of the measurement


doi:doi:10.6342/NTU202203205

# Appendix A

# Trianing Variable

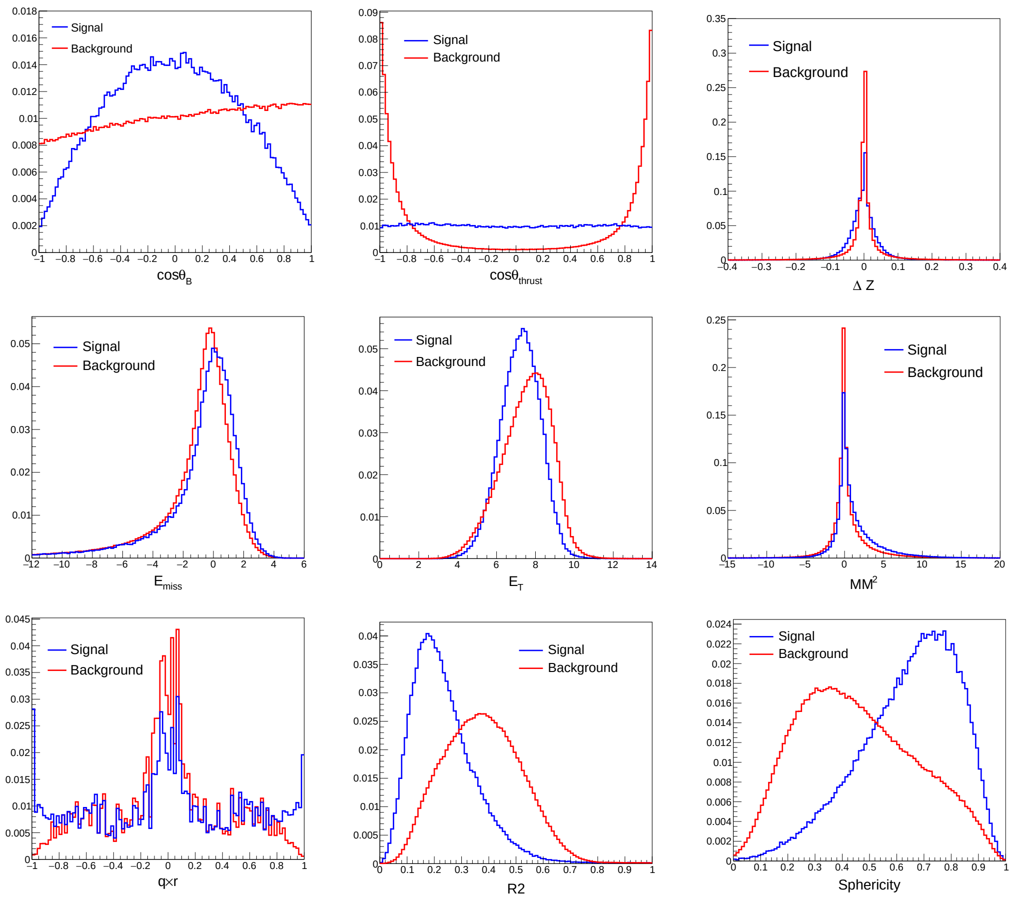


Figure A.1: Shape variables



doi:doi:10.6342/NTU202203205

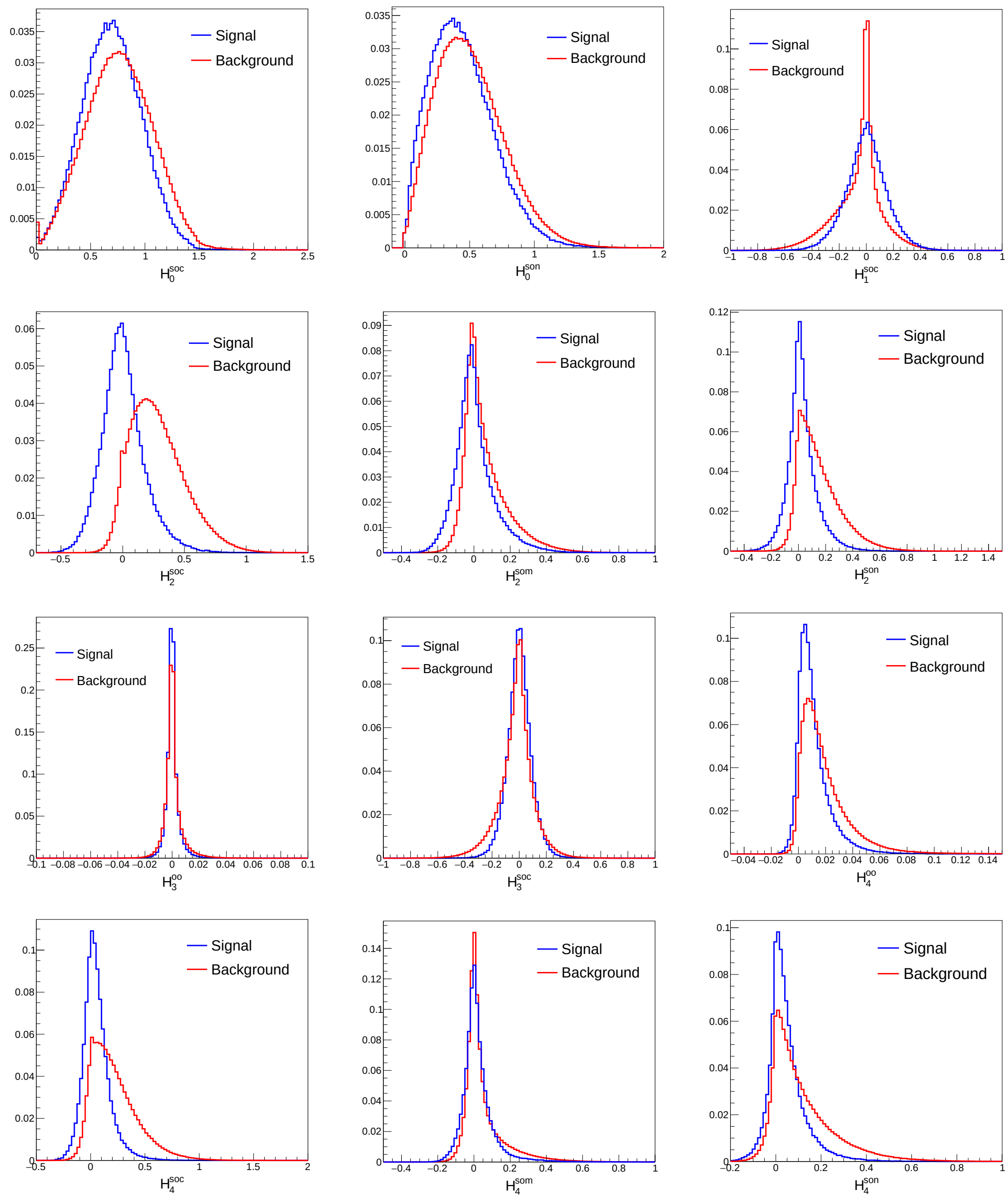


Figure A.2: KSFW



doi:doi:10.6342/NTU202203205

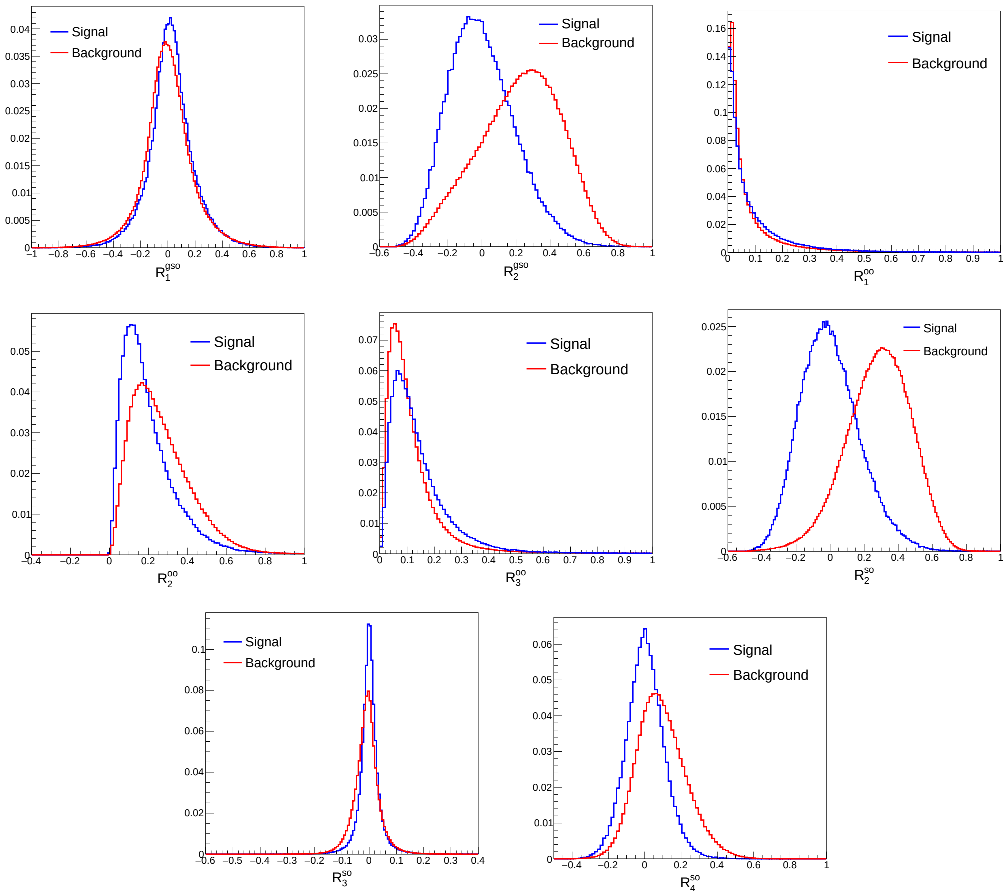


Figure A.3: SFW


doi:doi:10.6342/NTU202203205

doi:doi:10.6342/NTU202203205

# Appendix B

# ToyMC Fitter Test

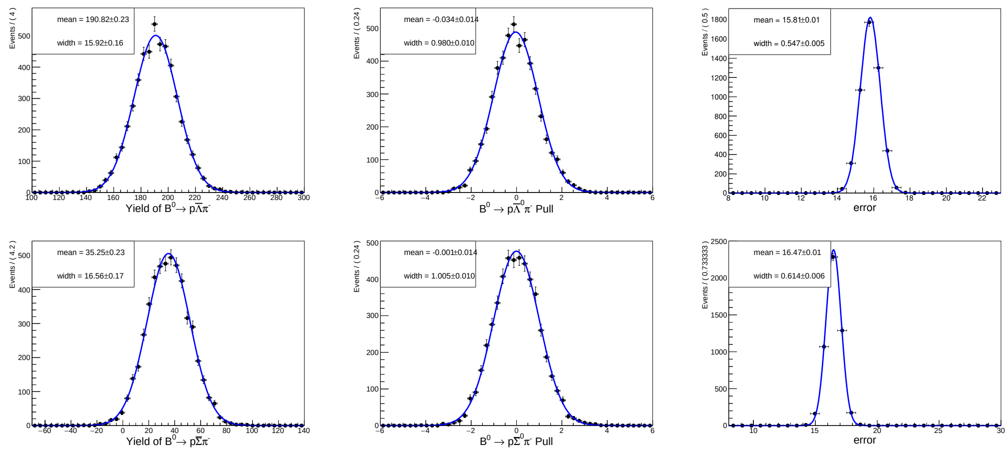


Figure B.1: ToyMC fitter result for $N_{sig}$ = 35

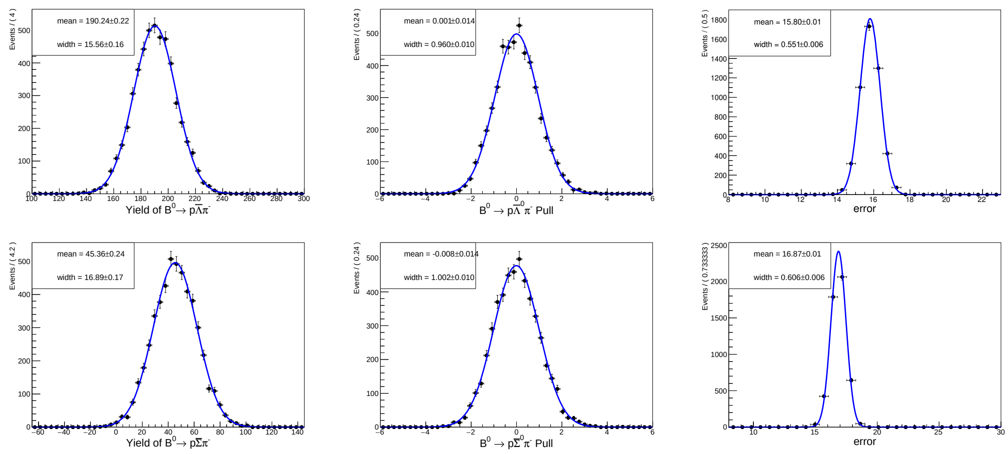


Figure B.2: ToyMC fitter result for $N_{sig}$ = 45



doi:doi:10.6342/NTU202203205

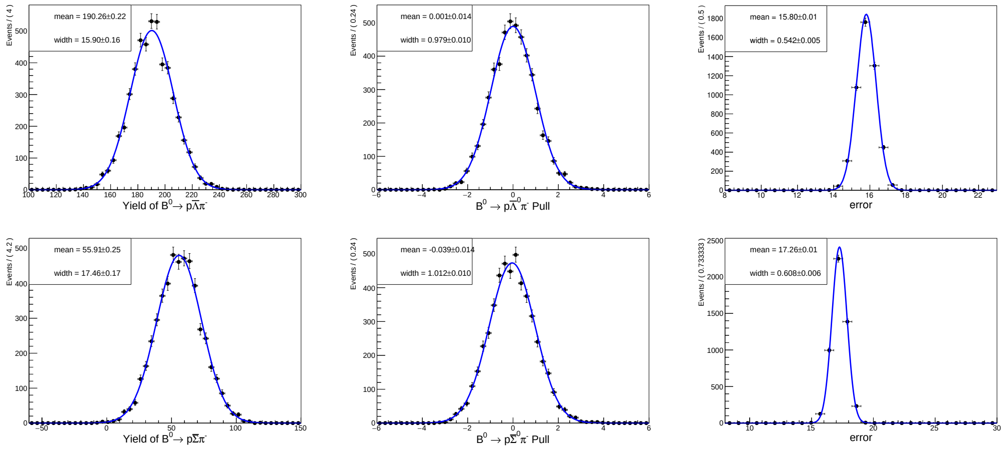


Figure B.3: ToyMC fitter result for $N_{sig}$ = 55

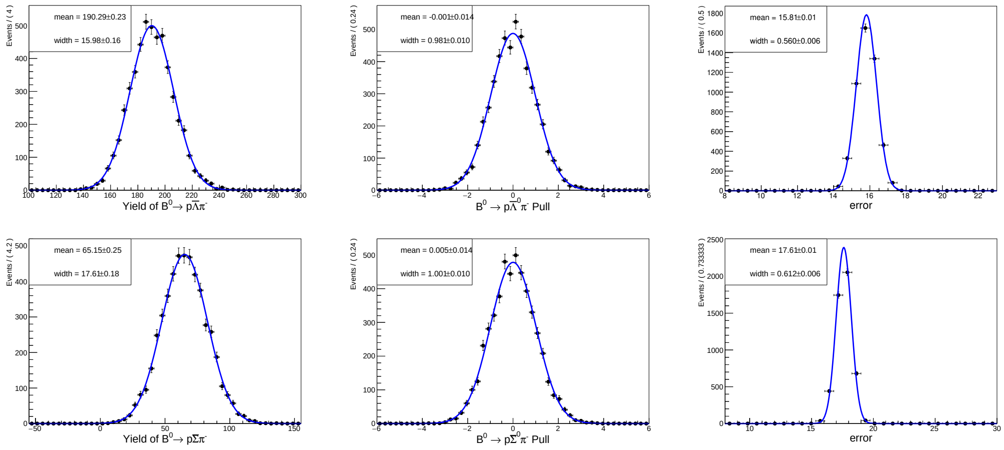


Figure B.4: ToyMC fitter result for $N_{sig}$ = 65

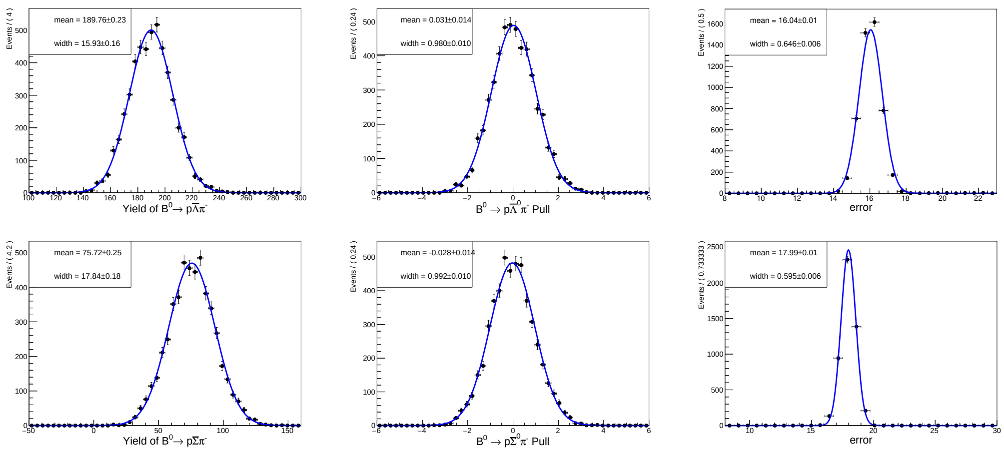


Figure B.5: ToyMC fitter result for $N_{sig}$ = 75


doi:doi:10.6342/NTU202203205

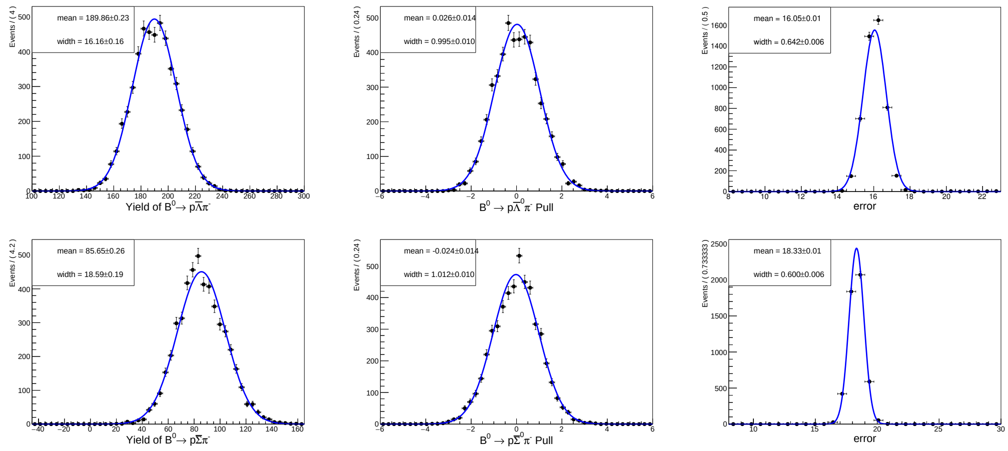


Figure B.6: ToyMC fitter result for $N_{sig} = 85$

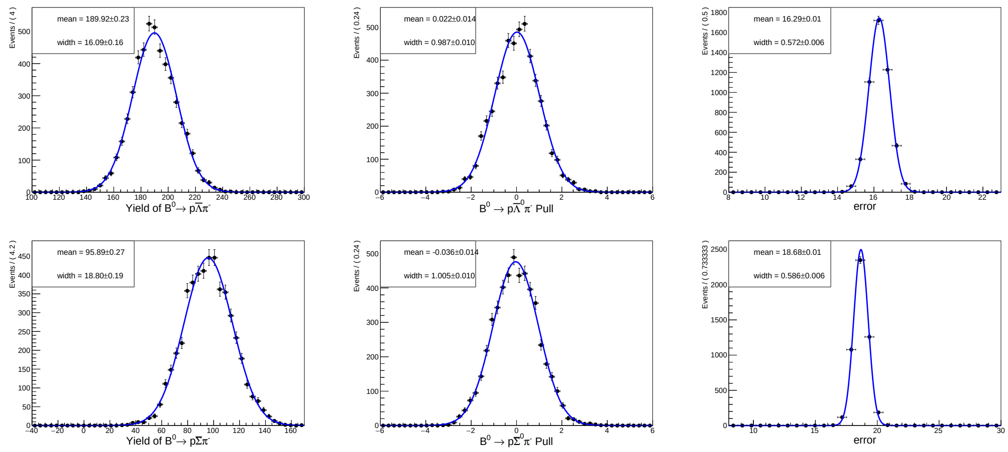


Figure B.7: ToyMC fitter result for $N_{sig} = 95$



doi:doi:10.6342/NTU202203205

doi:doi:10.6342/NTU202203205

# Appendix C

# Gsim Fitter Test

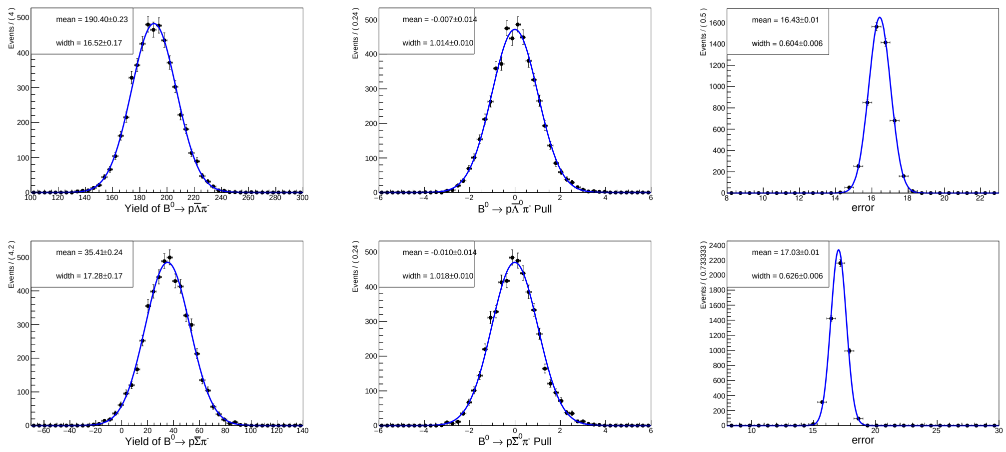


Figure C.1: Gsim fitter result for $N_{sig} = 35$

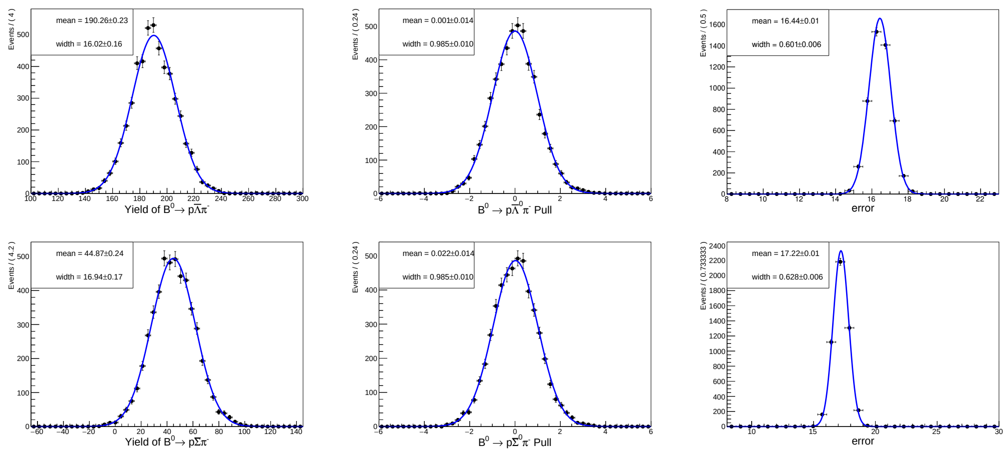


Figure C.2: Gsim fitter result for $N_{sig} = 45$


doi:doi:10.6342/NTU202203205

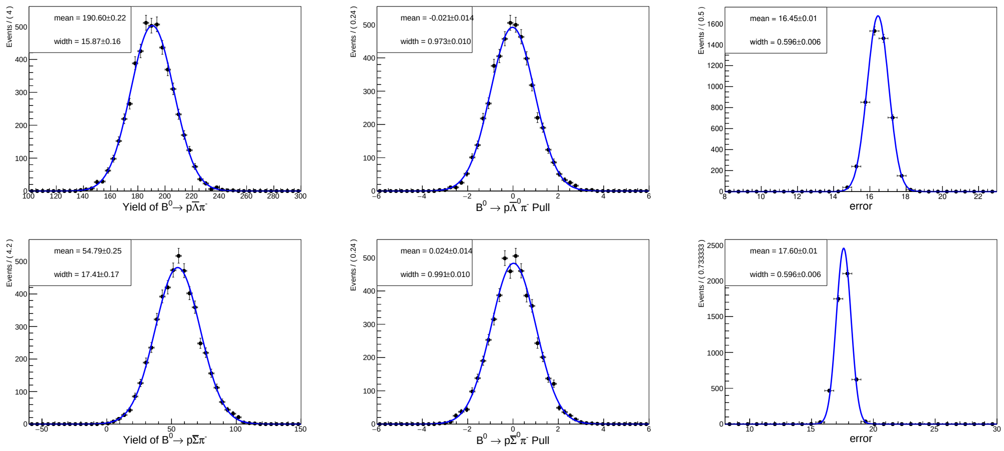


Figure C.3: Gsim fitter result for $N_{sig} = 55$

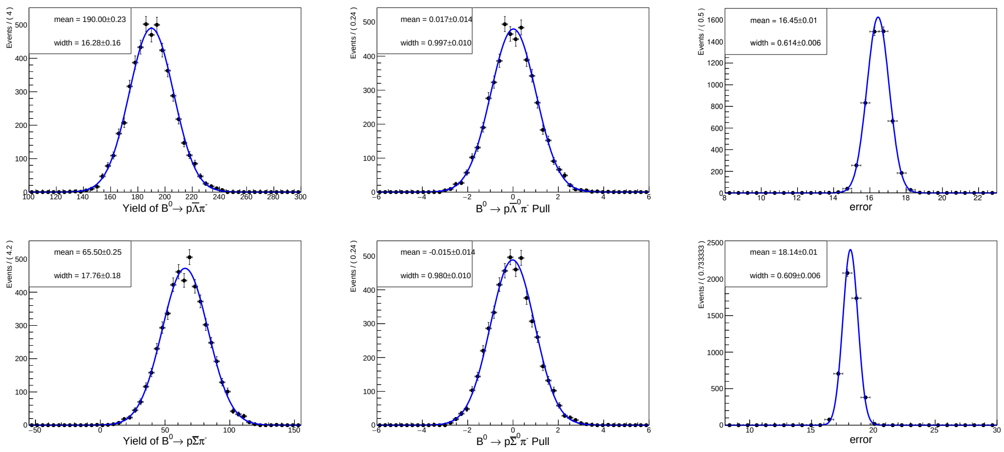


Figure C.4: Gsim fitter result for $N_{sig} = 65$

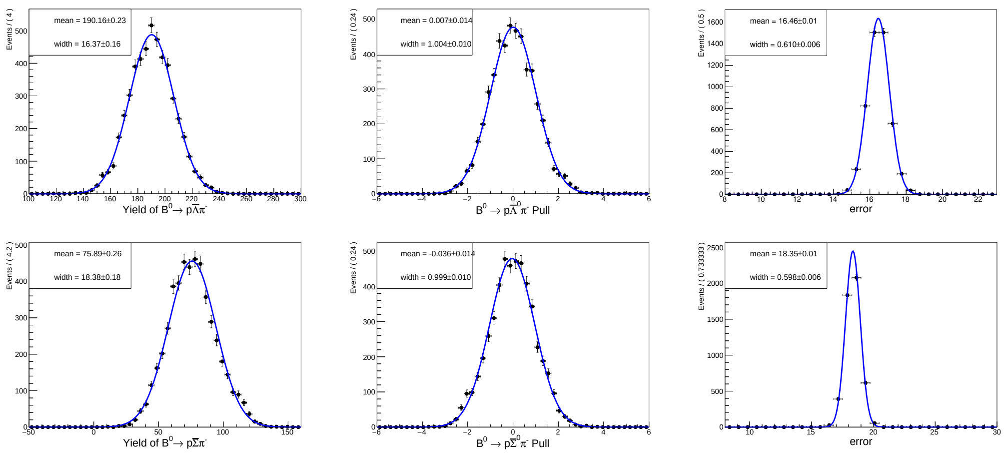


Figure C.5: Gsim fitter result for $N_{sig} = 75$



doi:doi:10.6342/NTU202203205

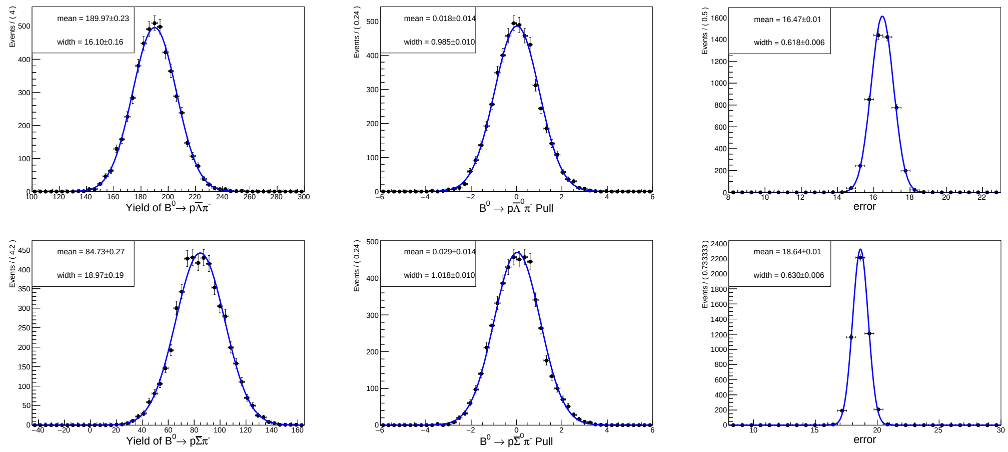


Figure C.6: Gsim fitter result for $N_{sig}$ = 85

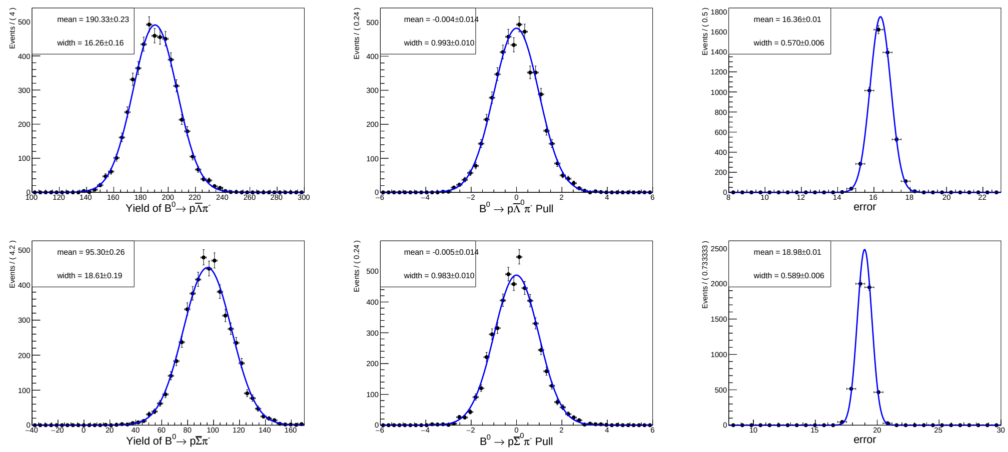


Figure C.7: Gsim fitter result for $N_{sig}$ = 95



doi:doi:10.6342/NTU202203205

# Bibliography


[1] *The Belle detector*, Nuclear Instruments and Methods in Physics Research Section A: Accelerators, Spectrometers, Detectors and Associated Equipment **479**, 117 (2002), Detectors for Asymmetric B-factories.

[2] H.-Y. Cheng and K.-C. Yang, *Charmless exclusive baryonic B decays*, Phys. Rev. D **66**, 014020 (2002).

[3] C.-K. Hou, W.-S. Chua, *Three-body baryonic $\overline{B} \to \Lambda\bar{p}\pi$decays and such*, The European Physical Journal C - Particles and Fields **29**, 27 (2003).

[4] M.-Z. Wang *et al.*, *Study of $B^+ \to p\overline{\Lambda}\gamma$, $p\overline{\Lambda}\pi^0$ and $B^0 \to p\overline{\Lambda}\pi^-$*, Phys. Rev. D **76**, 052004 (2007).

[5] C.-K. Chua, W.-S. Hou, and S.-Y. Tsai, *Charmless three-body baryonic B decays*, Phys. Rev. D **66**, 054004 (2002).

[6] D. J. Lange, *The EvtGen particle decay simulation package*, Nucl. Instrum. Meth. A **462**, 152 (2001).

[7] R. Brun, A. C. McPherson, P. Zanarini, M. Maire, and F. Bruyant, *GEANT 3 : user's guide Geant 3.10, Geant 3.11*, 1987.

[8] Y.-J. L. K-F. Chen, T.-L. Kuo, *$\Lambda$ Selection at Belle*, Belle Note 684 (2004).

[9] M. Feindt and U. Kerzel, *The NeuroBayes neural network package*, Nucl. Instrum. Meth. A **559**, 190 (2006).

[10] G. C. Fox and S. Wolfram, *Observables for the Analysis of Event Shapes in e+ e- Annihilation and Other Processes*, Phys. Rev. Lett. **41**, 1581 (1978).




doi:doi:10.6342/NTU202203205

[11] *PDG Value of* $D^- \to K_S\pi^-$, `https:// pdglive.lbl.gov/BranchingRatio.action?desig=2parCode=S031home=MXXX035`.

[12] *PDG Value of* $B^0 \to D^-\pi^+$, `https:// pdglive.lbl.gov/BranchingRatio.action?desig=1parCode=S018home=BXXX020`.

[13] *Number of B in HadronB(J)*, `https://belle.kek.jp/secured/nbb/nbb.html`.

[14] B. Bhuyan, *High $P_T$ Tracking Efficiency Using Partially Reconstructed $D^*$ Decays*, Belle Note 1165 (2010).

[15] S.Nishida, *Study of Kaon and Pion Identification Using Inclusive $D^*$ Sample*, Belle Note 779 (2005).

[16] M.-Z. W. Kai-Jen Tien, *Proton identification efficiency study*, Belle Note 1279 (2012).

[17] *PDG Value of* $\Lambda \to p\pi^-$, `https:// pdglive.lbl.gov/BranchingRatio.action?desig=1parCode=S018home=BXXX020`.



doi:doi:10.6342/NTU202203205